ELECTRONIC SPECTROSCOPY OF SOME ENVIRONMENTALLY IMPORTANT MOLECULES USING SYNCHROTRON RADIATION

By

ANUVAB MANDAL

Enrolment No.: PHYS01200804025
Bhabha Atomic Research Centre,
Trombay, Mumbai 400085, India

A thesis submitted to the
Board of Studies in Physical Sciences
In partial fulfillment of requirements
for the Degree of
DOCTOR OF PHILOSOPHY
of
HOMI BHABHA NATIONAL INSTITUTE

August, 2014

Homi Bhabha National Institute

Recommendations of the Viva Voce Committee

As members of the Viva Voce committee, we certify that we have read the dissertation prepared by Mr. Anuvab Mandal entitled “Electronic Spectroscopy of some Environmentally Important Molecules using Synchrotron Radiation” and recommend that it may be accepted as fulfilling the thesis requirement for award of Degree of Doctor of Philosophy.

29/12/2014
Chairman – Prof. K. G. Manohar **Date:**

29/12/2014
Guide / Convener – Prof. B. N. Jagatap **Date:**

29/12/2014.
Member – Prof. S. G. Nakhate **Date:**

Arup Banerjee 29/12/2014
Member – Prof. Arup Banerjee **Date:**

Krishna Rai Dastidar 29.12.14.
External – Prof. K. Rai Dastidar **Date:**

Final approval and acceptance of this thesis is contingent upon the candidate’s submission of the final copies of the thesis to HBNI.

I hereby certify that I have read this thesis prepared under my direction and recommend that it may be accepted as fulfilling the thesis requirement.

Date: December 29, 2014

Place: Mumbai

Prof. B. N. Jagatap

STATEMENT BY AUTHOR

This dissertation is submitted in partial fulfillment of requirements for an advanced degree at Homi Bhabha National Institute (HBNI) and is deposited in the Library to be made available to borrowers under rules of the HBNI.

Brief quotations from this dissertation are allowable without special permission, provided that accurate acknowledgement of source is made. Requests for permission for extended quotation from or reproduction of this manuscript in whole or in part may be granted by the Competent Authority of HBNI when in his or her judgment the proposed use of the material is in the interests of scholarship. In all other instances, however, permission must be obtained from the author.

Anuvab Mandal

DECLARATION

I, hereby declare that the investigation presented in the thesis has been carried out by me. The work is original and has not been submitted earlier as a whole or in part for a degree / diploma at this or any other Institution / University.

Anuvab Mandal

LIST OF PUBLICATIONS ARISING FROM THE THESIS

JOURNAL

1. "Electronic state spectroscopy of diiodomethane (CH_2I_2): Experimental and computational studies in the 30000–95000 cm^{-1} region," **Anuvab Mandal**, Param Jeet Singh, Aparna Shastri, and B. N. Jagatap, The Journal of Chemical Physics **140**, 194312 (2014).

2. "Rydberg and valence excited states of dibromomethane in 35,000–95,000 cm^{-1} region studied using synchrotron radiation," **Anuvab Mandal**, Param Jeet Singh, Aparna Shastri, Vijay Kumar, B. N. Raja Sekhar, B. N. Jagatap, Journal of Quantitative Spectroscopy & Radiative Transfer **144**, 164 (2014).

3. "Vibronic and Rydberg series assignments in the vacuum ultraviolet absorption spectrum of nitrous oxide", Aparna Shastri, Param Jeet Singh, Sunanda Krishnakumar, **Anuvab Mandal**, B. N. Raja Sekhar, R. D'Souza and B. N. Jagatap, Journal of Quantitative Spectroscopy & Radiative Transfer **147**, 121 (2014).

4. "Vacuum Ultraviolet photoabsorption spectroscopy of CH_2Cl_2 and CD_2Cl_2 in the energy region 50,000–95,000 cm^{-1}", **Anuvab Mandal**, Param Jeet Singh, Aparna Shastri and B.N. Jagatap, Journal of Quantitative Spectroscopy & Radiative Transfer **149**, 291 (2014).

5. "Photoabsorption and photodissociation studies of dimethyl sulphoxide in the 35,000-80,000 cm^{-1} region using synchrotron radiation", **Anuvab Mandal**, Param Jeet Singh, Aparna Shastri and B. N. Jagatap, Journal of Quantitative Spectroscopy & Radiative Transfer (communicated).

CONFERENCE

1. "VUV photoabsorption studies of DMSO using synchrotron radiation," **Anuvab Mandal**, Param Jeet Singh, Aparna Shastri, S. V. N. Bhaskara Rao, B. N. Jagatap, *DAE-BRNS Symposium on Atomic, Molecular and Optical Physics,* IISER Kolkata, December 14-17, 2012.
2. "Electronic structure of dibromomethane: VUV spectroscopy with synchrotron radiation source and TDDFT calculations," **Anuvab Mandal**, Param Jeet Singh, Vijay Kumar, Aparna Shastri, B. N. Jagatap, *Current Trends in Theoretical Chemistry,* BARC, Mumbai September 24-27, 2013.
3. "Study of Rydberg States of Diiodomethane Using VUV Synchrotron Radiation," **Anuvab Mandal**, Param Jeet Singh, Vijay Kumar, Aparna Shastri, B. N. Jagatap, *Trombay Symposium on Radiation Photochemistry,* BARC, Mumbai, January 06-09, 2014.

PUBLICATION NOT INCLUDED IN THE THESIS

1. "Development of an experimental set-up for low temperature spectroscopic studies of matrix isolated molecules and molecular ices", Param Jeet Singh, B. N. Raja Sekhar, K. Sundararajan, A. Shastri, Vijay Kumar, **Anuvab Mandal**, A. K. Sagar, M. S. Ansari, P. K. Kush, B. N. Jagatap, Nuclear Instruments and Methods in Physics Research A (communicated).

Anuvab Mandal

Dedicated to my parents

ACKNOWLEDGEMENTS

I would like to express my deepest gratitude to my advisor, Prof. B. N. Jagatap for his patient guidance, mentorship, encouragement and unwavering support throughout the course of the work. Fortunate to be one of his students, I have learned a great amount of Physics from his teaching. His scientific intuition has inspired me and enriched my growth as a researcher.

This thesis would not have materialized without the efforts of Dr. Aparna Shastri and Paramjeet Singh who have introduced me to the field of VUV spectroscopy and taught me experimental and theoretical techniques patiently and thoroughly. I am greatly indebted to them for their huge support throughout the course of the work. Their friendly and caring nature has always made me comfortable while working in the lab.

I am would like to thank Drs. R. D’Souza, S. V. N. Bhaskara Rao, Sunanda K. and B. N. Raja Sekhar for their help and encouragement. I have learned a lot from their invaluable suggestions. I extend many thanks to my doctoral committee members, Dr. K. G. Manohar, Dr. A. Banerjee and Dr. S. G. Nakhate for their encouragement, keen assessment and vital suggestions.

I am thankful to Babita, Vijay Kumar and Asim Kumar Das for their help during experiments. I would like to thank the Indus synchrotron radiation source facility for beamtime. Thanks are due to Sampath Kumar, Sanjay Somkuwar, Ajay Kumar and Yogesh Arondekar for providing generous support in the maintenance of electronic components on the beamline. I am also thankful to Dr. D. Bhattacharya for his help in the procurement of the chemical samples.

I express my thanks to all my friends especially Debes, Nazir, Pankaj, Naveen, Rohit, Niharika, Yogeshwar, Arvind, Neeranjan, Lokesh, Sumit, Ravi and Ganesh for their affectionate support and good wishes. My heartfelt appreciation goes to Subarna for encouraging me and lending me a sympathetic ear whenever needed.

Last but not least, I would not have come this far without the support of my family. I am extremely grateful to my parents for their encouragement, endless love and blessings.

CONTENTS

Homi Bhabha National Institute

SYNOPSIS OF Ph. D. THESIS

Name of the Student:	Anuvab Mandal
Name of the Constituent Institution:	Homi Bhabha National Institute Bhabha Atomic Research Centre Trombay, Mumbai 400085, India
Enrolment No.:	PHYS01200804025
Title of the Thesis:	Electronic Spectroscopy of some Environmentally Important Molecules using Synchrotron Radiation
Board of Studies:	Physical Sciences

SYNOPSIS

Excited electronic states of polyatomic molecules are important in many areas of physics and chemistry. It is well recognized that photochemical processes in the upper atmosphere proceed through formation of highly excited and super-excited states [1]. The chemistry of electronically excited species is also of fundamental importance in studies of flames and combustion, plasmas, semiconductor etching, pollution control, etc. [2]. In the biological domain, there exists evidence that photo-biological phenomena like photosynthesis may proceed via formation of intermediate states of Rydberg or charge transfer character [3]. Investigation of the excited state electronic structure of polyatomic molecules is thus an important field of study, both from the fundamental and applied point of view.

The energy of the lowest electronic transition in a molecule is given by the gap between the highest occupied molecular orbital (HOMO) and the lowest unoccupied molecular orbital (LUMO), which is generally in the UV-visible region. On the other hand, the highly excited states of molecules lie in the vacuum ultraviolet (VUV) region (~6–25 eV). Since the first ionization potential of most molecules lies in the range ~9–12 eV, spectroscopic studies in the VUV region yield rich information about the physical processes, e.g., photo-dissociation, photo-ionization, photo-fragmentation etc. that occur at energies close to the ionization potential. The electronic absorption spectra of polyatomic molecules up to their first ionization limit comprise of several valence, Rydberg and intermediate/mixed type transitions. Interpretation of the observed spectra in terms of these transitions is an important issue in the understanding of the structure of the excited states. Another vital issue is the assignment of the vibrational structure accompanying the electronic transitions, *i.e.*, vibronic transitions, which are related to several factors such as the geometry changes in the excited states, symmetry based selection rules and interactions between states.

VUV spectroscopic investigations in early days were often constrained by the limitations of traditional light sources which were either very weak or not continuously tunable. In the past few decades, synchrotron radiation has revolutionized VUV and soft X-ray spectroscopy and today it is well established as a powerful and versatile light source. Its unique properties like high brilliance, continuous tunability, well-defined pulsed time structure and polarization, etc. have made it one of the best light sources available. Since it is produced in ultra-high vacuum environment, it is spectroscopically pure unlike the traditional laboratory sources. In particular, in the VUV region it is the only source that offers both high intensity and tunability over a large spectral region.

This thesis presents VUV photoabsorption spectroscopy of a few halogen, sulphur and nitrogen containing polyatomic molecules in gas phase using synchrotron radiation. The molecules chosen for these studies are dichloromethane (CH_2Cl_2), dibromomethane (CH_2Br_2), diiodomethane (CH_2I_2), dimethyl sulphoxide (CH_3SOCH_3) and nitrous oxide (N_2O). These molecules play major roles in atmospheric chemistry and the knowledge of their excited state electronic structures is important in the understanding of complex photochemical processes involving them and this has been the basic motivation for the present work. A major difference between N_2O and the other molecules studied is that while the dihalomethanes and DMSO belong to the C_{2v} and C_s point groups, N_2O being linear in the ground state belongs to the $C_{\infty v}$ point group. This study has been included in order to gain a better perspective on the excited state spectroscopy of different types of polyatomic molecules, non-linear as well as linear.

The experiments are performed at Indus-1 synchrotron radiation source [4] at the Raja Ramanna Centre for Advanced Technology, Indore, India. The Indus-1 is a 450 MeV storage ring with a critical wavelength (λ_c) of 61 Å and a photon flux of 7×10^{11} photons/sec/mrad/0.1% bandwidth at λ_c. Photoabsorption spectra are recorded using two VUV beamlines at Indus-1, *i.e.*, the Photophysics [5] and High Resolution Vacuum Ultra-Violet (HRVUV) beamlines [6]. Absorption spectra of molecules in the wavelength region 1050–3000 Å typically consist of both valence and Rydberg transitions converging to the first ionization potential (IP). If the HOMOs are quite close in energy, one may observe Rydberg series converging to several IPs, each corresponding to removal of an electron from one of these HOMOs. Electronic transitions are also sometimes accompanied by vibrational structure. Assignment of these vibronic bands is not always straightforward since the equilibrium geometry and vibrational frequencies in the excited states may be drastically different from those in the ground state. In this context, vibrational frequencies of the corresponding cationic molecule if known from experiment or theory are useful in guiding the assignments, especially for Rydberg states. Isotopic substitution is also a well-known tool for confirming vibronic assignments. In the present work, in order to corroborate the spectral analyses, VUV photoabsorption spectra of the deuterated analogues of the halogen and sulphur containing molecules (CD_2Cl_2, CD_2Br_2, CD_2I_2 and CD_3SOCD_3) are also studied. This has greatly helped in verifying assignments or clarifying situations where discrepancies existed. Further, interpretation and assignments are supported by quantum chemical calculations.

Computational studies of molecules are very useful in interpretation and understanding of experimental results in molecular spectroscopy. In the present work, geometry optimization of the molecule is carried out using the density functional theory (DFT) and Møller-Plesset second order perturbation theory (MP2) methodologies and several basis sets. Computation of ground state vibrational frequencies and their comparison with experimental values help in verifying the accuracy of the calculation and identifying the most suitable method/basis set to be used for further work. Vertical excited states are calculated using the time dependent density functional theory (TDDFT) and fixing the molecular geometry at the ground state optimized values. Correlation of theoretically predicted values with experimental energies is done according to the symmetries of the initial and final molecular orbitals (MOs) involved in the transition. Since vibrational frequencies of the cationic ground states of molecules are generally good estimates of the corresponding frequencies in excited Rydberg states, optimized geometries and vibrational frequencies of the cationic ground states of all the molecules studied are computed. All computations are performed using the GAMESS (US) code [7]. Visualization of the MOs, which is very helpful in understanding the spectra, is carried out using the software MacMolPlt [8].

The thesis is organized into seven chapters. Chapter 1, which forms the introduction to the thesis, provides an overview of the VUV spectroscopy using synchrotron radiation. A few key concepts in molecular electronic spectroscopy used frequently in the thesis, such as valence and Rydberg states, quantum defect analysis, vibronic bands, isotopic shift, molecular symmetry, group theoretical formalism, etc. are discussed briefly here. The details of the synchrotron source, beamlines, experimental setup and procedures are discussed in this chapter. The computational methods and programs employed in this work along with a brief outline of their working principles are also provided. This chapter thus forms the basis of the work reported in the subsequent chapters.

In Chapter 2, a comprehensive investigation of the VUV absorption spectrum of CH_2I_2 in the region from 30,000 to 95,000 cm^{-1} (3.7–11.8 eV) is presented. CH_2I_2 has recently been recognized as a molecule of significant atmospheric interest [9,10]. The photolysis of CH_2I_2 in the presence of ozone results in formation of iodine oxide (IO) which in turn contributes to formation of aerosols, especially in coastal areas [10]. In addition to its atmospheric importance, CH_2I_2 being a small molecule it is also considered as a prototype for examining photo-dissociation dynamics of two-chromophore systems [11]. Despite the vast amount of literature available in the UV region, there is very little information available on the VUV spectrum of CH_2I_2. The only published work on the VUV photoabsorption spectrum of CH_2I_2 is by Okabe *et al*. [12] who reported absorption cross sections in the region 66,666–90,910 cm^{-1} measured using a hydrogen discharge lamp. In our work, it is observed that the absorption bands in the region 30,000–50,000 cm^{-1} are due to valence transitions, while the VUV spectrum in the range from 50,000 to 95,000 cm^{-1} is dominated by several Rydberg series converging to the first four IPs of CH_2I_2 at 9.46, 9.76, 10.21 and 10.56 eV corresponding to removal of an electron from the outermost $3b_2$, $2b_1$, $1a_2$ and $4a_1$ non-bonding orbitals respectively. Rydberg series of *ns*, *np* and *nd* type converging to each of the four ionization potentials are assigned based on the quantum defect analysis. Vertical excited states, calculated using the TDDFT method, are used to identify the transitions observed in the experimental spectra. DFT calculations of the neutral and ionic ground state geometries and vibrational frequencies are used to assign the observed vibronic structure. Vibronic features accompanying the Rydberg series are observed to be mainly due to excitation of the CI symmetric stretch (ν_3) and CH_2 wag (ν_8) modes, with smaller contributions from the CH symmetric stretch (ν_1). UV absorption bands are assigned to the low lying valence states 1^1B_2, 1^1B_1, 2^1A_1, 3^1A_1, 2^1B_1 and 2^1B_2 and the unusually high underlying intensity in parts of the VUV spectrum is attributed to valence states with high oscillator strength. The VUV absorption spectrum of CH_2I_2 in the 50,000–66,666 cm^{-1} region and spectral analysis in the 50,000–85,000 cm^{-1} region are reported here for the first time. This is also the first report of the VUV photoabsorption spectrum of CD_2I_2, which serves to verify and consolidate the spectral assignments.

In Chapter 3, UV-VUV photoabsorption spectroscopy of CH_2Br_2 and CD_2Br_2 in the energy region 35,000–95,000 cm^{-1} (4.3–11.8 eV) is presented. In nature, CH_2Br_2 is produced in seawater by macroalgae and released into the atmosphere by volatilization [13]. In the troposphere, it degrades by reacting with the hydroxyl (OH) radical which is produced by photolysis of ozone, thereby playing an important role in the ozone balance in the atmosphere [9]. A recent study on global modeling of CH_2Br_2 has indicated its important role in contributing reactive bromine to the stratosphere [14]. The VUV absorption spectrum of CH_2Br_2 was reported for the first time using hydrogen discharge lamp by Causley *et al.* [15], after which there have been no further VUV absorption studies till date. These authors assigned many of the observed lines to *ns* (up to $n = 9$) Rydberg series converging to three *IP*s *viz.* b_1, b_2 and $(a_1 + a_2)$ and the first members of *np* and *nd* Rydberg transitions were assigned based on term value calculations. In their work, several observed peaks were left unassigned and a few features were given tentative assignments. In the present work, transitions in the region 35,000–50,000 cm^{-1} are identified to be of valence nature. Using quantum defect analysis, most of the transitions in the region 50,000–95,000 cm^{-1} are assigned to Rydberg series of *ns*, *np* and *nd* type converging to the first four ionization limits at 10.52, 10.74, 11.21 and 11.30 eV corresponding to excitations from the outermost orbitals $3b_2$, $2b_1$, $1a_2$, $4a_1$ of CH_2Br_2. The 5*p* and 4*d* Rydberg states are observed to be associated with vibrational structures. These vibronic features, identified using vibrational frequencies of the cationic species calculated by DFT as a guideline, are assigned exclusively to the totally symmetric (a_1) CBr symmetric stretching mode (ν_3) in contrast to the earlier assignment [15] to ν_3 and CH_2 bending (ν_2) modes. The vertical excited state energies of CH_2Br_2 calculated using TDDFT method are compared with the experimentally observed transitions. The calculations are further used to infer the valence transitions responsible for the broad intensity pedestals underlying the Rydberg transitions. The assignments are confirmed using isotopic substitution studies on CD_2Br_2 whose UV-VUV photoabsorption spectrum is reported here for the first time. This work presents a consolidated analysis of the UV-VUV photoabsorption spectrum of dibromomethane.

Chapter 4 describes the photoabsorption spectroscopy of CH_2Cl_2 and CD_2Cl_2 in the energy region from 50,000 to 95,000 cm^{-1} (6.2–11.8 eV). CH_2Cl_2 is a molecule of atmospheric interest, sources of which are mainly anthropogenic arising from industrial and commercial uses [16]. Natural emissions from oceans [17] and biomass burning [18] also contribute to the amount of CH_2Cl_2 in the atmosphere. Although reaction with hydroxyl radicals (OH) limits the tropospheric lifetime of this molecule to 5–6 months, about 2% of CH_2Cl_2 emissions reach the stratosphere [19] where it plays an important role in ozone layer destruction. One of the earliest reported studies of VUV photoabsorption spectrum of CH_2Cl_2 was by Zobel *et al.* [20] who tentatively assigned some Rydberg transitions and a few vibronic features in the spectrum to the ν_3 (CCl_2 s-stretch), ν_2 (CH_2 bend) and ν_4 (CCl_2 scissor) modes. Tsubomura *et al.* [21] reported the spectrum of CH_2Cl_2 in the region 52,630–62,500 cm^{-1} using a hydrogen discharge lamp and assigned the band in the region 50,000–60,000 cm^{-1} to an $n \rightarrow \sigma^*$ transition. Subsequently, Russell *et al.* [22] and Robin [23] assigned a few bands to Rydberg transitions, based on the available ionization potential measurements for CH_2Cl_2. Lee *et al.* [24] reported photobsorption and fluorescence cross-sections of CH_2Cl_2 in the region 47600–95240 cm^{-1} measured at a resolution of 2 Å using synchrotron radiation. They identified six progressions attributed to ν_3 (CCl_2 s-stretch) and ν_5 (CH_2 twist) modes. However they did not assign the Rydberg series origins. The Rydberg series and vibronic analysis of this molecule reported in literature is incomplete and shows several discrepancies. In the work reported here, the observed absorption band of CH_2Cl_2 in the region 50,000–60,000 cm^{-1} is identified to be of valence nature and most of the bands in the region 60,000–95,000 cm^{-1} are fitted to Rydberg series of *ns, np* and *nd* type converging to the first four ionization potentials 11.32, 11.36, 12.16 and 12.27 eV of CH_2Cl_2 arising from excitation of an electron from one of the four outermost Cl non-bonding orbitals. A few Rydberg transitions are accompanied by vibronic features. Optimized geometries and vibrational frequencies of the ground states of CH_2Cl_2/CD_2Cl_2 and $CH_2Cl_2^+$/$CD_2Cl_2^+$ obtained by DFT help in assigning vibrational features observed in the spectra. The vertical excited states of CH_2Cl_2 are calculated using TDDFT and are correlated with experimentally observed electronic states based on the symmetries of the initial and final MOs involved in a transition. Observed vibronic features associated with a few Rydberg states are assigned mainly to the CCl_2 symmetric stretch (ν_3) mode with smaller contributions from the CH_2 symmetric stretch (ν_1), CH_2 bend (ν_2) and CH_2 wag (ν_8) modes. As before, assignments are corroborated by comparison with the absorption spectrum of the deuterated isotopologue CD_2Cl_2. This chapter presents a consolidated analysis of VUV spectra of CH_2Cl_2 and CD_2Cl_2.

Chapter 5 deals with the VUV spectroscopy of dimethyl sulphoxide (DMSO) and its deuterated analogue; DMSO-h_6 and DMSO-d_6. DMSO is a versatile solvent widely used in industrial applications and is a natural product of biodegradation of organo-sulphur compounds in the biosphere [25]. It is the simplest example of the class of sulphoxide compounds and plays an important role in sulphur balance in the atmosphere. The electronically excited states of DMSO are important in understanding photochemical reactions involving this compound. Several theoretical studies on electronic structure of DMSO are available in the literature [26-28]. The photoabsorption spectrum of DMSO in the region 1150–3400 Å using synchrotron radiation has been reported recently by Drage *et al.* [25]. However, vibronic analysis of the observed transitions reported in literature is incomplete. In the present work, photoabsorption spectra of DMSO-h_6 and DMSO-d_6 are studied in the region 1050–3500 Å at a resolution of ~1.5 Å using the Photophysics beamline. Details of the experiments performed and the analysis of the spectra carried out with the help of quantum chemical calculations are presented in this chapter. The overall spectral features observed for DMSO-h_6 are in good agreement with earlier work, while the VUV photoabsorption spectrum of DMSO-d_6 has been reported here for the first time. It is observed that the vibronic structures which appear in the absorption spectrum of DMSO-h_6 are not very prominent in DMSO-d_6, in fact some of them seem to disappear. In order to investigate this aspect further, photoabsorption spectra of DMSO-h_6 and DMSO-d_6 are recorded at a better resolution (~0.5 Å) in the region 1300–2300 Å using the HRVUV beamline. In this spectrum, however, several new features are observed which may have the origin in the dissociation of the molecule by the broadband radiation permitted by the configuration of HRVUV beamline.

In Chapter 6, Rydberg series and vibronic assignments of N_2O in the 72,000 cm^{-1} – 95,000 cm^{-1} region are discussed. There has been continued interest in the spectroscopy of N_2O due to its important role in atmospheric and astrophysical processes [29]. Photodissociation of N_2O is known to produce metastable species such as O (^1S, ^1D) which participate in important atmospheric photochemical reactions and recent studies show that nitrous oxide is the single largest anthropogenic threat to the ozone layer with a very high global warming potential [29]. Early work on nitrous oxide is well summarized in the review by Rabalais *et al*. [30]. The only synchrotron radiation based photoabsorption study of this molecule is by Nee *et al* [31] who reported absolute cross sections up to the first IP without any new spectral assignments. In the region > 72,000 cm^{-1} dominated by Rydberg transitions, assignments of Rydberg series and accompanying vibronic structures reported in earlier works are at wide variance with each other. Some of these discrepancies were sorted out by Cossart-Magos *et al* [32] who used frozen core calculations to assign Rydberg transitions. There have been a wide range of theoretical studies of N_2O, amongst which the report by Hopper [33] is one of the most comprehensive report on excited states of this molecule. Despite a large volume of experimental and theoretical work, there remain several unresolved issues in the excited state electronic structure of nitrous oxide. In the present work, a reinvestigation of the absorption spectrum of nitrous oxide (N_2O) in the 72,000 cm^{-1} – 95,000 cm^{-1} region is carried out using synchrotron radiation. The observed spectrum comprises mainly of Rydberg series converging to the two spin-orbit components ($^2\Pi_{1/2,3/2}$) of the ground state of N_2O^+ and a few high lying valence transitions. The $3p\pi\,^1\Sigma^+$ state at ~ 77,600 cm^{-1} shows large quantum defect (0.96) which is explained as arising due to mixed valence-Rydberg character. In the 85,000 - 95,000 cm^{-1} region, a number of absorption features are observed with greater clarity than in earlier photoabsorption studies and assigned to Rydberg series of type $nl\lambda$ (n=3,4; l=s,p,d; λ=σ,π,δ) and accompanying vibronic bands. Spectral analysis is aided by extensive quantum chemical calculations of vertical excited states using time dependent density functional theory. This work has resulted in clarification of several discrepancies in earlier Rydberg series assignments. Additionally, the $3p\pi\ ^3\Sigma^-$ Rydberg state at 85,788 cm^{-1}, the valence transition 7σ→3π ($^1\Pi$) at 87,433 cm^{-1} and the 3dλ Rydberg series in the 91,700 – 92,600 cm^{-1} region are assigned for the first time.

Finally, the important conclusions from the present studies and scope for future work are summarized in Chapter 7.

References

1. Y. Hatano, Rad. Phys. Chem. **67**, 187 (2003).
2. N. J. Mason, A. Dawes, R. Mukerji, E. A. Drage, E. Vasekova, S. M. Webb and P. Limão-Vieira, J. Phys. B: At. Mol. Opt. Phys. **38**, S839 (2005).
3. G. L. Findley, J. A. Wilder, P. Hochmann and S.P. McGlynn, Photophysics of Highly-Excited States, in: S. P. McGlynn, G. L. Findley, R. H. Huebner (eds.), Photophysics and Photochemistry in the Vacuum Ultraviolet, Springer, Netherlands (1985), pp. 1-40.
4. Indus-1, web page http://www.cat.ernet.in/technology/accel/indus/
5. P. M. Raja Rao, N. C. Das, B. N. Raja Sekhar, S. Padmanabhan, A. Shastri, S. S. Bhattacharya and A. P. Roy, Nuc. Instr. Meth. Phys. Res. A **467–468**, 613 (2001).
6. P. J. Singh, A. Shastri, R. S. Kumar, S. N. Jha, S. V. N. B. Rao, R. D'Souza and B. N. Jagatap, Nuc. Instr. Meth. Phys. Res. A **634**, 113 (2011).
7. M. W. Schmidt, K. K. Baldridge, J. A. Boatz, S. T. Elbert, M. S. Gordon, J. H. Jensen, S. Koseki, N. Matsunaga, K. A. Nguyen, S. Su, T. L. Windus, M. Dupuis and J. A. Montgomery, J. Comp. Chem. **14**, 1347 (1993).
8. B. M. Bode and M. S. Gordon, J. Mol. Graph. Mod. **16**, 133 (1998).
9. J. C. Mössinger, D. E. Shallcross and R. Anthony Cox, J. Chem. Soc. Faraday Trans. **94**, 1391(1998).
10. T. J. Johnson, T. Masiello and S. W. Sharpe, Atmos. Chem. Phys. **6**, 2581 (2006).
11. W. M. Kwok and D. L. Phillips, J. Chem. Phys. **104**, 2529 (1996).
12. H. Okabe, M. Kawasaki and Y. Tanaka, J. Chem. Phys. **73**, 6162 (1980).
13. K. D. Goodwin, M. E. Lidstrom and R. S. Oremland, Env. Sci. Tech. **31**, 3188 (1997).
14. Q. Liang, R. S. Stolarski, S. R. Kawa, J. E. Nielsen, A. R. Douglass, J. M. Rodriguez, D. R. Blake, E. L. Atlas and L. E. Ott, Atmos. Chem. Phys. **10**, 2269 (2010).
15. G. C. Causley and B. R. Russell, J. Chem. Phys. **62**, 848 (1975).
16. R. Coppmann (ed.), Volatile Organic Compounds in the Atmosphere, Wiley-Blackwell, (2007) pp. 173-220.
17. P. Fabian (ed.) and O. N. Singh (ed.), Reactive Halogen Compounds in the Atmosphere, Springer, Berlin (1999) pp. 45-79.
18. J. M. Lobert, W. C. Keene, J. A. Logan and R. Yevich, J. Geophys. Res. Atmos. **104**, 8373 (1999).
19. T. E. Graedel and W. Keene, Pure Appl. Chem. **68**, 1689 (1996).
20. C. R. Zobel and A. B. F. Duncan, J. Am. Chem. Soc. **77**, 2611 (1955).
21. H. Tsubomura, K. Kimura, K. Kaya, J. Tanaka and S. Nagakura, Bull. Chem. Soc. Jap. **37**, 417 (1964).
22. B. R. Russell, L. O. Edwards and J. W. Raymonda, J. Am. Chem. Soc. 95, 2129 (1973).

23. M. B. Robin, Higher Excited States of Polyatomic Molecules. Vol. 1, Academic, New York (1974).
24. L. C. Lee and M. Suto, Chem. Phys. **114**, 423 (1987).
25. E. A. Drage, P. Cahillane, S. V. Hoffmann, N. J. Mason and P. Limão-Vieira, Chem. Phys. **331**, 447 (2007).
26. J. W. Cubbage and W. S. Jenks, J. Phys. Chem. A **105**, 10588 (2001).
27. V. P. Mondéjar, M. J. Yusá, I. G. Cuesta, A. M. J. S. de Merás and J. Sánchez-Marín, Theo. Chem. Accounts **118**, 527 (2007).
28. E. Bodo and G. Lanaro, Chem. Phys. **377**, 136 (2010).
29. A. S. Ravishankara, J. S. Daniel and R. W. Portmann, Science **326**, 123 (2009).
30. J. W. Rabalais, J. M. McDonald, V. Scherr and S. P. McGlynn, Chem. Rev. **71**, 73 (1971).
31. J. B. Nee, J. C. Yang, P. C. Lee, X. Y. Wang and C. T. Kuo, Chin. J. Phys. **37**, 172 (1999).
32. C. Cossart-Magos, M. Jungen and F. Launay, J. Chem. Phys. **114**, 7368 (2001).
33. D. G. Hopper, J. Chem. Phys. **80**, 4290 (1984).

Publications in Refereed Journals:

Published:

1. “Electronic state spectroscopy of diiodomethane (CH_2I_2): Experimental and computational studies in the 30000–95000 cm^{-1} region,” **Anuvab Mandal**, Param Jeet Singh, Aparna Shastri, and B. N. Jagatap, The Journal of Chemical Physics **140**, 194312 (2014).
2. “Rydberg and valence excited states of dibromomethane in 35,000–95,000 cm^{-1} region studied using synchrotron radiation,” **Anuvab Mandal**, Param Jeet Singh, Aparna Shastri, Vijay Kumar, B. N. Raja Sekhar, B. N. Jagatap, Journal of Quantitative Spectroscopy & Radiative Transfer **144**, 164 (2014).

Accepted:

3. “Vibronic and Rydberg series assignments in the vacuum ultraviolet absorption spectrum of nitrous oxide”, Aparna Shastri, Param Jeet Singh, Sunanda Krishnakumar, **Anuvab Mandal**, B. N. Raja Sekhar, R. D’Souza and B. N. Jagatap, Journal of Quantitative Spectroscopy & Radiative Transfer (to appear).

Communicated:

4. “Photoabsorption spectroscopy of CH_2Cl_2 and CD_2Cl_2 in the energy region 50,000 to 95,000 cm^{-1}”, **Anuvab Mandal**, Param Jeet Singh, Aparna Shastri and B.N. Jagatap, Journal of Quantitative Spectroscopy & Radiative Transfer.

Other Publications:

1. “VUV photoabsorption studies of DMSO using synchrotron radiation,” **Anuvab Mandal**, Param Jeet Singh, Aparna Shastri, S. V. N. Bhaskara Rao, B. N. Jagatap, *DAE-BRNS Symposium on Atomic, Molecular and Optical Physics, Kolkata* (2012).
2. “Electronic structure of dibromomethane: VUV spectroscopy with synchrotron radiation source and TDDFT calculations,” **Anuvab Mandal**, Param Jeet Singh, Vijay Kumar, Aparna Shastri, B. N. Jagatap, *Current Trends in Theoretical Chemistry, Mumbai* (2013).
3. “Study of Rydberg States of Diiodomethane Using VUV Synchrotron Radiation,” **Anuvab Mandal**, Param Jeet Singh, Vijay Kumar, Aparna Shastri, B. N. Jagatap, *Trombay Symposium on Radiation Photochemistry, Mumbai* (2014).

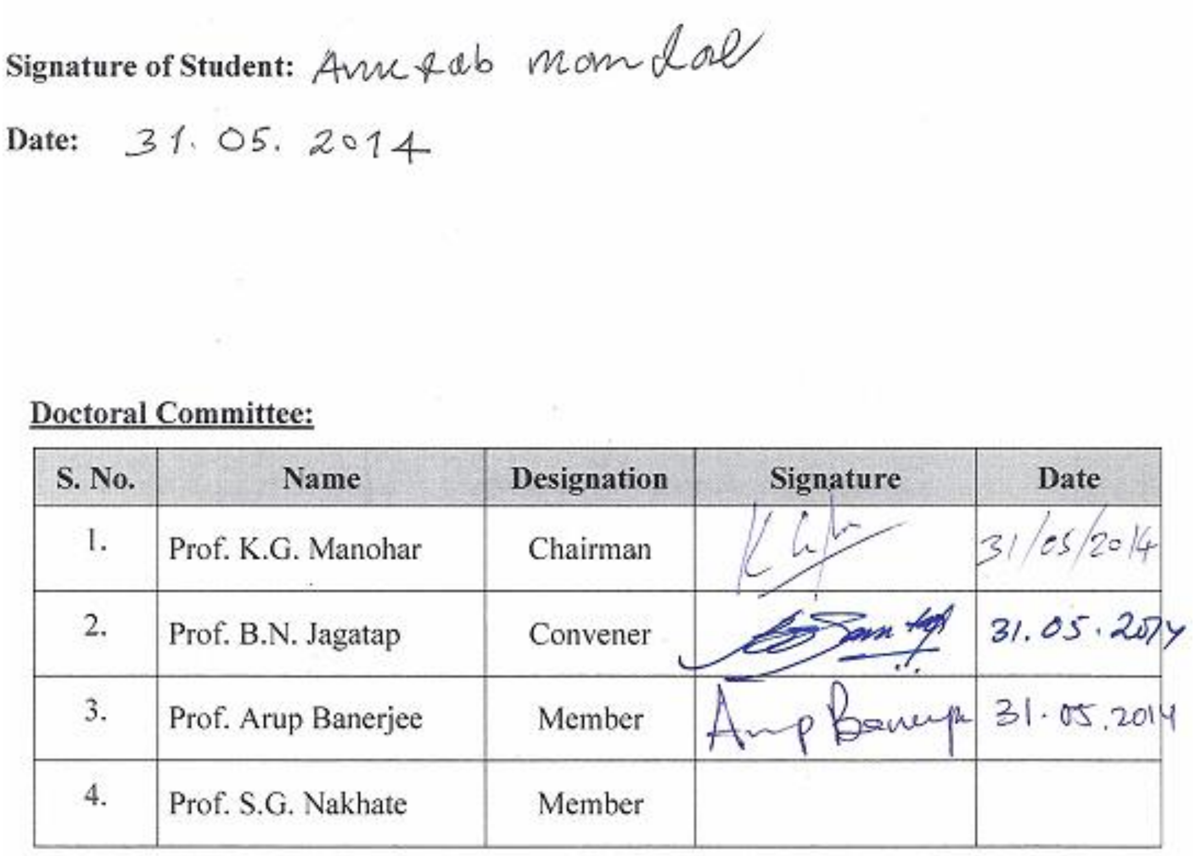

Signature of Student: Anuvab Mandal

Date: 31. 05. 2014

Doctoral Committee:

S. No.	Name	Designation	Signature	Date
1.	Prof. K.G. Manohar	Chairman		31/05/2014
2.	Prof. B.N. Jagatap	Convener		31.05.2014
3.	Prof. Arup Banerjee	Member	Arup Banerjee	31.05.2014
4.	Prof. S.G. Nakhate	Member		

LIST OF FIGURES

LIST OF TABLES

CHAPTER 1

INTRODUCTION

Electronic spectroscopy of molecules is of fundamental importance in furthering the understanding of the electronic structure of matter since successful development of theoretical models relies heavily on the availability of accurate experimental data. Electronically excited states of molecules are central to the understanding of radiative and nonradiative processes in many diverse areas like atmospheric physics and chemistry, astrophysics and astrochemistry, plasmas, flames and combustion, pollution control, etc. [1]. It is known that the highly excited states, the Rydberg as well as the superexcited, play a key role in photochemical processes in the upper atmosphere [2] as well as photobiological processes like photosynthesis [3]. Investigation of the excited state structure of polyatomic molecules thus encompasses a wide spectrum of issues, both fundamental and applied.

The energy of the lowest electronic transition in a molecule generally lies in the UV-visible region while the highly excited states typically lie in the vacuum ultraviolet (VUV) region (~6–25 eV). Since the first ionization potential of most molecules lies in the range ~9–12 eV, spectroscopic studies in the VUV region yield rich information about the physical processes, *e.g.*, photo-dissociation, photo-ionization, photo-fragmentation, etc. that occur at energies close to the ionization potential. The energy region of 5-12 eV is of particular importance in molecular physics since it covers the excited electronic states including the valence, Rydberg and intermediate/mixed type levels of molecules up to and little above the first ionization potential of most of the molecules. A continuously tunable photon source that covers this energy range is essential for such investigations. Synchrotron radiation with its characteristic properties like high intensity and tunability over the entire VUV region is an ideal light source for these studies.

This thesis focuses on the VUV photoabsorption spectroscopy of a few halogen, sulphur and nitrogen containing polyatomic molecules in gas phase using synchrotron radiation. The molecules chosen for these investigations are dichloromethane (CH_2Cl_2), dibromomethane (CH_2Br_2), diiodomethane (CH_2I_2), dimethyl sulphoxide (DMSO, CH_3SOCH_3) and nitrous oxide (N_2O). These studies are motivated by the fact that these molecules are known to play major roles in atmospheric chemistry and consequently the knowledge of their excited state electronic structures is important in the understanding of complex photochemical processes involving them. From the molecular symmetry point of view, the dihalomethanes and DMSO belong to the C_{2v} and C_s point groups while N_2O being linear in the ground state belongs to the $C_{\infty v}$ point group. The study presented in the thesis thus provides a perspective of the excited state spectroscopy of different types of polyatomic molecules, non-linear as well as linear.

Interpretation of the observed photoabsorption spectra in terms of the valence, Rydberg and mixed type transitions is a major involvement in the understanding of the structure of the excited states. Another vital issue is the assignment of the vibrational structure accompanying the electronic transitions, *i.e.*, vibronic transitions, which are related to several factors such as the geometry changes in the excited states, symmetry based selection rules and interactions between states. Isotopic substitution is a well-known tool for confirming vibronic assignments. In this context, VUV photoabsorption spectra of the deuterated analogues of the halogen and sulphur containing molecules (CD_2Cl_2, CD_2Br_2,

CD_2I_2 and CD_3SOCD_3) are also studied. This has greatly helped in verifying assignments or clarifying situations where discrepancies existed. Further, interpretation and assignments are supported by quantum chemical calculations.

A typical photoabsorption study of a molecule thus consists of three major parts: Acquiring the experimental spectra using synchrotron radiation, analysis of the spectral data, and quantum chemical computations of molecular structure and its correlation with the observed spectra. These issues including the synchrotron radiation source, VUV beamlines and the experimental workstations, theoretical concepts for interpretation of molecular photoabsorption spectra and the computational techniques are discussed in what follows. This chapter thus builds the requisite platform for work reported in the subsequent chapters.

1.1 SYNCHROTRON RADIATION

Electrons (or other charged particles) moving along curved trajectories under the influence of a magnetic field with relativistic speeds radiate electromagnetic radiation in a narrow cone in the forward direction of their motion. This highly collimated radiation is known as synchrotron radiation (SR). The total power (P) radiated by a relativistic charged particle of energy E when accelerated through a path of radius R is given by

$$P = \frac{2q^2c}{3R^2}\left(\frac{E}{mc^2}\right)^4 \tag{1.1}$$

in CGS units, where c is the speed of light, q and m are the charge and rest mass of the particle. In order to have high emitted power, electrons (or positrons) are usually chosen as the accelerating particle. A synchrotron radiation source (SRS) is essentially a storage ring in which relativistic electrons circulate for a long period, *i.e.*, few hours or more. Electrons are made to move in a closed path consisting of arced and straight sections, by an array of magnets known as the magnetic lattice, which consists of dipole (or bending) magnets, quadrupole magnets and sextupole magnets. The electrons emit SR during acceleration through the bending magnets. The quadrupole and sextupole magnets are used to focus the electron beam and maintain the closed trajectory. The energy loss due to emission of SR is replenished by radio frequency (RF) electric field cavities, installed in one or more straight sections of the ring, by supplying the right amount of energy to the electrons on every pass.

SR is a powerful and versatile light source and has revolutionized VUV and soft X-ray spectroscopy like never before. VUV spectroscopic investigations in early days were often constrained by the limitations of traditional light sources which were either very weak or not continuously tunable. With its unique properties like high brilliance, continuous tunability, well-defined pulsed time structure and polarization, etc. SR has established itself as one of the best light sources available. Since it is produced in ultra-high vacuum environment, it is spectroscopically pure unlike the traditional laboratory sources. In particular, in the VUV region it is the only source that offers both high intensity and tunability over a large spectral region. The work reported in this thesis is carried out using the Indian SR source Indus-1 at Raja Ramanna Centre for Advanced Technology (RRCAT), Indore, India.

1.1.1 INDUS 1 SYNCHROTRON RADIATION SOURCE

Indus-1 is a 450 MeV [4, 5] storage ring, with a critical wavelength of 61 Å, is designed to provide radiation in the range of ~30–2000 Å. A schematic diagram of the facility is shown in Figure 1.1. The injection of electrons into Indus-1 is carried out by a 20 MeV microtron [4] and a 450 MeV booster synchrotron. The electrons, generated by thermionic emission, are initially accelerated by the microtron to an energy of 20 MeV and then injected through the Transfer Line-1 (*cf.* Fig. 1.1), into the booster synchrotron where their energy is increased to 450 MeV. Finally, the 450 MeV electrons are extracted and injected into Indus-1 through Transfer Line-2 until the beam current in the storage ring reaches ~100 mA.

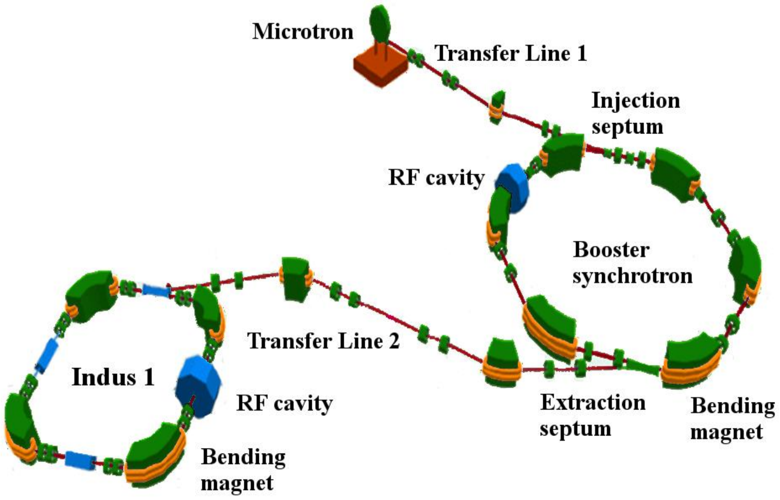

Fig. 1.1: A schematic diagram of the Indus-1 facility at RRCAT, Indore, India

The ring has a circumference of 18.6 m and is made up of four super periods of magnetic lattice connected by 1.3 m long straight sections. A super period consists of one dipole magnet with a field index of 0.5, a pair of doublets of quadrupoles and a pair of sextupoles. One of the straight sections is used to accommodate an RF cavity operating at 31.619 MHz, which provides replenishes the energy loss due to synchrotron radiation. The entire system is maintained under ultrahigh vacuum (UHV) of ~10^{-10} mbar to achieve a beam lifetime of a few hours in the ring. Of the several beamlines currently in operation at the Indus 1 facility, the Photophysics and the High Resolution VUV (HRVUV) beamlines operating in the VUV region are used for the work presented in this thesis.

1.1.2 THE PHOTOPHYSICS BEAMLINE AND EXPERIMENTAL STATION

The Photophysics beamline is a medium resolution beamline based on a Seya-Namioka monochromator and operates in the wavelength range of 500–3000 Å [6, 7]. It is suitable for photoabsorption, photoemission and photodissociation studies of molecules in gas and solid phases. A view of the Photophysics beamline and the schematics of experimental set-up for gas-phase spectroscopy are presented in Figures 1.2(a) and (b) respectively.

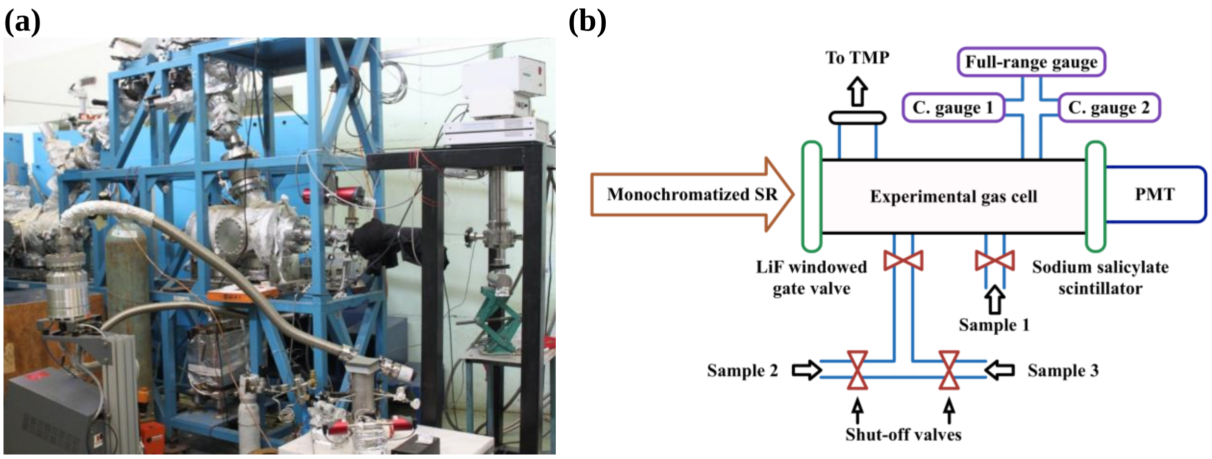

Fig. 1.2: (a) Photophysics beamline on Indus-1 sychrotron radiation source and (b) A schematic diagram of the gas-phase experimental setup on the Photophysics beamline

The beamline mainly consists of two toroidal mirrors mounted on UHV compatible mirror mounts housed in stainless steel chambers and the 1 m Seya-Namioka monochromator. The entire system is maintained under UHV of ~10^{-9} mbar using sputter ion pumps (SIPs). The SR from the tangent point of the bending magnet of Indus 1 is focused by the first toroidal mirror with acceptance angles of 48 mrad (hor.) x 6 mrad (ver.) onto the entrance slit of the monochromator. The Seya-Namioka monochromator is a constant deviation mount with a fixed angle of 70º15′ subtended at the grating by the entrance and exit arms. As the SR beam is more divergent in the horizontal direction, the Seya-Namioka monochromator is designed to operate in the vertical dispersion mode. Wavelength is scanned by rotating the grating about an axis parallel to the grooves passing through the pole of the grating. This is accomplished with the help of a stepper motor by translating the motion into a linear scale by a standard sine drive mechanism. The grating is coupled to the drive mechanism by a rotary based feedthrough. The dispersed light from the exit slit of the monochromator is focused by the second toroidal mirror on to the experimental cell. With a

2400 l/mm ion etched laminar grating mounted in the monochromator, a resolution of ~1.5 Å at 1500 Å is achieved.

Photoabsorption studies are performed in a gas phase experimental station (*cf.* Fig.1.2(b)) which is coupled to the beamline and mechanically isolated by a lithium fluoride windowed gate valve, limiting the optical transmission to >1050 Å (<95,240 cm^{-1}). The experiments are carried out in a 25 cm long single-pass stainless steel six-way cross gas cell. A schematic diagram of the experimental setup is shown in Figure 1.2. The cell is evacuated to a base pressure of 10^{-6} mbar by a turbo molecular pump (TMP) before introducing samples. The samples, when in liquid form at room temperature, are contained in a glass vial connected to the absorption cell by a glass-metal seal and several shut-off (Swagelok) valves. The samples are subjected to several freeze-pump-thaw cycles to get rid of volatile impurities before introduction into the cell. For gaseous samples, cylinders can be connected directly to the shut-off valves through standard ferrule connectors.

Sample pressures are measured using a set of two absolute capacitance gauges (C. gauges 1 and 2 in Fig. 1.2) of Pfeiffer make having ranges of 10^{-5}–10^{-1} and 10^{-2}–10^{2} mbar. Transmitted intensities are detected using a UV-visible sensitive photomultiplier tube (PMT) coupled with a sodium salicylate coated quartz window. Sodium salicylate works as a scintillator converting VUV photons into visible light through fluorescence. The visible light is then detected by the UV-visible PMT. The transmitted intensity through the evacuated cell (I_0) and through the sample (I) are measured and the absorption spectrum is obtained using the well known Beer-Lambert law

$$I = I_0 \mathrm{e}^{-\sigma(\lambda) n L}, \tag{1.2}$$

where $\sigma(\lambda)$ is the absorption cross section, n is the number density of molecules interacting with the beam and L is the absorption path length. The measured intensities are normalized with respect to the storage ring beam current which is recorded simultaneously at every step of 0.5 Å. The transmitted intensity and beam current at each step are monitored and recorded by the data acquisition system coupled to a personal computer. The calibration of the wavelength scale is achieved with the help of atomic absorption lines of xenon as a reference and using this method, the overall error in determination of line positions is found to be within the experimental resolution.

1.1.3 THE HRVUV BEAMLINE AND EXPERIMENTAL STATION

The High Resolution VUV (HRVUV) beamline is useful for photoabsorption studies of atoms and molecules in the wavelength region of 1150–3000 Å [8]. The beamline is constituted of three major components, a pre-focusing optical system, an experimental cell for gas phase studies and a 6.65 m long VUV spectrometer. The VUV spectrometer and schematics of the gas handling system of HRVUV are displayed in Figure 1.3(a) and (b) respectively.

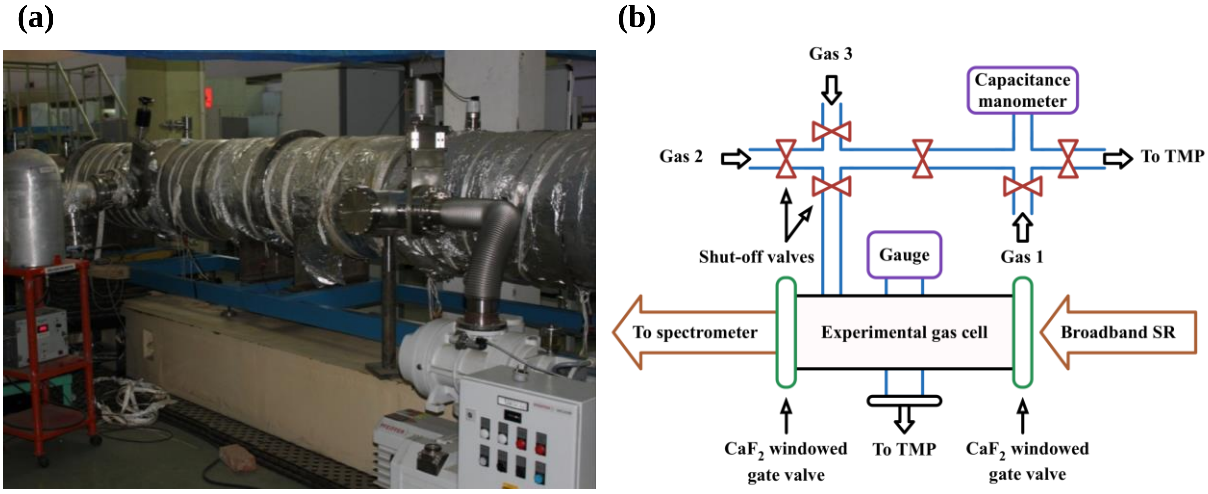

Fig. 1.3: (a) The 6.65 m off-plane Eagle spectrometer and (b) A schematic diagram of the gas-phase experimental setup at the HRVUV beamline

The pre-focusing optics consists of three concave cylindrical mirrors. The first mirror (M1), with a radius of curvature $r = 0.881\text{m}$, collimates the synchrotron radiation from the bending magnet in the horizontal direction while acting as a plane mirror in vertical direction. The collimated beam from M1 is focused in the horizontal plane by the second mirror (M2) with $r = 4.513\,\text{m}$. M2 acts as a plane mirror in the vertical direction. The third mirror (M3) with $r = 38.6\,\text{m}$ focuses the SR beam from M2 in the vertical plane, while acting as a plane mirror in the horizontal plane, to the entrance slit of the spectrometer. The cylindrical axes of the mirrors M1 and M2 lie in the vertical plane while that of M3 lies in the horizontal plane.

The spectrometer is based on a concave spherical grating of radius of curvature 6.65 m in off-plane Eagle mount (*cf.* Fig. 1.3(a)). A particular central wavelength selection is done by rotating the grating about the horizontal axis passing through its pole and parallel to the grooves and entrance and exit slits. In order to focus the dispersed wavelength on the Rowland circle, the grating is translated along the axis of the spectrometer. The spectrometer chamber is kept at a vacuum of ~10^{-6} mbar. The transmitted intensity is scanned by moving an assembly of the exit slit and a UV-visible sensitive PMT vertically along the focal plane (on the Rowland circle). The PMT is coupled with a sodium salicylate coated quartz window which acts as a scintillator. The exit slit-PMT assembly can cover a total distance of 160 mm along the vertical focal plane. This movement gives a wavelength scanning range of 200 Å and a resolution of ~0.5 Å with a 1200 ln/mm (Al+MgF_2) coated grating.

Gas phase photoabsorption studies are performed in a 30 cm long cylindrical stainless steel cell with several ports (*cf.* Fig. 1.3(b)). The cell is placed between the pre-focusing mirror system and the entrance slit of the spectrometer and is isolated on both sides by UHV gate valves fitted with CaF_2 windows which limit the optical transmission to 1250 Å (80,000 cm^{-1}). A schematic diagram of the experimental setup is shown in Figure 1.3. The cell is evacuated to a base pressure of 10^{-6} mbar using a TMP. The sample introduction system and experimental procedures are similar to those described for the Photophysics beamline. A microcontroller based data acquisition system interfaced with a personal computer is used for controlling the grating rotation, grating translation and PMT scanning as well as acquiring the data. The calibration of the spectra is done using the standard atomic lines of xenon and molecular bands of oxygen.

1.2 MOLECULAR ELECTRONIC STATES: THEORETICAL BACKGROUND

1.2.1 GROUP THEORY AND MOLECULAR SYMMETRY

Group theory is the mathematical theory of symmetry and a powerful tool that simplifies the process of obtaining a variety of useful information about molecules [9, 10]. A symmetry operation transforms a molecule in such a way that the final orientation is physically indistinguishable from the initial orientation. Symmetry elements are geometrical entities (a point, line or plane) with respect to which symmetry operations are carried out. Besides the identity operation (E), which simply leaves the molecule unchanged, there are only four types of symmetry operations needed to be considered. They are inversion about a point (i), reflection with respect to a vertical or horizontal plane (σ), rotation about an axis (C_n) and rotation followed by reflection (S_n) also known as an improper rotation. Here n in the subscripts denotes a rotation by an angle of $2\pi/n$. The set of all symmetry operations of a molecule forms a mathematical group; called a point group since the centre of mass of the isolated molecule remains fixed during any of the symmetry operations. A molecule is assigned to a point group by identifying its symmetry elements. The molecular Hamiltonian is invariant under the symmetry operations of the point group to which molecule belongs.

The matrix representation of a point group is a set of matrices, one for each element of the group, which satisfy the group multiplication table. If it is possible, using some similarity transformation, to bring the set of matrices into a block diagonal form so that each block forms a representation of the group, the original set of matrices is called a reducible representation. If it is not possible to further reduce all the matrices in this manner, then the representation is called irreducible. A character table of a point group is a table which displays the characters (*i.e.*, traces of the matrices) of the irreducible representations (also known as symmetry species) of that point group, arranged in a particular way. The irreducible representations of a point group are the ones which are of fundamental importance in deducing various properties of the molecule.

Molecules studied in this thesis belong to C_{2v} (CH_2X_2, CD_2X_2, X=Cl, Br, I), C_s (CH_3SOCH_3, CD_3SOCD_3) and $C_{\infty v}$ (N_2O) point groups respectively. A molecule belonging to the C_{2v} point group has a C_2 axis and two vertical symmetry planes (σ_v and $\sigma_{v'}$) containing the C_2 axis. A molecule having only a plane (σ_h) as a symmetry element belongs to the C_s point group. A molecule belonging to $C_{\infty v}$ point group has an axis of rotation of infinite order (C_∞) and infinite number of vertical reflection planes (σ_v). The character tables of these point groups are given in Tables 1.1–1.3 [10].

Table 1.1: Character table for C_s point group

C_s	E	σ_h		
A′	1	1	x, y, R_z	x^2, y^2, z^2, xy
A″	1	-1	z, R_x, R_y	yz, zx

Table 1.2: Character table for C_{2v} point group

C_{2v}	E	C2	σ_v(xz)	σ_v'(xz)		
A_1	1	1	1	1	Z	x^2, y^2, z^2
A_2	1	1	-1	-1	R_z	xy
B_1	1	-1	1	-1	x, R_y	zx
B_2	1	-1	-1	1	y, R_z	yz

Table 1.3: Character table for $C_{\infty v}$ point group

$C_{\infty v}$	E	$2C_\infty$	$3C_\infty$	$\infty\sigma_v$		
Σ^+	1	1	…	1	z	x^2+y^2, z^2
Σ^-	1	1	…	-1	R_z	(zx, yz)
Π	2	2cosφ	…	0	(x, y); (R_x, R_y)	(x^2-y^2, xy)
Δ	2	2cos2φ	…	0		
Φ	2	2cos3φ	…	0		
…	…	…	…	…		

Character tables can be used to deduce selection rules, *i.e.*, allowed or forbidden transitions, without the need of detailed quantum mechanical calculations. For vibronic transitions, the electric dipole selection rule is given by the transition moment R_{ev}

$$R_{ev} = \int \psi_e'^* \psi_v'^* \hat{\mu} \psi_e'' \psi_v'' \, d\tau_{ev} \,, \tag{1.3}$$

where ψ_e and ψ_v are electronic and vibrational wavefunctions respectively, $\hat{\mu}$ is the dipole moment operator and primes and double-primes denote the upper and lower states respectively [9]. The group theoretical form of the vibronic selection rule is given by

$$\Gamma(\psi_e')\times\Gamma(\psi_v')\times\Gamma(\mu)\times\Gamma(\psi_e'')\times\Gamma(\psi_v'')\supset A, \tag{1.4}$$

where the A stands for the totally symmetric species of the point group and Γ stands for an irreducible representation.

1.2.2 VALENCE, RYDBERG AND INTERMEDIATE STATES

The excited states of a molecule are obtained by promoting an electron from one of the filled molecular orbitals (MOs) in the ground state to higher MOs [11]. Electronic states of a molecule can be classified as Rydberg, valence and intermediate type, depending on the nature of the final orbitals involved in the transitions [12]. A qualitative understanding of this qualification may be developed using the the LCAO-MO (linear combination of atomic orbitals- molecular orbitals) framework, in which the MOs are constructed from the constituent atomic orbitals (AOs). In this picture, the valence MOs are those constructed from AOs that have their maximal principal quantum number (1 for H, 2 for C, 3 for Cl, etc.) [13]. In the ground state of the molecule these MOs are fully or partially occupied and are called the outer shell MOs. If the principal quantum number of one of the constituent AOs is less than the maximal, such MOs are called inner shell MOs. A transition from the ground state to a MO in which one or more of the constituent AOs have principal quantum number higher than in the ground state is termed a Rydberg transition and the final MO is said to be Rydberg in nature. The excited molecule may be approximated quantum mechanically to a hydrogenic system in which the nuclei and the rest of the occupied MOs form the core for the excited Rydberg electron. Transitions to MOs in which the principal quantum number is the same are termed as valence. Rydberg MOs are diffuse in extent as compared to valence MOs. This qualitative picture is based on atomic concepts and in practice one finds many instances of mixed character transitions in molecules.

As in the atomic case, molecular Rydberg series converging to an ionization potential (IP) may be described by the standard Rydberg formula

$$E_n = IP - \frac{R}{\left(n-\delta_l\right)^2}, \tag{1.5}$$

where R is the Rydberg constant, n is the principal quantum number, δ_l is the quantum defect (QD). The QD accounts for the screening of the core and depends on the extent of penetration of the orbital. Thus the QD has a dependence on the orbital angular momentum l and in general, $\delta(ns) > \delta(np) > \delta(nd)$; which means that for Rydberg transitions having a particular n, $E(ns) < E(np) < E(nd)$. There could also be a lifting of degeneracy of components of levels with $l \geq 1$ due to the asymmetry of the core, characterized by the azimuthal number λ. However, unlike in atomic case, molecular Rydberg transitions may not always be sharp and intense [14].

The valence/Rydberg interpretation can also be understood in terms of the bonding/antibonding/non-bonding nature of the MOs involved. For example, if the excitation is from a non-bonding to antibonding MO, the molecular core is more tightly bound in the excited state than in the ground state, and the molecule may be approximated to a hydrogenic system even if the principal quantum number is not very high [11]. It may be noted that, especially in cases where the excitation is from a non-bonding or atomic like MO, molecular QD values are close to the corresponding atomic QDs, but they may be somewhat modified by the molecular environment. While there are states which are predominantly Rydberg (or valence) at any molecular geometry there are many intermediate cases where the Rydberg/valence nature changes with the geometry [12]. For high lying Rydberg states, the situation is more atomic-like while for low Rydberg states, mixing is common which complicates their spectral interpretation. These low lying Rydberg states are very important in photochemistry and it has been suggested that photochemical reactions occurring through excited states may depend systematically on the nature of the state, extent of valence-Rydberg mixing, etc. [15]. This has provided the motivation to investigate the valence/Rydberg nature of excited states of all the molecules studied in this thesis.

1.2.3 VIBRONIC STRUCTURE

Transitions from various vibrational levels of one electronic state to those of another give rise to vibronic structure in the spectrum of a molecule (*cf.* Fig. 1.4). While the intensities of these vibronic transitions are governed by the Franck-Condon principle, the expected band origin ν_{00} under harmonic approximation is given by

$$\nu_{00} = E' - E'' + (\mathrm{ZPE})' - (\mathrm{ZPE})'', \tag{1.6}$$

where primes and double-primes denote the upper and lower electronic states respectively, *E*’s are the equilibrium electronic energies and ZPE’s are the zero point energies which are given by $\sum_{i=1}^{3M-6} \omega_i / 2$, ω_i being the frequencies of the (3*M*–6) vibrational modes of a molecule having *M* nuclei. Analysis of the observed vibronic structure presupposes a knowledge both upper and lower state vibrational frequencies.

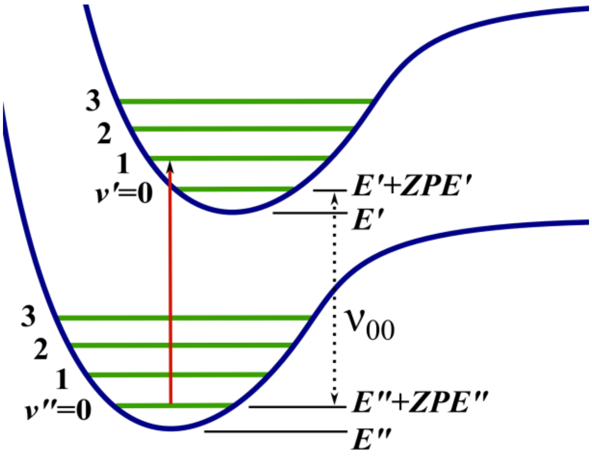

Fig. 1.4: Vibronic levels of a diatomic molecule showing equilibrium electronic energies *E′*, *E″* and zero point energies *ZPE′*, *ZPE″*

The vibrational frequencies in excited states of molecules are not generally known and the situation is complicated by the fact that the geometry of the molecule and hence the vibrational frequencies are different from those of the ground state. In practice, unless vibrational frequencies in the excited states are known from experiment or computation, it is difficult to carry out vibronic assignments. In this context, vibrational frequencies of the cationic ground state of a molecule are generally good estimates of the corresponding frequencies in excited Rydberg states (described by a positive ionic core and an excited electron far away from it) and are useful in assignment of vibronic transitions [16-18]. Another useful tool in the analysis of vibrational structure of electronic transitions is the isotope shift. Under Born-Oppenheimer approximation, the electronic energy levels do not change when an atom in a molecule is substituted by its isotope. The isotopic shift in the band origin can be approximated by

$$\left(\nu_{00}\right)_a - \left(\nu_{00}\right)_b = \left[(\mathrm{ZPE})' - (\mathrm{ZPE})''\right]_a - \left[(\mathrm{ZPE})' - (\mathrm{ZPE})''\right]_b, \tag{1.7}$$

where the subscripts *a* and *b* denote the two isotopologues. This can be used to verify or consolidate assignments of vibrational features and has been used effectively in the present thesis by comparing the spectra of the dihalomethanes with their deuterated isotopologues (CH_2X_2, CD_2X_2, X=Cl, Br, I).

1.3 COMPUTATIONAL METHODS

All the computations of molecular structure presented in this thesis are performed using GAMESS (US) [19] quantum chemistry code. For visualization of the molecular orbitals the software MacMolPlt [20] is used. The basic principles on which the computational techniques are based are discussed briefly in this section.

The many body Schrödinger equation for molecules cannot be solved in a straightforward manner owing to the electron-electron interaction and that calls for suitable approximate methods. The Hamiltonian of a molecular system, in atomic units, consisting of *M* nuclei and *N* electrons can be written as

$$\hat{H} = -\frac{1}{2}\sum_{i=1}^{N}\nabla_i^2 - \frac{1}{2}\sum_{A=1}^{M}\nabla_A^2 - \sum_{i=1}^{N}\sum_{A=1}^{M}\frac{Z_A}{r_{iA}} + \sum_{i=1}^{N}\sum_{j>1}^{N}\frac{1}{r_{ij}} + \sum_{A=1}^{M}\sum_{B>A}^{M}\frac{Z_A Z_B}{r_{AB}}, \tag{1.8}$$

where *A*, *B* run over the *M* nuclei and *i*, *j* run over the *N* electrons in the system; r_{AB} denotes the distance between particles *a* and *b*; Z_A is the atomic number on nucleus *A*. First two terms denote the kinetic energies (KEs) of electrons and nuclei. The other three terms describe the attractive electrostatic interaction between the nuclei and the electrons and repulsive potentials due to electron-electron and nucleus-nucleus interactions. Under the Born-Oppenheimer approximation, the electrons being much lighter are considered as moving in the field of fixed nuclei. The electronic Hamiltonian then may be written as

$$\hat{H}_{\mathrm{el}} = -\frac{1}{2}\sum_{i=1}^{N}\nabla_i^2 - \sum_{i=1}^{N}\sum_{A=1}^{M}\frac{Z_A}{r_{iA}} + \sum_{i=1}^{N}\sum_{j>i}^{N}\frac{1}{r_{ij}} = \hat{T} + \hat{V}_{\mathrm{Ne}} + \hat{V}_{\mathrm{ee}}\,. \tag{1.9}$$

The total electronic energy (U) including nuclear-nuclear interaction is given by

$$U = \left\langle \hat{H}_{\mathrm{el}} + \hat{V}_{\mathrm{NN}} \right\rangle, \tag{1.10}$$

$$\hat{V}_{\mathrm{NN}} = \sum_{A=1}^{M}\sum_{B>A}^{M}\frac{Z_A Z_B}{r_{AB}}\,. \tag{1.11}$$

1.3.1 THE HARTREE-FOCK SELF CONSISTENT FIELD METHOD

In the Hartree-Fock (HF) method each electron is considered to be moving in the electrostatic field of the *M* nuclei and the average field of the other (*N*–1) electrons. The ground state electronic wavefunction $|\Psi_0\rangle$ is approximated by an antisymmetrized product of *N* orthonormal spin orbitals $\varphi_i(\vec{x})$ and is given by a single Slater determinant

$$|\Psi_0\rangle \approx |\Psi_{\mathrm{HF}}\rangle = \frac{1}{\sqrt{N!}}\begin{vmatrix} \varphi_1(\vec{x}_1) & \varphi_2(\vec{x}_1) & \dots & \varphi_N(\vec{x}_1) \\ \varphi_1(\vec{x}_2) & \varphi_2(\vec{x}_2) & \dots & \varphi_N(\vec{x}_2) \\ \vdots & \vdots & \vdots & \vdots \\ \varphi_1(\vec{x}_N) & \varphi_2(\vec{x}_N) & \dots & \varphi_N(\vec{x}_N) \end{vmatrix}, \tag{1.12}$$

where $\vec{x}_1 = (\vec{r}_i, \sigma_i)$, $\vec{r}_i$ and σ_i being the position and spin of the *i*-th electron respectively. Now using the variational method, $\varphi_i(\vec{x})$ are found out for which $|\Psi_{\mathrm{HF}}\rangle$ minimizes the total energy

$$E_{\mathrm{HF}} = \frac{\langle \Psi_{\mathrm{HF}} | \hat{H}_{\mathrm{el}} | \Psi_{\mathrm{HF}} \rangle}{\langle \Psi_{\mathrm{HF}} | \Psi_{\mathrm{HF}} \rangle}, \tag{1.13}$$

subject to the constraints that the spinorbitals are orthonormal. The application of this minimization procedure leads to the HF differential equations for the individual spinorbitals

$$\hat{f}\varphi_i = \varepsilon_i \varphi_i,\ i = 1, 2, \dots, N, \tag{1.14}$$

where ε_i are the eigenvalues of the effective one-electron operator $\hat{f}$ *i.e.*, the Fock operator,

$$\hat{f}(1) = -\frac{1}{2}\nabla_1^2 - \sum_{A=1}^{M} \frac{Z_A}{r_{1A}} + \sum_{j=1}^{N} (\hat{J}_j(\vec{x}_1) - \hat{K}_j(\vec{x}_1)), \tag{1.15}$$

$$\hat{J}(\vec{x}_1) = \int |\varphi_j(\vec{x}_2)|^2 \frac{1}{r_{12}} \mathrm{d}\vec{x}_2 \ . \tag{1.16}$$

The Coulomb operator of Eq. (1.16) represents the potential that an electron at $\vec{x}_1$ experiences due to the average charge distribution of another electron in the spin orbital φ_j .The exchange operator $\hat{K}_j$ is defined through its effect when operating on a spin orbital $\varphi_i(\vec{x}_1)$ as

$$K_j(\vec{x}_1)\varphi_i(\vec{x}_1) = \int \varphi_j^*(\vec{x}_2)\frac{1}{r_{12}}\varphi_i(\vec{x}_2)\,\mathrm{d}\vec{x}_2\,\varphi_j(\vec{x}_1)\,. \tag{1.17}$$

Since the HF potential depends on $\varphi_i(\vec{x})$, the HF equations are solved self-consistently.

There are three types of HF wavefunctions used for calculations. The restricted HF (RHF) wavefunctions are used for closed shell atoms or molecules, characterized by an even number of electrons, a singlet spin state and zero orbital angular momentum. The restricted open-shell HF (ROHF) wavefunctions are used for systems having a non-zero spin or orbital angular momentum. In this case, spatial orbitals may be singly or doubly occupied. The unrestricted HF (UHF) wavefunctions are used for the same class of molecules as the ROHF. The difference is that the spatial orbitals for the electrons with opposite spins are different. There are no doubly occupied spatial orbitals. The HF SCF wave function takes into account the interactions between electrons only in an average way. It does not take into account the instantaneous Coulomb interaction between electrons; *i.e.*, the electron correlation.

1.3.2 MØLLER-PLESSET PERTURBATION THEORY

Møller-Plesset (MP) theory uses perturbation theory to correct the electron correlation in a many electron system. The sum of one electron Fock operators, defined in Eq. (1.15) is taken as the unperturbed Hamiltonian, $\hat{H}^{(0)} = \sum_{i=1}^{N} \hat{f}(i)$. The eigenfunctions of $\hat{f}$ are the occupied and virtual Hartree-Fock orbitals of the system and the eigenvalues are the associated one-electron energies. The HF wavefunction (*cf.* Eq. (1.12)) is an eigenfunction of $\hat{H}^{(0)}$ with an eigenvalue $\sum_{i=1}^{N}\varepsilon_i$, *i.e.*, the sum of the one electron energies of the occupied spin orbitals. The perturbing Hamiltonian $\hat{H}'$ is the difference between the true molecular Hamiltonian $\hat{H}_{\mathrm{el}}$ and $\hat{H}^{(0)}$, *i.e.*, $\hat{H}' = \hat{H}_{\mathrm{el}} - \hat{H}^{(0)}$. The first order correction to the ground state energy is given by $\langle\psi_0|\hat{H}'|\psi_0\rangle$, giving the total energy equal to the Hartree-Fock energy E_{HF},

$$E^{(1)} = \langle\psi_0|\hat{H}^{(0)} + \hat{H}'|\psi_0\rangle = \langle\psi_0|\hat{H}_{\mathrm{el}}|\psi_0\rangle = E_{\mathrm{HF}}. \tag{1.18}$$

The second order correction to the ground state energy is given by,

$$E_0^{(2)} = \sum_{P\neq 0} \frac{\left|\langle\psi_P|\hat{H}'|\psi_0\rangle\right|^2}{E_0^{(0)} - E_P^{(0)}}, \tag{1.19}$$

where $|\psi_P\rangle$ is a multiply excited determinant and an eigenfunction of $\hat{H}^{(0)}$ with eigenvalue $E_P^{(0)}$. It can be shown that the matrix elements $\langle\psi_P|\hat{H}'|\psi_0\rangle$ are non-zero only for doubly excited Slater determinants and $E_0^{(2)}$ can be expressed as

$$E_2^{(0)} = \frac{1}{4}\sum_{a,b}^{occ}\sum_{p,q}^{vir} \frac{(ab\,||\,pq)(pq\,||\,ab)}{\varepsilon_a + \varepsilon_b - \varepsilon_p - \varepsilon_q}, \tag{1.20}$$

$$\begin{aligned}(ab\,||\,pq) &= \int \varphi_a^*(\mathrm{x}_1)\varphi_b^*(\mathrm{x}_2)\frac{1}{r_{12}}\varphi_p(\mathrm{x}_1)\varphi_q(\mathrm{x}_2)\,\mathrm{dx}_1\,\mathrm{d}x_2 \\ &\quad - \int \varphi_a^*(\mathrm{x}_1)\varphi_b^*(\mathrm{x}_2)\frac{1}{r_{12}}\varphi_q(\mathrm{x}_1)\varphi_p(\mathrm{x}_2)\,\mathrm{dx}_1\,\mathrm{d}x_2,\end{aligned} \tag{1.21}$$

where φ_a and φ_b are occupied spin orbitals and φ_p and φ_q are virtual spin orbitals. An MP computation to nth order is called as MPn. While calculations at MP2 level provide good agreement with experimental values, the perturbation theory can be extended to include higher order energy corrections, *i.e.*, MP3, MP4 etc. [21].

1.3.3 THE DENSITY FUNCTIONAL THEORY

The density functional theory (DFT) has become one of the most important tools in electronic structure theory for predicting a broad range of properties of molecules in the ground state with a low computational cost and reasonable accuracy. DFT formally scales as

$\aleph^3$ where $\aleph$ is the number of basis functions (with charge fitting), and including the effects of electron correlation at some reasonable level while conventional ab-initio MO theory formally scales as $\aleph^4$ at the HF level [22].

The basic idea behind DFT is that the energy of an electronic system can be written in terms of the electron probability density $\rho(\vec{r})$. Underlying the DFT are two theorems by Hohenberg and Kohn (HK). According to the first theorem, the ground state electronic energy E_0 is a unique functional of the ground state electron probability density $\rho(\vec{r})$, *i.e.* $E_0 \equiv E_0[\rho]$. The second theorem states that the true ground state electron density minimizes the energy functional $E_0[\rho]$. If the $\rho(\vec{r})$ is known then it is possible to calculate all the ground state molecular properties from it, without the necessity of finding the molecular wavefunction. While the many-body electronic wave-function is a function of 3*N* spatial variables, the density is a simple function that depends solely on three spatial variables $\vec{r} = (x, y, z)$ [23]. Kohn and Sham showed that the energy functional can be explicitly written as,

$$E[\rho] = -\frac{1}{2}\sum_{i=1}^{N}\int \psi_i^*(\vec{r}_1)\nabla^2\psi_i(\vec{r}_1)\,\mathrm{d}\vec{r}_1 - \sum_{A=1}^{M}\int \frac{Z_A}{r_{A1}}\rho(\vec{r}_1)\,\mathrm{d}\vec{r}_1 + \frac{1}{2}\iint \frac{\rho(\vec{r}_1)\rho(\vec{r}_2)}{r_{12}}\,\mathrm{d}\vec{r}_1\mathrm{d}\vec{r}_2 + E_{\mathrm{XC}}[\rho], \quad (1.22)$$

where ψ_i (i = 1, 2,…, N) are the Kohn-Sham (KS) orbitals and the exact ground-state electron density is given by

$$\rho_s(\vec{r}) = \sum_{i=1}^{N}\sum_{m_s}\left|\psi_i(\vec{r}, m_s)\right|^2 . \quad (1.23)$$

The first term on the right in Eq. (1.22) represents the kinetic energy of the electrons; the second term corresponds to the electron-nucleus attraction; the third term represents the Coulomb interaction between the total charge distribution at $\vec{r}_1$ and $\vec{r}_2$; the last term is the exchange-correlation energy of the system, which is also a functional of the density and takes into account all non-classical electron-electron interactions. The true form of the exchange-correlation functional is not known and in practical calculations, some approximations to E_{XC} are used [24]. Traditionally, E_{XC} is broken up into exchange (E_{X}) and correlation (E_{C}) parts. Now the variational principle is applied to minimize the energy and the resulting equation, called KS equation, is given by

$$\left(-\frac{1}{2}\nabla_1^{\,2}-\sum_{A=1}^{M}\frac{Z_A}{r_{A1}}+\int\frac{\rho(\vec{r}_2)}{r_{12}}\mathrm{d}\vec{r}_2+V_{\mathrm{XC}}(\vec{r}_1)\right)\psi_i(\vec{r}_1)=\varepsilon_i\psi_i(\vec{r}_1)\,, \tag{1.24}$$

where the exchange correlation potential V_{XC} is defined as the functional derivative of E_{XC} with respect to ρ, *i.e.*,

$$V_{\mathrm{XC}}=\delta E_{\mathrm{XC}}/\delta\rho\,. \tag{1.25}$$

If E_{XC} is known, then V_{XC} can be obtained. Calculations start with an initial trial electron density giving a KS potential via Eq. (1.25); the KS equations are then solved and a new density is found. This iterative cycle is repeated until a convergence criterion is reached.

Numerous schemes have been developed for obtaining approximate forms for the functional for the exchange-correlation energy. The main source of error in DFT usually stems from the approximate nature of E_{XC}. In the Local Density Approximation (LDA), it is assumed that the density can be treated as a uniform electron gas, and is the basis of all approximate exchange correlation functionals. Its form is given by

$$E_{\mathrm{XC}}^{\mathrm{LDA}}=\int\rho(\vec{r})\varepsilon_{\mathrm{XC}}(\rho)\,\mathrm{d}\vec{r}\,, \tag{1.26}$$

where $\varepsilon_{\mathrm{XC}}(\rho)$ is the exchange plus correlation energy per electron in a homogeneous electron gas of constant density ρ. Improvements over the LDA approach must consider a non-uniform electron gas. This can be achieved by making the exchange and correlation energies dependent not only on the electron density but also on the derivatives of the density.

LDA with gradient (first derivative) corrections, which is called the generalized gradient approximation (GGA) yields better accuracy. A variety of exchange-correlation functionals, having names such as B3LYP, BLYP , PBE0 and so on, have been developed for use in DFT calculations; where the names designate a particular pairing of GGA exchange and correlational functionals. For example, in the BLYP exchange-correlation functional, B (Becke) is the standard GGA for exchange and LYP (Lee-Yang-Parr) for correlation [25]. In this thesis, the B3LYP and PBE0 functionals have been used.

1.3.4 TIME-DEPENDENT DENSITY FUNCTIONAL THEORY

The time-dependent density functional theory (TDDFT) is useful for the investigation of the response of molecular systems to electric and magnetic fields and as well as for calculating excited state energies [21]. Excited state energies are calculated using the linear (first-order) time-dependent response of the ground state electron density to an external oscillatory time-dependent electric field. The ground state electron density ρ_0 is calculated using time-independent KS equation [26]. The basis of TDDFT is the Runge-Gross (RG) theorem [27] which states that, for a given initial wavefunction, particle statistics and interaction, a given time-dependent density can arise from at most one time-dependent external potential. RG theorem is the time-dependent analogue of the HK theorem [28] and implies that time-dependent potential (and all other properties) is a functional of the time-dependent density. It is then possible to define time-dependent Kohn-Sham (TDKS) equations, which describe non-interacting electrons that evolve in a time-dependent KS potential but produce the same density as that of the interacting system of interest. Thus the time dependent Schrödinger equation is replaced by the time-dependent KS equations

$$\left\{-\frac{1}{2}\nabla_1^2-\sum_{I=1}^{M}\frac{Z_I}{r_{I1}}+\int\frac{\rho(\vec{r}_2,t)}{r_{12}}d\vec{r}_2+V_{\mathrm{ext}}(t)+V_{\mathrm{XC}}(\vec{r}_1,t)\right\}\psi_i(\vec{r}_1,t)=i\frac{\partial}{\partial t}\psi_i(\vec{r}_1,t)\,, \qquad (1.27)$$

$$\rho(\vec{r},t)=\sum_{i=1}^{N}\left|\psi_i(\vec{r},t)\right|^2, \tag{1.28}$$

where the external potential V_{ext} (for example, the oscillating electromagnetic field), the exchange-correlation potential V_{XC}, the KS orbitals and the density are all time-dependent. Usually the adiabatic approximation is used wherein the functional dependence of $V_{\mathrm{XC}}(\vec{r},t)$ on $\rho(\vec{r},t)$ is assumed to same as in DFT.

The linear response in ω-space [29] can be formally written as

$$\delta\rho(\vec{r}_1,\omega)=\int\chi[\rho_0](\vec{r}_1,\vec{r}_2,\omega)\delta V_s(\vec{r}_2,\omega)\,\mathrm{d}\vec{r}_2, \tag{1.29}$$

$$\delta V_s(\vec{r}_1,\omega)=\delta V_{\mathrm{ext}}(\vec{r}_1,\omega)+\int\frac{\delta\rho(\vec{r}_2,\omega)}{r_{12}}\mathrm{d}\vec{r}_2+\int f_{\mathrm{XC}}(\vec{r}_1,\vec{r}_2,\omega)\delta\rho(\vec{r}_2,\omega)\,\mathrm{d}\vec{r}_2, \tag{1.30}$$

where f_{XC} is defined as the Fourier transform of the functional derivative of $V_{\mathrm{XC}}(\vec{r},t)$ with respect to the time-dependent density $\rho(\vec{r},t)$, evaluated at the ground state density:

$$f_{XC}(\vec{r}_1,\vec{r}_2,\omega)=\left.\frac{\delta V_{XC}[\rho](\vec{r}_1,\omega)}{\delta\rho(\vec{r}_2,\omega)}\right|_{\rho_0(\vec{r}_1)}. \tag{1.31}$$

In Eq. (1.29), χ is the KS response function constructed from KS energies and orbitals [30] and is given by

$$\chi[\vec{r}_1,\vec{r}_2,\omega]=\lim_{\eta\to0+}\sum_{j,k=1}^{\infty}(f_j-f_k)\frac{\psi_j(\vec{r}_1)\psi_k^*(\vec{r}_1)\psi_j^*(\vec{r}_2)\psi_k(\vec{r}_2)}{\omega-(\varepsilon_j-\varepsilon_k)+i\eta}, \tag{1.32}$$

where f_j and f_k are the occupation numbers (0 or 1) of the KS orbitals in the ground state. ε_j are the KS energies in the time-independent KS equation. Since the perturbation $\delta V_s(\vec{r}_1,\omega)$ depends on the response function $\delta\rho(\vec{r}_1,\omega)$, Eq. (1.29) is solved self-consistently. When there is no external perturbation $(V_{\mathrm{ext}}=0)$, $\delta V_{\mathrm{ext}}(\vec{r}_1,\omega)$ is set to zero in Eq. (1.30). In this case $\delta\rho(\vec{r}_1,\omega)=0$ for all ω except for certain frequencies Ω corresponding to the excitation energies of the unperturbed molecule and $\rho(\vec{r}_1,\Omega)$ is the profile of the associated electronic eigenmode [29]. If the KS orbitals are assumed to be real and f_{XC} is frequency independent then the eigen frequencies can be obtained from the following equation:

$$\sum_{i',a'}\left[\delta_{ii'}\delta_{aa'}\left(\omega_{ia}^2-\Omega^2\right)+2\sqrt{\omega_{ia}\omega_{i'a'}}K_{ia,i'a'}\right]Z_{i'a'}=0\,. \tag{1.33}$$

This equation is analogous to classical eigenvalue equation of small oscillations yielding the eigen frequencies Ω and the eigenmodes Z_{ia} of the system.

The TDDFT method for excited states gives a combination of accuracy and low computational cost. In particular it has been shown that TDDFT calculated vertical excitation energies are fairly accurate up to the energy of the HOMO plus 1 eV when the PBE0 functional is used [31]; the accuracy however is poor for highly excited states or Rydberg states (diffused upper state orbitals) [32]. The extent of spatial overlap between the occupied and virtual orbitals involved in an excitation is measured using a quantity called lambda diagnostic parameter $(0 \le \Lambda \le 1)$ [32]. In general higher values of Λ indicate higher accuracy than low Λ values. The Λ value may also be used as an indication of the nature of the excitation. Transitions with low Λ values (≤0.3) are interpreted as predominantly Rydberg in nature while high Λ values (≥0.5) signify largely valence nature. Intermediate values of Λ indicate that the transition has a valence-Rydberg mixed nature.

1.3.5 BASIS SETS

Quantum-mechanical computational methods usually begin with the choice of a set of basis functions which are used to express the molecular orbitals (or KS orbitals in DFT). The MOs are expressed as a linear combination of a set of $\aleph$ basis functions $\psi_i=\sum_{j=1}^{\aleph}c_{ji}\chi_i$ where χ_i is a contracted Gaussian function (CGTF) which is itself taken to be a fixed linear combination of Gaussian functions. Several methods exist to form the CGTFs. The simplest type of basis set is a minimal basis set in which one function is used to represent each of the orbitals. Significant improvement is achieved by replacing each basis function in the minimal basis set by two or more basis functions, called double-zeta (DZ), triple-zeta (TZ), etc. A split-valence basis set uses two (or more) CGTFs for each valence AO but only one CGTF for each inner-shell (core) AO and designated as valence double zeta (VDZ), valence triple zeta (VTZ), etc.

A commonly used set of split valence basis sets developed by Pople and co-workers [33] is designated as *k-nlmG* where *k* refers to the number of primitive GTOs (PGTOs) used to represent core orbitals, *nl* and *nlm* indicate the numbers of inner and outer valence PGTOs in double and triple split valence respectively. For example, 6-311G is a triple split valence basis set where the core orbitals are a contraction of six PGTOs and the valence is split into three functions, represented by three, one and one PGTOs, respectively. To allow for the polarization due to distortion of the AOs as the atoms approach each other to form the molecule, one adds basis-function CGTFs whose *l* quantum numbers are greater than the maximum of the valence shell. For molecules in which significant electron density is expected at large distances from the nuclei, better accuracy is obtained by adding diffuse functions with small orbital exponents [34, 35].

The correlation consistent polarized basis sets cc-pV*n*Z, aug-cc-pV*n*Z (*n*=D, T, Q, 5) developed by Dunning and co-workers [36, 37] are geared towards recovering the correlation energy of the valence electrons. The augmented sets (aug-cc-pV*n*Z) are obtained by additions of diffuse primitive non-polarization and polarization functions to the cc-pV*n*Z basis sets [35]. In this thesis, most of the computational results were obtained using 6-311G and cc-pV*n*Z, aug-cc-pV*n*Z (*n*=D, T, Q, 5) basis sets.

1.3.6 GEOMETRY OPTIMIZATION AND VIBRATIONAL FREQUENCIES

The electronic energy U is a function of the 3M–6 independent nuclear coordinates $(q_1, q_2, \ldots, q_{3M-6})$ which define the geometry of the molecule and forms a 3M–5 dimensional surface called the potential energy surface (PES). The process of energy minimization to find the equilibrium bond lengths and bond angles of a molecule in a given electronic state is known as geometry optimization. The set of 3M–6 first partial derivatives of U form a vector $\{\partial U/\partial X_i\}$ called the gradient of the electronic energy. Any point on the PES where the gradient is zero is called a stationary point which may be a minimum, a maximum or a saddle point. The set of second derivatives $\partial^2 U/\partial X_1^2, \partial^2 U/\partial X_1 \partial X_2, \partial^2 U/\partial X_2 \partial X_1, \partial^2 U/\partial X_2^2, \ldots$ when arranged in an array form a matrix called the Hessian or force constant matrix. For a true minimum, all second derivatives must be positive. The procedure of geometry optimization starts with a guess for the equilibrium molecular geometry. The electronic energy and its gradient are calculated at the initial geometry using some quantum chemical method (HF, MP2, DFT, etc.). Based on the calculated values, the 3M–6 coordinates are changed to a new set for which U and $\{\partial U/\partial X_i\}$ are re-calculated. This iterative process is repeated until a convergence criterion is reached. The use of molecular symmetry helps in reduction of coordinates in the actual calculations [35].

The vibrational frequencies of the molecule are calculated by solving the set of 3M linear equations of the form,

$$\sum_{j=1}^{3M} \left(F_{ij} - \delta_{ij} \lambda_k \right) l_{jk} = 0, \quad i = 1, 2, \ldots, 3M \, , \tag{1.34}$$

where the set of quantities $F_{ij} = \left(\partial^2 U / \partial X_i \partial X_j \right)_e \Big/ \sqrt{m_i m_j}$ form the mass-weighted Hessian matrix, m_i is the mass of the nucleus corresponding to the nuclear coordinate X_i and the e in the subscript denotes that the quantity is calculated at the equilibrium geometry. The non-trivial solutions of the set of 3*M* homogeneous equations (1.34) are obtained by solving the secular (determinantal) equation of the form,

$$\left|F_{ij} - \delta_{ij}\lambda_k\right| = 0 \ . \tag{1.35}$$

Eq. (1.35) yields 3*N* roots λ_k and the vibrational mode frequencies are calculated from

$$\nu_k = \frac{\sqrt{\lambda_k}}{2\pi}, \qquad k = 1, 2, \ldots, 3M \ . \tag{1.36}$$

In the actual calculation, six of the λ_k values are found to be very close to zero, corresponding to the three translational and three rotational degrees of freedom of the molecule and the other values give the 3*M*–6 vibrational frequencies of the molecule. Once the values of λ_k are obtained, the set of 3*M*–6 equations (1.34) are solved for non-zero values of λ_k to yield the values of l_{jk}. The quantity $(m_i^{1/2} l_{jk}) / (m_j^{1/2} l_{ik})$ gives the ratio of the classical vibrational amplitudes X_j to X_i, for the *k*-th normal mode with frequency ν_k [35]. Theoretically calculated vibrational frequencies help in analyzing observed vibronic features in the photoabsorption spectra. Also in the geometry optimization processes, a set of real values of vibrational frequencies of a molecule calculated at the equilibrium geometry indicates that a true minimum of the electronic energy is reached. Excited states of the molecule are calculated keeping the geometry fixed to the ground state optimized values. From the Franck-Condon principle, it is expected that the observed maximum intensity of the electronic absorption occurs to an excited state vibrational level, which corresponds to no change in geometry from the ground state. Hence the excitation energy is called the vertical excitation energy.

1.4 ORGANIZATION OF THE THESIS

The thesis is organized into seven chapters including the introductory chapter. Chapters 2–4 describe the VUV photabsorption studies of the family of compounds known as dihalomethanes (CH_2X_2; X=I, Br, Cl) and their deuterated isotopologues. Chapter 5 is devoted to the VUV spectroscopy of DMSO (CH_3SOCH_3) and its deuterated analogue (CD_3SOCD_3). Photoabsorption studies relating to N_2O are discussed in Chapter 6.

In Chapter 2, a comprehensive investigation of the VUV absorption spectrum of diiodomethane (CH_2I_2) and diiodomethane-d_2 (CD_2I_2) in the region 30,000–95,000 cm^{-1} (3.7–11.8 eV) is presented. The spectrum of CH_2I_2 in the 50,000–66,666 cm^{-1} region and spectral analysis in the 50,000–85,000 cm^{-1} region are reported here for the first time. This is also the first report of the VUV photoabsorption spectrum of CD_2I_2, which serves to verify and consolidate the spectral assignments. It is observed that the absorption bands in the region 30,000–50,000 cm^{-1} are due to valence transitions, while the VUV spectrum in the range 50,000–95,000 cm^{-1} is dominated by several Rydberg series converging to the first four IPs of CH_2I_2 at 9.46, 9.76, 10.21 and 10.56 eV corresponding to removal of an electron from the outermost $3b_2$, $2b_1$, $1a_2$ and $4a_1$ non-bonding orbitals respectively. Vibronic features accompanying the Rydberg series are observed to be mainly due to excitation of the CI symmetric stretch (ν_3) and CH_2 wag (ν_8) modes, with smaller contributions from the CH symmetric stretch (ν_1). UV absorption bands are assigned to the low lying valence states and the unusually high underlying intensity in parts of the VUV spectrum is attributed to valence states with high oscillator strength.

In Chapter 3, a consolidated analysis of UV-VUV photoabsorption spectrum of dibromomethane (CH_2Br_2) and dibromomethane-d_2 (CD_2Br_2) in the energy region 35,000–95,000 cm^{-1} (4.3–11.8 eV) is presented. The transitions in the region 35,000–50,000 cm^{-1} are identified to be of valence nature and most in the region 50,000–95,000 cm^{-1} are assigned to Rydberg series of *ns*, *np* and *nd* type converging to the first four ionization limits at 10.52, 10.74, 11.21 and 11.30 eV corresponding to excitations from the outermost orbitals $3b_2$, $2b_1$, $1a_2$, $4a_1$ of CH_2Br_2. The 5p and 4d Rydberg states are observed to be associated with vibrational structures which are assigned exclusively to the totally symmetric (a_1) CBr symmetric stretching mode (ν_3) in contrast to the earlier assignment to ν_3 and CH_2 bending (ν_2) modes. The valence transitions responsible for the broad intensity pedestals underlying the Rydberg transitions are inferred. The assignments are confirmed using isotopic substitution studies on CD_2Br_2 whose UV-VUV photoabsorption spectrum is reported here for the first time.

Chapter 4 is devoted to the photoabsorption spectroscopy of dichloromethane (CH_2Cl_2) and dichloromethane-d_2 (CD_2Cl_2) in the energy region 50,000–95,000 cm^{-1} (6.2–11.8 eV). The observed absorption band of CH_2Cl_2 in the region 50,000–60,000 cm^{-1} is identified to be of valence nature and most of the bands in the region 60,000–95,000 cm^{-1} are fitted to Rydberg series of *ns*, *np* and *nd* type converging to the first four ionization potentials 11.320, 11.357, 12.152 and 12.271 eV of CH_2Cl_2 arising from excitation of an electron from one of the four outermost Cl non-bonding orbitals. Observed vibronic features associated with a few Rydberg states are assigned mainly to the CCl_2 symmetric stretch (ν_3) mode with smaller contributions from the CH_2 symmetric stretch (ν_1), CH_2 bend (ν_2) and CH_2 wag (ν_8) modes. The assignments are corroborated by comparison with the absorption spectrum of the deuterated isotopologue CD_2Cl_2.

Chapter 5 deals with the VUV spectroscopy of dimethyl sulphoxide (DMSO) and its deuterated analogue (DMSO-d_6) in the energy region 35,000–80,000 cm^{-1} using the Photophysics beamline. The overall spectral features observed for DMSO are in good agreement with earlier work, while the VUV photoabsorption spectrum of DMSO-d_6 has been reported here for the first time. It is observed that the vibronic structures which appear in the absorption spectrum of DMSO are not very prominent in DMSO-d_6, in fact some of them seem to disappear. This aspect is further investigated by recording the photoabsorption spectra of DMSO and DMSO-d_6 at a better resolution (~0.5 Å) using the HRVUV beamline. This spectrum however exhibits several new features arising due to the VUV dissociation of the molecules. Details of these studies together with theoretical calculations are presented in this chapter.

In Chapter 6, a reinvestigation of the absorption spectrum of nitrous oxide (N_2O) in the region 72,000–95,000 cm^{-1} region is carried out and Rydberg series and vibronic assignments are discussed. The observed spectrum comprises mainly of Rydberg series converging to the two spin-orbit components ($^2\Pi_{1/2,3/2}$) of the ground state of N_2O^+ and a few high lying valence transitions. The $3p\pi\,^1\Sigma^+$ state at ~77,600 cm^{-1} shows large quantum defect (0.96) which is explained as arising due to mixed valence-Rydberg character. In the 85,000–95,000 cm^{-1} region, a number of absorption features are observed with greater clarity than in earlier photoabsorption studies and assigned to Rydberg series of type $nl\lambda$ (n=3,4; l=s,p,d; $\lambda=\sigma,\pi,\delta$) and accompanying vibronic bands. This work has resulted in clarification of several discrepancies in earlier Rydberg series assignments. Additionally, the $3p\pi\ ^3\Sigma^-$ Rydberg state at 85,788 cm^{-1}, the valence transition $7\sigma\rightarrow3\pi$ ($^1\Pi$) at 87,433 cm^{-1} and the $3d\lambda$ Rydberg series in the 91,700–92,600 cm^{-1} region are assigned for the first time.

Finally in the last chapter, the important conclusions from the present studies are summarized and scope for future work is discussed.

CHAPTER 2

ELECTRONIC SPECTROSCOPY OF DIIODOMETHANE AND DIIODOMETHANE-d_2

2.1 INTRODUCTION

Reactive halogen atoms and radicals play an important role in tropospheric chemistry. The principal sources of halogen atoms in the troposphere are organic halogen containing compounds which may be of natural or anthropogenic origin; one of the major natural sources being the oceans [38]. Recent studies show that in addition to the earlier established role of the methyl halides as source gases, dihalomethanes also contribute significantly to the production of halogen atoms [38]. Diiodomethane (CH_2I_2) has now been recognized as a molecule of significant atmospheric interest [39]. The photolysis of iodine containing compounds like CH_3I and CH_2I_2 in the presence of ozone results in formation of iodine oxide (IO), which in turn contributes to formation of aerosols, especially in coastal areas [39].

Although the electronic spectra and dynamics of halomethanes have attracted the interest of researchers since a long time with a considerable amount of work published on monoalkyl halides, relatively few studies have been reported on the dihalomethanes. One of the reasons for this could be the presence of two carbon-halogen bonds in these molecules which makes their electronic structure and spectra more complex [40]. Early spectroscopic studies of molecules containing two or more halogen atoms have noted that the observed interaction amongst the lone pairs and local σ* configurations are stronger in the dibromides and diiodides than in the corresponding dichlorides and difluorides [14]. In addition to its atmospheric importance, CH_2I_2 being a small molecule is also considered as a prototype for examining photodissociation dynamics of two-chromophore systems [41]. Yet another reason for the interest in CH_2I_2 is related to the potential for lasing action in excited I_2 produced by photodissociation of CH_2I_2 [42].

Over the years, a considerable number of experimental [14, 38, 40-58] and theoretical [59-63] investigations on CH_2I_2, largely pertaining to photodissociation dynamics in the UV region (<50,000 cm^{-1}) have been carried out. Notwithstanding the vast amount of literature available on the UV region, it is rather surprising that there is very little information available on the vacuum ultraviolet (VUV) spectrum of CH_2I_2. The only published work on the VUV photoabsorption spectrum of CH_2I_2 is by Okabe *et al.* [42] who reported absorption cross sections in the region 1100–1500 Å (66,666–90,910 cm^{-1}) measured using a hydrogen discharge lamp. Their investigation focused on photodissociation aspects and except for a tentative assignment of one *ns* Rydberg series, no spectral assignments were made by them. This very limited VUV spectral data and the absence of assignments reported in literature for the higher excited states of CH_2I_2 motivated the present work. The electronic absorption spectrum of diiodomethane in the region 30,000–95,000 cm^{-1} (3.7–11.8 eV) is investigated using synchrotron radiation. Spectral analysis is aided by DFT calculations of vibrational frequencies and TDDFT calculations of excited state energies and potential energy curves. This is the first report of the VUV spectrum of CH_2I_2 in the region 50,000–66,666 cm^{-1} and the first spectral analysis of the entire VUV region of 50,000–85,000 cm^{-1}. Spectral assignments are confirmed by comparison with the spectrum of the deuterated isotopologue diiodomethane-d_2 (CD_2I_2) whose VUV spectrum is also reported for the first time.

2.2 METHODOLOGY

2.2.1 EXPERIMENTAL

The Photophysics beamline and gas phase experimental station described in Chapter 1 is used for these studies. The sample which is in liquid form at room temperature is contained in a glass vial connected to the absorption cell by a glass-metal seal and several Swagelok valves. The CH_2I_2 and CD_2I_2 samples (Sigma Aldrich) with stated purity of 99% are subjected to several freeze-pump-thaw cycles to get rid of volatile impurities before introduction into the cell. The sample pressure is varied from 0.001 to 1 mbar in this study. In general, cross sections are much higher in the VUV region, for which a pressure of ~0.01 mbar is found to be optimum. In the UV region where absorption cross sections are relatively lower, sample pressure of ~1 mbar is used to obtain clear absorption features. Details of the experimental setup have been described in Chapter 1.

2.2.2 COMPUTATIONAL

The ground state of CH_2I_2 belongs to C_{2V} point group and the geometry used for calculations is such that the origin is at the center of mass of the molecule, the I–C–I group is in the YZ plane and the H–C–H group lies in the XZ plane. It may be noted here that for molecules belonging to C_{2V} point group, the choice of vertical planes XZ and YZ determines the b_1 and b_2 symmetries. This must be taken into account while comparing the results of different calculations. Geometry optimization and vibrational frequency calculations of the neutral and cationic ground states of CH_2I_2 are performed using density functional theory (DFT) with two hybrid exchange correlation GGA functionals *viz.* Perdew-Burke-Ernzerhof (PBE0) [64] and Becke-3-Lee-Yang-Parr (B3LYP) [25, 65] as well as the second order Møller-Plesset perturbation theory (MP2). Calculations for the cationic ground states of

CH_2I_2 and CD_2I_2 are computed using the unrestricted reference (UHF). Computational studies of the excited state electronic structure of CH_2I_2 are carried out using the time dependent density functional theory (TDDFT). For calculation of vertical excited states, the geometrical parameters of the molecule are held fixed to the optimized ground state values.

Basis sets used in the present study include the correlation consistent basis sets cc-pVnZ and aug-cc-pVnZ [36]. The latter are augmented with diffuse functions for carbon and hydrogen. For iodine, cc-pVnZ-PP and aug-cc-pVnZ-PP (n = T, Q, 5) basis sets [66, 67], obtained from the EMSL basis set library [68, 69] are used. These basis sets replace the iodine inner cores (1s–3d) by energy-consistent relativistic pseudopotentials optimized in multi-configurational Dirac-Hartree-Fock calculations and have demonstrated systematic convergence in both Hartree-Fock and correlation energies [66, 67].

2.3 RESULTS AND DISCUSSION

2.3.1 GROUND STATE MOLECULAR ORBITALS, EQUILIBRIUM GEOMETRIES AND VIBRATIONAL FREQUENCIES

The ground state electronic configuration of CH_2I_2 as predicted by the DFT computation is $[\mathit{core}](1a_1)^2(1b_2)^2(2a_1)^2(1b_1)^2(3a_1)^2(2b_2)^2(4a_1)^2(1a_2)^2(2b_1)^2(3b_2)^2$: X^1A_1 where the numbering excludes core electrons. While some of the earlier workers [70] have suggested the orbital ordering of the four highest occupied molecular orbitals (HOMOs) to be $4a_12b_11a_23b_2$, the present ordering agrees with the extended Hückel calculation of Manne *et al.* [71] and the work by Dixon *et al.* [72] in which halogen-halogen as well as halogen-carbon interaction have been taken into account. Contour plots of the four HOMOs ($4a_1$, $1a_2$, $2b_1$, $3b_2$) and four lowest unoccupied molecular orbitals or LUMOs ($5a_1$, $3b_1$, $6a_1$, $4b_2$) of CH_2I_2 generated using the software MacMolPlt [20] are shown in Fig. 2.1.

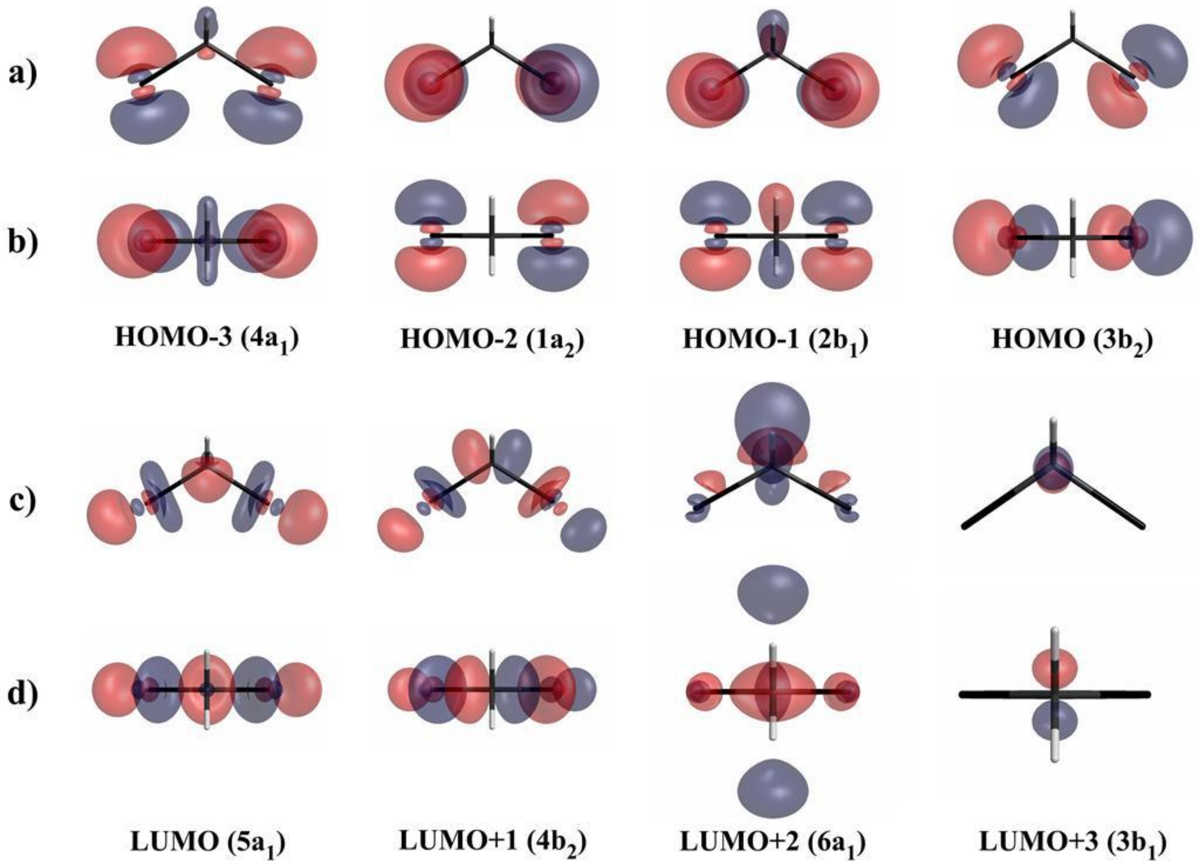

Fig. 2.1: Contour plots of the four HOMOs and four LUMOs of CH_2I_2 at PBE0/aug-cc-pVQZ level of theory. HOMOs viewed along (a) X axis and (b) Z axis, LUMOs viewed along (c) X axis and (d) Z axis

It is observed that the four outermost occupied orbitals have a predominantly non-bonding character. Of these, the $3b_2$ and $1a_2$ orbitals correspond to iodine lone pair orbitals while the $2b_1$ and $4a_1$ orbitals are iodine lone pair type mixed with weaker C–H bonding contributions. The two LUMOs ($5a_1$ and $4b_2$) exhibit C–I antibonding character, while the $6a_1$ and $3b_1$ LUMOs are of non-bonding nature localized on the carbon atom. The energy level diagram corresponding to these orbitals is shown in Fig. 2.2, with a few electronic transitions marked. Correlation of theoretically predicted transitions and experimental observations is discussed in Section 2.3.2.

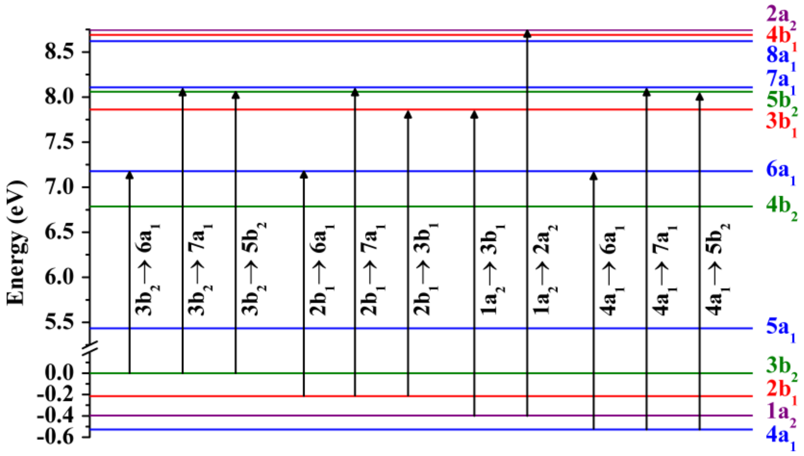

Fig. 2.2: Energy level diagram showing first few Rydberg transitions. The zero of the energy scale is fixed at the energy of the HOMO ($3b_2$).

The results of geometry optimization of the ground states of the neutral and ionic CH_2I_2, using DFT and MP2 methods with the aug-cc-pVQZ basis set are shown in Tables 2.1 and 2.2 respectively. The calculated bond lengths and bond angles of CH_2I_2 are compared with the experimentally measured values [73] while experimental geometry parameters for $CH_2I_2^+$ are not available in literature. The MP2 method is found to yield the best agreement with the experimental values and in DFT, PBE0 is found to yield better agreement than B3LYP. As TDDFT method is used for computations of vertical excited states, the optimized geometry obtained from PBE0/aug-cc-pVQZ calculations is considered for further calculations.

Table 2.1: Optimized bond lengths (Å) and bond angles (deg.) of the ground state of CH_2I_2 using DFT and MP2 methods

	r(C–I)	r(C–H)	∠(I–C–I)	∠(H–C–I)	∠(H–C–H)
B3LYP/aug-cc-pVQZ	2.154	1.079	116.6	107.0	112.3
PBE0/aug-cc-pVQZ	2.127	1.082	116.1	107.2	111.9
MP2/aug-cc-pVQZ	2.128	1.082	114.6	107.7	111.6
Experimental[a]	2.12	1.09	114.7	–	111.3

[a]Ref. [73]

Table 2.2: Optimized bond lengths (Å) and bond angles (deg.) of the ground state of $CH_2I_2^+$ using DFT and MP2 methods

	r(C–I)	r(C–H)	∠(I–C–I)	∠(H–C–I)	∠(H–C–H)
B3LYP/aug-cc-pVQZ	2.147	1.082	95.7	110.9	115.8
PBE0/aug-cc-pVQZ	2.121	1.084	93.9	111.3	115.8
MP2/aug-cc-pVQZ	2.123	1.083	93.3	111.3	116.0

The calculated vibrational frequencies of the ground states of CH_2I_2/$CH_2I_2^+$ and CD_2I_2/$CD_2I_2^+$ at the PBE0/aug-cc-pVQZ level of theory are listed in Table 2.3. Corresponding experimental values are given alongside wherever available from literature [39, 74]. A close agreement is seen between the theoretically predicted and experimentally reported vibrational frequencies of neutral species. It may be noted that experimental values of vibrational frequencies for the $CH_2I_2^+$ and $CD_2I_2^+$ are not available in literature, only computed values of frequencies have been reported earlier for $CH_2I_2^+$ (*cf.* Table 2.2) [56].

Table 2.3: Ground state vibrational frequencies (cm^{-1}) of CH_2I_2 and $CH_2I_2^+$ calculated at the PBE0/aug-cc-pVQZ level of theory

Normal Mode (symmetry)	**CH_2I_2**		**CD_2I_2**		**$CH_2I_2^+$**		**$CD_2I_2^+$**
	This work	**Expt.**[a]	**This work**	**Expt.**[b]	**This Work**	**B3LYP/ 6-311G***[c]	**This work**
ν_1: C-H_2 sym. stretch (a_1)	3156	3002	2286	2191^L	3139	3142	2271
ν_2: C-H_2 bend (a_1)	1412	1374	1036	999^L	1390	1411	1021
ν_3: C-I_2 sym. str. (a_1)	507	493	481	456^L	585	540	555
ν_4: C-I_2 bend (a_1)	123	122^L	122	122^L	133	113	132
ν_5: C-H_2 twist (a_2)	1070	1042	758	733^L	1017	1011	721
ν_6: C-H_2 asym. stretch (b_1)	3246	3073	2415	2344	3254	3257	2426
ν_7: C-H_2 rock (b_1)	738	718	578	554	774	789	589
ν_8: C-H_2 wag (b_2)	1143	1114	864	842	1132	1127	859
ν_9: C-I_2 asym. stretch (b_2)	611	584	576	547	533	500	502

[a]Ref. [39], [b]Ref. [74], [c]Ref. [56], [L]denotes frequencies in liquid

2.3.2 EXPERIMENTALLY OBSERVED RYDBERG SERIES AND CORRELATION WITH COMPUTED VERTICAL EXCITED STATES

The experimentally measured photoabsorption spectra of CH_2I_2 and CD_2I_2 in the VUV region are shown in Fig. 2.3. The first four IPs of CH_2I_2 arising from electron excitation from the four outermost non-bonding orbitals have been measured at 9.46, 9.76, 10.21 and 10.56 eV by photoelectron spectroscopy studies [70]. Several Rydberg series of type *ns*, *np* and *nd* converging to each of these four IPs are observed in the present study. Identification of these series in the experimental spectrum is done on the basis of quantum defect analysis, using the well known Rydberg expression (Eq.1.5). Since the electron excitation is from the iodine lone pair orbitals, one expects the quantum defect values to be close to the iodine atomic quantum defects [75]. Following this line of reasoning, most of the observed spectral features in the VUV region can be assigned to Rydberg series with iodine-like quantum defects as listed in Tables 2.4–7 and marked appropriately in Fig. 2.3.

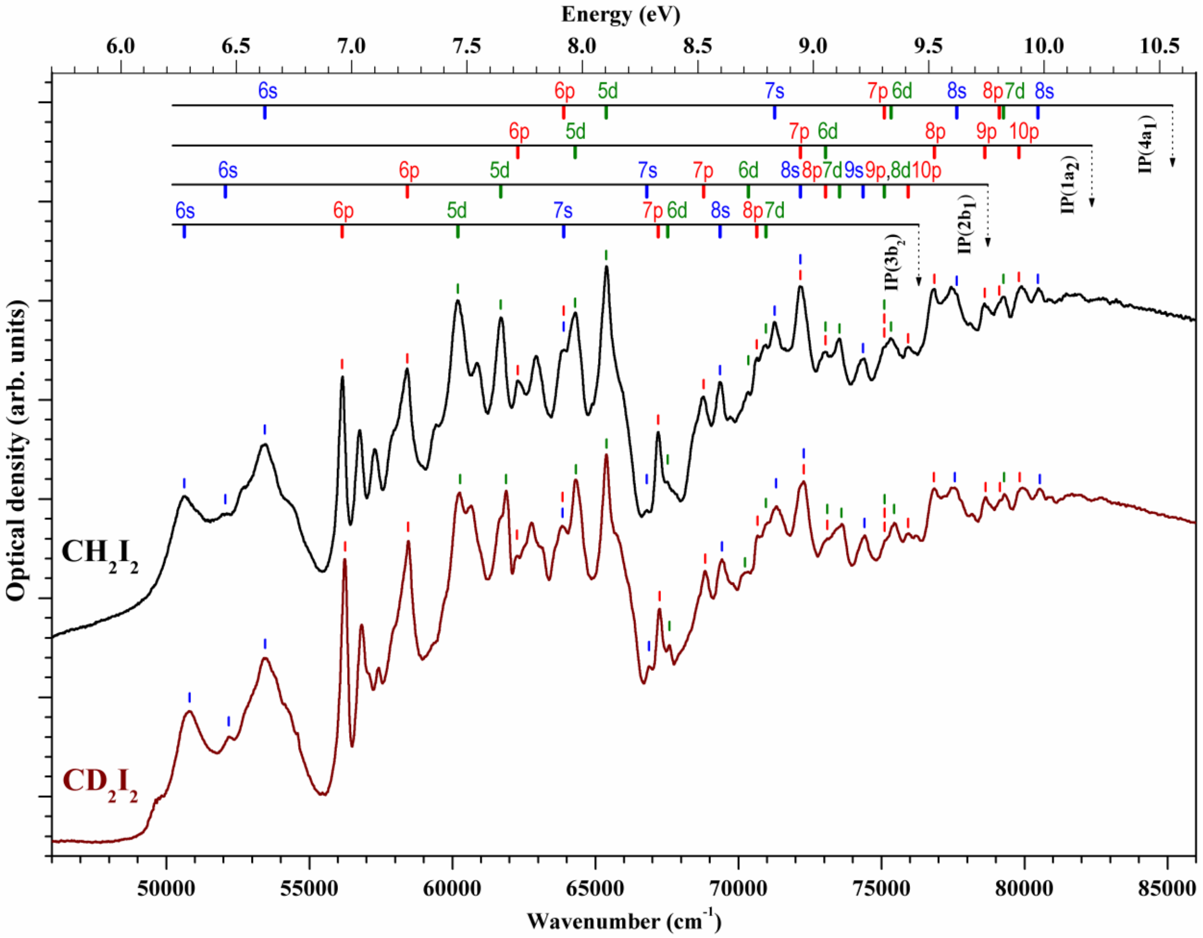

Fig. 2.3: Rydberg series observed in the VUV photoabsorption spectra of CH_2I_2 and CD_2I_2

For each of the four IPs, three to five members of *ns*, *np* and *nd* series are observed, except for $1a_2$→*ns* which is dipole forbidden. The most extensive series appears to be the *np* series with five members each observed for $3b_2$→*np* and $1a_2$→*np*. Experimentally observed quantum defects are in the range 3.93–4.19 for the *ns* series, 3.53–3.74 for the *np* series and 2.38–2.70 for the *nd* series. It may be noted that a few of the features in the region 1200–1350 Å have been tentatively assigned to *ns* type Rydberg series converging to the IP at

10.21 eV by Okabe *et al*. [42]. A quantum defect of 4.25 was assumed by them. However, the assignment of this series to *ns* is doubtful as the corresponding orbital excitation is from 1a_2 to *ns* (a_1), which is dipole forbidden under the C_{2v} point group.

Note here that the vertical excited state energies do not change with isotopic substitution; hence theoretical results in Tables 2.4–2.7 are tabulated only for CH_2I_2. The observed isotopic shifts between Rydberg series origins of CH_2I_2 and CD_2I_2 depend mainly on the difference in zero point energies (ZPE) between the ground and excited states of each isotopic species (*cf.* Chapter 1). Since the exact calculation of vibrational frequencies for the excited states is not possible, the ionic ground state frequencies (*cf.* Table 2.3) are taken to be indicatives of the excited state frequencies of the neutral molecule. Following this, the difference in ZPE between excited states and ground state is ~1440 cm^{-1} for both isotopic species, *i.e.*, expected isotopic shift of ≈0. The experimentally observed isotope shift (*cf.* Tables 2.4–2.7) varies from ~ –190 to +120 cm^{-1} (–24 to 15 meV), which may mean that the actual excited state frequencies are somewhat different from the calculated ionic frequencies.

Table 2.4: Rydberg series converging to IP ($3b_2$) = 9.46 eV observed in VUV photoabsorption spectrum of diiodomethane

Experimentally observed peak position[a]			**Calculated by TDDFT: PBE0/aug-cc-pVQZ**					**O–C**
Assignment	**CH_2I_2**	**CD_2I_2**	**Energy (eV)**	***f***	**Major transition**	***A***	**Λ**	
6s	6.277 (3.93)	6.300 (3.93)	6.320	0.181	$3b_2 \rightarrow 6a_1$	0.80	0.39	-0.043
7s	7.921 (4.03)*	7.917 (4.03)*	7.651	0.007	$3b_2 \rightarrow 8a_1$	-0.76	0.38	0.270
8s	8.600 (4.02)	8.608 (4.00)	8.602	0.027	$3b_2 \rightarrow 10a_1$	-0.55	0.34	-0.002
6p	6.962 (3.67)	6.974 (3.66)	7.207	0.008	$3b_2 \rightarrow 7a_1$	0.98	0.26	-0.245
			7.945	0.013	$3b_2 \rightarrow 2a_2$	0.91	0.20	-0.982
7p	8.331 (3.53)	8.337 (3.52)	7.998	0.016	$3b_2 \rightarrow 9a_1$	-0.89	0.27	0.333
			9.100	0.046	$3b_2 \rightarrow 3a_2$	-0.77	0.39	-0.769
8p	8.758 (3.60)	8.762 (3.58)	8.763	<0.001	$3b_2 \rightarrow 11a_1$	0.89	0.26	-0.005
			10.964	0.216	$3b_2 \rightarrow 4a_2$	-0.60	0.36	-2.207
5d	7.463 (2.39)	7.473 (2.38)	7.277	0.012	$3b_2 \rightarrow 5b_2$	0.71	0.32	0.186
6d	8.372 (2.46)	8.380 (2.45)	7.983	0.038	$3b_2 \rightarrow 6b_2$	-0.87	0.28	0.389
7d	8.798 (2.47)	8.798 (2.47)	8.329	0.060	$3b_2 \rightarrow 7b_2$	-0.51	0.42†	0.469

[a] quantum defect value in the parenthesis, *blended line, *f*: oscillator strength, *A*: excitation amplitude, Λ: lambda diagnostic, †valence-Rydberg mixed nature, O–C: difference of observed and calculated energies (eV)

Table 2.5: Rydberg series converging to IP ($2b_1$) = 9.76 eV observed in VUV photoabsorption spectrum of diiodomethane

Experimentally observed peak position[a]			**Calculated by TDDFT: PBE0/aug-cc-pVQZ**					**O–C**
Assignment	**CH_2I_2**	**CD_2I_2**	**Energy (eV)**	***f***	**Major transition**	***A***	**Λ**	
6s	6.455 (3.97)	6.470 (3.97)	6.450	0.097	$2b_1 \rightarrow 6a_1$	-0.97	0.36	0.005
7s	8.282 (3.97)	8.292 (3.96)	7.908	0.059	$2b_1 \rightarrow 8a_1$	-0.87	0.35	0.374
8s	8.948 (3.91)*	8.962 (3.87)*	8.603	0.002	$2b_1 \rightarrow 10a_1$	-0.92	0.28	0.345
9s	9.219 (3.98)	9.225 (3.96)	10.035	0.016	$2b_1 \rightarrow 12a_1$	-0.95	0.45†	-0.816
6p	7.244 (3.67)	7.247 (3.67)	7.414	0.040	$2b_1 \rightarrow 7a_1$	0.95	0.26	-0.170
			8.145	0.033	$2b_1 \rightarrow 2a_2$	-0.82	0.30	-0.902
7p	8.528 (3.68)	8.534 (3.67)	8.190	0.002	$2b_1 \rightarrow 9a_1$	-0.90	0.26	0.338
			9.193	0.102	$2b_1 \rightarrow 3a_2$	0.67	0.53†	-0.665
8p	9.056 (3.61)*	9.064 (3.58)*	8.940	0.006	$2b_1 \rightarrow 11a_1$	-0.78	0.32	0.116
9p	9.311 (3.50)*	9.313 (3.48)*	10.453	0.003	$2b_1 \rightarrow 13a_1$	0.68	0.44†	-1.142
10p	9.415 (3.72)	9.415 (3.72)	11.678	0.009	$2b_1 \rightarrow 15a_1$	0.86	0.36	-2.263
5d	7.649 (2.46)	7.672 (2.45)	7.205	0.016	$2b_1 \rightarrow 3b_1$	-0.74	0.31	0.444
6d	8.722 (2.38)	8.707 (2.40)	8.032	0.022	$2b_1 \rightarrow 4b_1$	-0.85	0.34	0.690
7d	9.117 (2.40)	9.125 (2.37)	8.745	<0.001	$2b_1 \rightarrow 5b_1$	-0.83	0.52†	0.372
8d	9.311 (2.50)*	9.313 (2.48)*	9.145	0.006	$2b_1 \rightarrow 6b_1$	0.79	0.31	0.166
9d	–	–	10.242	<0.001	$2b_1 \rightarrow 7b_1$	-0.65	0.50†	–

[a] quantum defect value in the parenthesis, *blended line, *f*: oscillator strength, *A*: excitation amplitude, Λ: lambda diagnostic, †valence-Rydberg mixed nature, O–C: difference of observed and calculated energies (eV)

Table 2.6: Rydberg series converging to IP ($1a_2$) = 10.21 eV observed in VUV photoabsorption spectrum of diiodomethane

Experimentally observed peak position[a]			**Calculated by TDDFT: PBE0/aug-cc-pVQZ**					**O–C**
Assignment	**CH_2I_2**	**CD_2I_2**	**Energy (eV)**	***f***	**Major transition**	***A***	**Λ**	
6s	–	–	6.606	0.000	$1a_2 \rightarrow 6a_1$	0.97	0.32	–
7s	–	–	8.066	0.000	$1a_2 \rightarrow 8a_1$	0.89	0.32	–
8s	–	–	8.773	0.000	$1a_2 \rightarrow 10a_1$	0.94	0.27	–
6p	7.722 (3.66)	7.720 (3.66)	7.405	0.054	$1a_2 \rightarrow 3b_1$	-0.95	0.25	0.317
			7.567	0.015	$1a_2 \rightarrow 5b_2$	0.86	0.33	0.155
7p	8.948 (3.72)*	8.962 (3.70)*	8.253	<0.001	$1a_2 \rightarrow 4b_1$	0.67	0.32	0.695
			8.315	0.023	$1a_2 \rightarrow 6b_2$	-0.81	0.25	0.633
8p	9.527 (3.54)	9.527 (3.54)	8.979	0.171	$1a_2 \rightarrow 5b_1$	-0.80	0.50†	0.548
			8.793	0.041	$1a_2 \rightarrow 7b_2$	-0.93	0.30	0.734
9p	9.747 (3.58)	9.749 (3.57)	9.363	<0.001	$1a_2 \rightarrow 6b_1$	0.97	0.24	0.384
			9.614	0.208	$1a_2 \rightarrow 8b_2$	-0.93	0.38	0.132
10p	9.895 (3.43)	9.898 (3.40)	10.481	0.023	$1a_2 \rightarrow 7b_1$	-0.78	0.44†	-0.586
5d	7.971 (2.54)	7.974 (2.53)	8.407	0.011	$1a_2 \rightarrow 2a_2$	0.79	0.32	-0.437
6d	9.056 (2.57)*	9.064 (2.55)*	9.434	0.027	$1a_2 \rightarrow 3a_2$	-0.63	0.52†	-0.378
7d	–	–	11.504	0.039	$1a_2 \rightarrow 4a_2$	0.56	0.43†	

[a] quantum defect value in the parenthesis, *blended line, *f*: oscillator strength, *A*: excitation amplitude, Λ: lambda diagnostic, †valence-Rydberg mixed nature, O–C: difference of observed and calculated energies (eV)

Table 2.7: Rydberg series converging to IP ($4a_1$) = 10.56 eV observed in VUV photoabsorption spectrum of diiodomethane

Experimentally observed peak position[a]			**Calculated by TDDFT: PBE0/aug-cc-pVQZ**					**O–C**
Assignment	**CH_2I_2**	**CD_2I_2**	**Energy (eV)**	***f***	**Major transition**	***A***	**Λ**	
6s	6.625 (4.14)	6.627 (4.14)	6.740	0.058	$4a_1 \rightarrow 6a_1$	-0.95	0.34	-0.115
7s	8.836 (4.19)	8.843 (4.19)	8.189	0.019	$4a_1 \rightarrow 8a_1$	-0.79	0.36	0.647
8s	9.625 (4.19)	9.616 (4.20)	8.981	0.059	$4a_1 \rightarrow 10a_1$	-0.90	0.39	0.644
9s	9.977 (4.17)	9.985 (4.13)	10.399	0.001	$4a_1 \rightarrow 12a_1$	-0.75	0.50†	-0.422
6p	7.921 (3.73)*	7.917 (3.73)*	7.716	0.015	$4a_1 \rightarrow 7a_1$	-0.87	0.32	0.205
			7.524	0.014	$4a_1 \rightarrow 3b_1$	-0.88	0.20	0.398
7p	9.311 (3.70)*	9.313 (3.70)*	8.567	<0.001	$4a_1 \rightarrow 9a_1$	0.87	0.29	0.744
			8.366	0.050	$4a_1 \rightarrow 4b_1$	0.83	0.27	0.944
8p	9.809 (3.74)	9.812 (3.73)	9.269	0.006	$4a_1 \rightarrow 11a_1$	-0.87	0.33	0.540
			8.964	0.004	$4a_1 \rightarrow 5b_1$	0.60	0.36	0.845
9p	–	–	9.483	0.001	$4a_1 \rightarrow 6b_1$	-0.98	0.18	–
5d	8.106 (2.65)	8.107 (2.65)	7.728	0.001	$4a_1 \rightarrow 5b_2$	0.76	0.34	0.379
6d	9.340 (2.66)	9.353 (2.64)	8.377	0.186	$4a_1 \rightarrow 6b_2$	0.62	0.32	0.963
7d	9.828 (2.69)	9.831 (2.68)	8.894	0.010	$4a_1 \rightarrow 7b_2$	0.94	0.32	0.934
8d	–	–	9.713	0.002	$4a_1 \rightarrow 8b_2$	0.93	0.32	–

[a] quantum defect value in the parenthesis, *blended line, *f*: oscillator strength, *A*: excitation amplitude, Λ: lambda diagnostic, †valence-Rydberg mixed nature, O–C: difference of observed and calculated energies (eV)

Theoretically predicted transitions corresponding to the observed Rydberg series are tabulated to the right side of the experimental values in Tables 2.4–2.7. Vertical excited states of CH_2I_2 are generated at the equilibrium geometry of the neutral ground state using PBE0/aug-cc-pVQZ. Excitation amplitudes for the major orbital excitations (amplitude >0.5) contributing to each transition, oscillator strengths and lambda diagnostic values are also tabulated. The assignment of calculated electronic states to experimentally observed Rydberg (and valence) transitions is carried out essentially based on the symmetries of initial and final MOs involved in the transition. As stated in Chapter 1, the accuracy of calculated excited state energies is expected to be very good up to 1 eV higher than the energy of the HOMO [31], *i.e.*, ~8.38 eV in this case. Except for a few low lying transitions, higher excited states are quite severely overlapped and it is not straightforward to correlate the intensities observed in the experimental spectra with calculated oscillator strengths. For example, in the 7p and 9p region, there are a lot of underlying intensity that could be due to overlapping valence states.

For the *ns* series, the final MOs are of a_1 symmetry. For the *np* and *nd* series, although such a generalization cannot be made, the symmetries of the final orbitals are expected to be the same within a given series that converges to a specified IP. Using this logic, all experimentally observed transitions are correlated with theoretically calculated energies. It is observed that low lying excited states result from essentially single orbital excitations, whereas for higher excited states mixing of two or more molecular orbital excitations with comparable amplitude becomes more common.

For *np* series, two sets of theoretically predicted excited states corresponding to different symmetries can be associated with the experimentally observed peaks. Both the possibilities are listed in Tables 2.4–7. While it is permissible, in principle to observe more than one series of a given angular momentum, it may not be possible to distinguish these in the spectrum due to the presence of several intense valence transitions overlapping the Rydberg transitions, as discussed in Section 2.3.4 on valence excited states. The experimental resolution may also play a role here and for a more thorough understanding it would be useful to carry out photoabsorption studies at higher resolution.

2.3.3 VIBRONIC ASSIGNMENTS

Vibronic features accompanying the Rydberg series are observed for the $2b_1\rightarrow6s$, $3b_2\rightarrow6p$, $2b_1\rightarrow6p$ and $2b_1\rightarrow5d$ transitions. Assignment of the vibronic features is accomplished by comparison of the intervals between vibronic bands with the calculated ionic frequencies of CH_2I_2. The assignments are further validated by comparing the corresponding vibronic band positions in the deuterated analogue CD_2I_2. The consolidated list of vibronic assignments is displayed in Table 2.8 and an expanded view of the VUV photoabsorption spectrum of CH_2I_2 in the region 52,000–63,000 cm^{-1} with vibronic features marked appropriately is shown in Fig. 2.4.

Table 2.8: Vibronic bands (cm^{-1}) observed in the VUV photoabsorption spectra of diiodomethane.

Assignment	CH_2I_2		CD_2I_2	
	Peak Position	ΔE	Peak Position	ΔE
$2b_1 \rightarrow 6s$	**52,064**		**52,186**	
$2b_1 \rightarrow 6s+\nu_3'$	52,643	579	52,803	617
$3b_2 \rightarrow 6p$	**56,150**		**56,247**	
$3b_2 \rightarrow 6p+\nu_3'$	56,761	611	56,841	594
$3b_2 \rightarrow 6p+\nu_8'$	57,286	1136	57,071	824
$3b_2 \rightarrow 6p+2\nu_3'$	57,286	1136	57,435	1188
$3b_2 \rightarrow 6p+3\nu_3'$	57,961	1811	57,995	1748
$2b_1 \rightarrow 6p$	**58,423**		**58,450**	
$2b_1 \rightarrow 6p+\nu_8'$	59,431	1008	59,342	892
$2b_1 \rightarrow 6p+\nu_2+\nu_8'$	60,867	2444	60,270	1820
$2b_1 \rightarrow 6p+\nu_1'$	61,693	3270	60,653	2203
$2b_1 \rightarrow 5d$	**61,693**		**61,879**	
$2b_1 \rightarrow 5d+\nu_8'$	62,916	1223	62,779	900

ΔE is the difference in energy between the Rydberg series origin and the associated vibronic band.

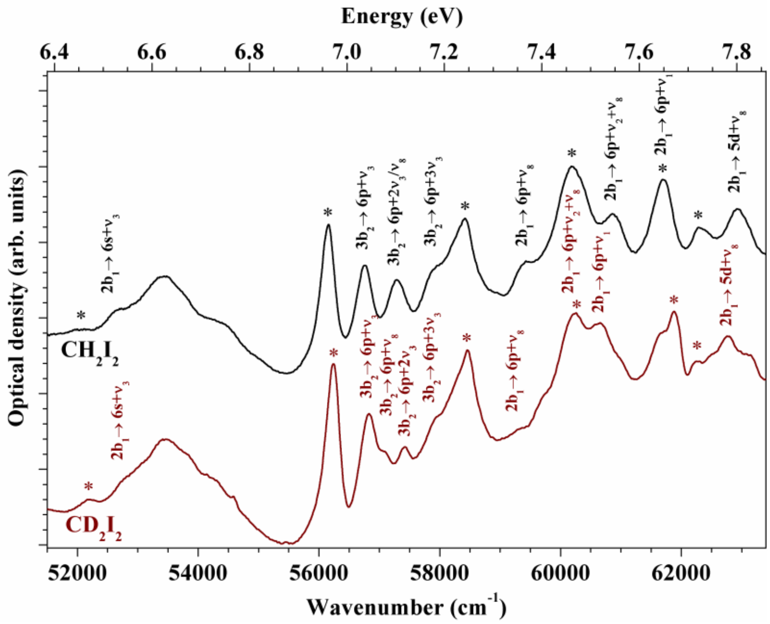

Fig. 2.4: Vibronic assignments in the spectra of CH_2I_2 and CD_2I_2 in 52,000–63,000 cm^{-1} region. Rydberg series origins are indicated by (*)

The $2b_1 \rightarrow 6s$ Rydberg transition is accompanied by excitation of one quantum of the ν_3' mode (C–I symmetric stretch) while the $3b_2 \rightarrow 6p$ transition shows a very well formed progression of ν_3' up to three members as well as excitation of one quantum of the ν_8' mode (CH_2 wag). Here primes denote the vibrational frequencies of the upper electronic state. It is interesting to note that the $3b_2 \rightarrow 6p+\nu_8'$ feature (located at 1136 cm^{-1} from the origin) is blended with $3b_2 \rightarrow 6p+2\nu_3'$ at 57,286 cm^{-1} in CH_2I_2, whereas in CD_2I_2 the ν_8' and $2\nu_3'$ features (located at 824 and 1188 cm^{-1} from the origin) occur at 57,071 and 57,435 cm^{-1} respectively and are clearly distinguishable. Thus the unambiguous identification of the ν_8' mode is rendered possible due to the isotopic comparison study. Vibronic features accompanying the $2b_1 \rightarrow 6p$ transition are assigned to ν_8', ν_1' and the combination band $\nu_8'+\nu_2'$. The feature appearing at 62,916 cm^{-1} in CH_2I_2, red shifted to 62,779 cm^{-1} in CD_2I_2 can be similarly be assigned to $2b_2 \rightarrow 5d+\nu_8'$.

2.3.4 VALENCE EXCITED STATES

The first few excited states of CH_2I_2 are valence in nature and occur in the UV region (30,000–50,000 cm^{-1}) while a few valence states and Rydberg-valence mixed states are also predicted by the current calculations in higher energy regions (>50,000 cm^{-1}). Although the photoabsorption spectrum of CH_2I_2 in the UV (*cf*. Fig. 2.5) has been discussed extensively by several authors [43, 44, 48, 49, 51, 76], there still remain several unresolved discrepancies in the assignments of electronic transitions to the observed spectrum.

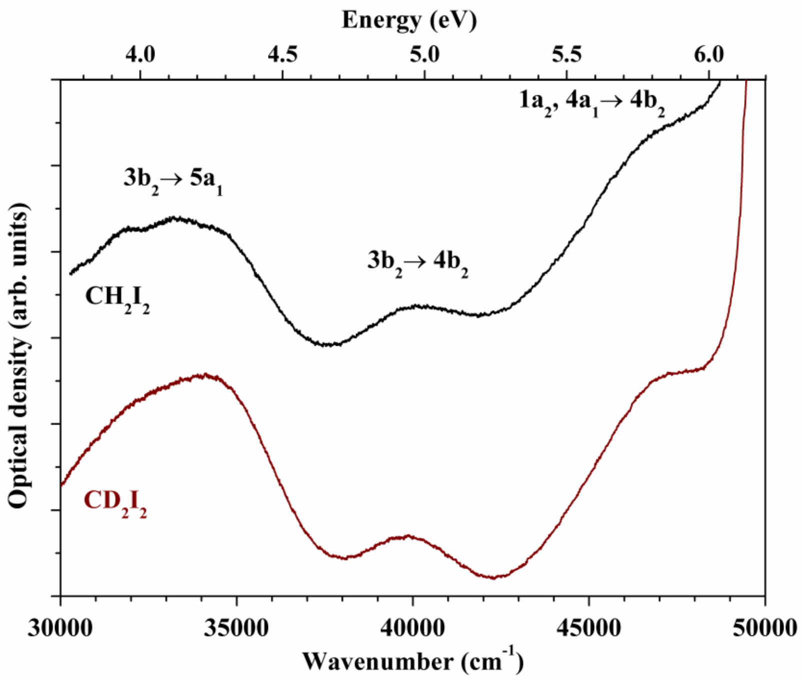

Fig. 2.5: UV Photoabsorption spectra of CH_2I_2 and CD_2I_2 in the region 30,000–50,000 cm^{-1}. Transitions predicted by TDDFT: PBE0/aug-cc-pVQZ are marked.

Following the early work by Ito *et al.* [43] in which the UV absorption spectrum was deconvoluted into four Gaussian bands, several authors have revisited this issue. For instance, Kawasaki *et al.* [44] proposed the first five excited states to be $^1B_1$, $^1B_1$, $^1B_2$, $^1A_1$, $^1A_1$ whereas the magnetic circular dichroism (MCD) results of Gedanken and Rowe [76], showing the presence of five distinct bands and a shoulder between 30,000 cm^{-1} to 50,000 cm^{-1} assign the first three excited states to $^1B_2$, $^1B_1$, $^1A_1$. Other workers have postulated that the four absorption features do not correspond to single excitations but may be composed of two or more overlapping electronic transitions, with curve crossings of electronic states also playing a possible role [48].

In the present work, these assignments are reviewed in light of TDDFT calculations of vertical excited states. The theoretically predicted valence states at the PBE0/aug-cc-pVQZ level of theory are listed in Table 2.9. Dipole forbidden states and states with very low oscillator strength are omitted from this table, as also states of mixed nature which are already included in Rydberg assignments. The first six singlet excited states including the forbidden A_2 state have been calculated earlier using the complete active space second order perturbation method (CASPT2) by Liu *et al.* [63]. Their results are shown in parentheses in Table 2.9 for comparison. It may be seen that excitation energies are in overall good agreement except for re-ordering of some of the states. However the predicted oscillator strengths differ considerably for some of the transitions.

Potential energy curves for the first eight singlet excited states generated at the same level of theory are shown in Fig. 2.6. The only earlier report of PECs of excited states is by Ya-Jun Liu *et al.* [63] who have investigated UV photolysis pathways using spin-orbit coupled multistate complete active space second order perturbation method and calculated potential energy curves for the first four singlet and triplet excited states. The present work is mainly concerned with explanation of spectral features observed in the UV photoabsorption spectrum. Since significant contribution from triplet states to the absorption intensity is generally not expected, only the singlet state PECs are considered here (*cf.* Fig. 2.6).

Table 2.9: Valence transitions for CH_2I_2 calculated by TDDFT: PBE0/aug-cc-pVQZ

Sym.	**Energy (eV)**	***f***	**Transition**	**Λ**	***A***
B_2	4.209 (4.37)	0.033 (0.006)	$3b_2 \rightarrow 5a_1$	0.61	-0.982
B_1	4.300 (4.04)	<0.001 (0.002)	$2b_1 \rightarrow 5a_1$	0.59	0.991
A_1	4.666 (4.77)	<0.001 (0.002)	$4a_1 \rightarrow 5a_1$	0.63	-0.979
A_2	4.486 (5.39)	0.000 (0.000)	$1a_2 \rightarrow 5a_1$	0.56	0.987
A_1	5.547 (6.13)	0.004 (0.004)	$3b_2 \rightarrow 4b_2$	0.51	-0.974
B_1	5.940 (6.54)	0.010 (0.044)	$1a_2 \rightarrow 4b_2$	0.50	0.976
B_2	6.096	0.005	$4a_1 \rightarrow 4b_2$	0.48	-0.796
B_2	**7.609**	**0.341**	**$2b_2 \rightarrow 5a_1$**	**0.54**	**-0.744**
B_2	7.728	0.001	$4a_1 \rightarrow 5b_2$	0.34	0.761
A_1	8.287	0.001	$3a_1 \rightarrow 5a_1$	0.61	-0.752
B_1	8.964	0.004	$2b_1 \rightarrow 11a_1$	0.36	-0.575
			$3b_2 \rightarrow 3a_2$		0.511
B_1	9.100	0.046	$4a_1 \rightarrow 5b_1$	0.39	0.520
B_2	**9.193**	**0.102**	**$3a_1 \rightarrow 4b_2$**	**0.53**	**0.613**
B_2	**9.448**	**0.297**	**$3a_1 \rightarrow 4b_2$**	**0.50**	**0.523**
			$2b_1 \rightarrow 3a_2$		**-0.592**
B_2	9.493	0.006	$2b_2 \rightarrow 6a_1$	0.29	0.964
B_1	9.810	0.040	$1b_2 \rightarrow 5a_1$	0.46	0.957
A_1	**9.823**	**0.215**	**$2b_2 \rightarrow 4b_2$**	**0.56**	**-0.513**
			$1a_2 \rightarrow 3a_2$		**0.561**
B_2	10.166	**0.760**	$3b_2 \rightarrow 12a_1$	0.49	0.778
B_2	10.309	0.003	$3b_2 \rightarrow 13a_1$	0.40	-0.888
A_1	**10.464**	**0.276**	**$3b_2 \rightarrow 9b_2$**	**0.49**	**0.706**
B_1	10.618	0.090	$4a_1 \rightarrow 7b_1$	0.45	-0.693
B_2	**10.635**	**0.222**	**$2b_2 \rightarrow 7a_1$**	**0.34**	**0.777**
A_1	10.715	0.003	$2b_2 \rightarrow 5b_2$	0.43	-0.617
B_2	10.836	0.028	$4a_1 \rightarrow 9b_2$	0.46	0.858
A_1	10.925	0.052	$4a_1 \rightarrow 13a_1$	0.44	-0.759
B_1	10.947	0.011	$3a_1 \rightarrow 3b_1$	0.29	-0.791
B_2	10.952	0.014	$2b_2 \rightarrow 8a_1$	0.31	-0.857
B_1	**10.964**	**0.216**	**$3a_1 \rightarrow 3b_1$**	**0.36**	**0.559**

f: oscillator strength, Λ: lambda diagnostic, *A*: excitation amplitude. States with high oscillator strength are shown in bold. Values in parentheses refer to the CASPT2(L3) results of Ref. [63].

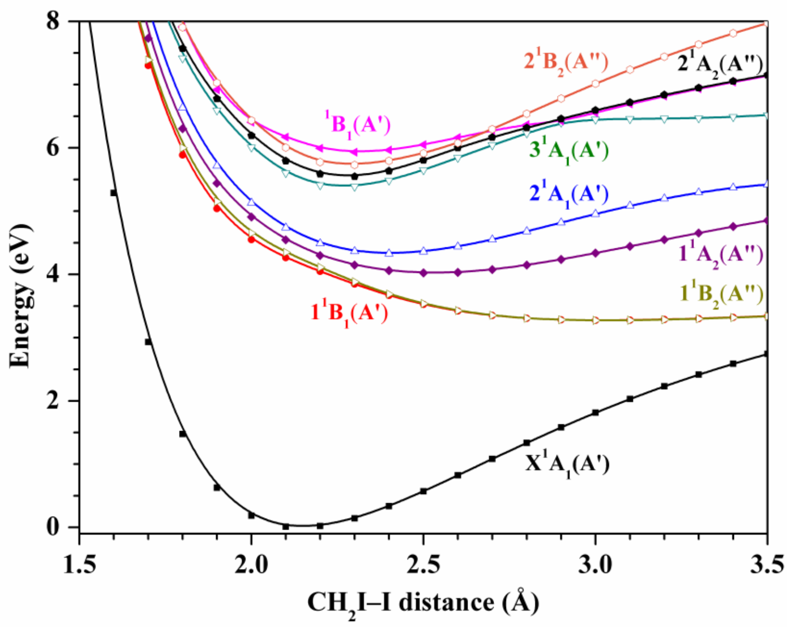

Fig. 2.6: Potential energy curves for first eight singlet excited states with respect to change in C–I bond length generated by PBE0/aug-cc-pVQZ

Excited states which could contribute to the broad 32000 cm^{-1} absorption band are 1^1B_2, 1^1B_1, 1^1A_2, 2^1A_1, of which the transition to 1^1A_2 is dipole forbidden. From the potential energy curves, it is seen that the 1^1B_2 and 1^1B_1 states are strongly repulsive while the 1^1A_2 and 2^1A_1 states have very shallow minima. Since the oscillator strengths of the allowed transitions X^1A_1–1^1B_1 and X^1A_1–2^1A_1 are very small (<0.001) it is concluded that the 1^1B_2 state with oscillator strength 0.033 is primarily responsible for the absorption in this region. The broad absorption band observed is due to the repulsive nature of the potential energy curve with respect to change in the C–I bond length in the Franck-Condon region. In the next two absorption features at 40,000 and 47,000 cm^{-1}, the possible states involved are 3^1A_1, 2^1A_2, 2^1B_1 and 2^1B_2 of which the 2^1A_2 state is forbidden and the other three states have comparable oscillator strengths (*cf.* Table 2.9).

The difference in energy between the 3^1A_1 and 2^1B_1 states is somewhat larger than the energy difference between 2^1B_1 and 2^1B_2. It seems reasonable to conclude that the band at 40,000 cm^{-1} is primarily due to 3^1A_1 whereas the 47,000 band is due to 2^1B_1 and 2^1B_2. The higher intensity of the 47,000 cm^{-1} feature is also in line with this inference. The feature at

47,000 cm^{-1} appears as a shoulder in the spectrum due to the very high intensity of the 6s transition (f = 0.181) which is quite close to it in energy. It may be noted that the PECs of these allowed states (3^1A_1, 2^1B_1 and 2^1B_2) do not show a repulsive behavior with respect to CH_2I–I distance, although they do have shallow minima. Thus the absorption spectrum in the UV region may be attributed to six allowed states 1^1B_2, 1^1B_1, 2^1A_1, 3^1A_1, 2^1B_1 and 2^1B_2, of which the oscillator strengths of 1^1B_1 and 2^1A_1 are small. These six states may be correlated satisfactorily with the MCD experiments of Gedanken *et al*. in which five distinct states and a shoulder were observed [76]. The above assignments are also consistent with earlier observations [40, 42] that the molecule preferentially dissociates into CH_2I and I atom on photoexcitation at ~32,000 cm^{-1} with photodissociation into CH_2 and I_2 gaining more importance at energies >40000 cm^{-1}.

Several high lying valence states and states with mixed character occur in the VUV region (>50,000 cm^{-1}) interspersed with the Rydberg states (*cf*. Table 2.9). Transitions to valence states having relatively large oscillator strengths (shown in bold type in the table) could account for the high underlying intensity observed in some parts of the VUV absorption spectrum, which cannot be accounted for by oscillator strengths of the Rydberg transitions alone. It is also worth mentioning here that photolysis of CH_2I_2 in the region 66,000–90,000 cm^{-1} has been shown to result in fragmentation into CH_2 and excited I_2 molecules by Okabe *et al*. [42]. They conclude, based on comparison of the absorption cross section of CH_2I_2 in this region with the I_2 ($^3\Pi_{2g}$) fluorescence excitation spectrum that the I_2 emission bands arise mainly from the underlying continuum (σ–σ* type of transitions) and not from the structured features corresponding to Rydberg transitions.

CHAPTER 3

ELECTRONIC SPECTROSCOPY OF DIBROMOMETHANE AND DIBROMOMETHANE-d$_2$

3.1 INTRODUCTION

The molecule studied in this chapter from the family of dihalomethanes is dibromomethane (CH_2Br_2). The principal source of CH_2Br_2 in nature is seawater where it is produced by marine macroalgae and is released into atmosphere by volatilization [77]. It is estimated that about 60% of the total oceanic emissions of CH_2Br_2 are from the open ocean and about 40% are from coastal regions [78]. In the troposphere, it is degraded by reacting with hydroxyl (·OH) radical which is produced by photolysis of ozone and thereby playing an important role in the ozone balance in the atmosphere [38, 79]. It has been shown in a recent study on global modeling of bromomethanes that CH_2Br_2 plays an important role in contributing reactive bromine to the stratosphere [78].

Photodissociation studies on CH_2Br_2 have been done by many workers using several techniques such as photoelectron photoion coincidence (PEPICO) [45, 56], ion velocity imaging [80, 81], resonance enhanced multiphoton ionization (REMPI) [82], laser induced [83] and cavity ring down spectroscopy [84]. The first few IPs of CH_2Br_2 have been determined by PEPICO [45, 56], photoelectron spectroscopy (PES) [72, 85] and Penning ionization electron spectroscopy (PIES) [85] experiments. Ultraviolet absorption cross sections of CH_2Br_2 at room temperature were measured by Molina *et al.* [79] and a temperature dependent study was carried out by Gillottay and co-workers [86]. Mössinger *et al.* [38] reported UV-visible absorption cross section over a range of temperatures and estimated the atmospheric life time of CH_2Br_2. Recently, Liu *et al.* [87] have performed spin orbit *ab-initio* calculations for photodissociation of CH_2Br_2 in the UV region.

The VUV absorption spectrum of CH_2Br_2 was reported for the first time using a hydrogen discharge lamp by Causley and Russell in 1975 [88]. Many of the observed lines were assigned to *ns* (up to $n = 9$) Rydberg series converging to three IPs, *viz.*, b_1, b_2 and ($a_1 + a_2$) and the first members of *np* and *nd* Rydberg transitions were assigned based on term value calculations. The third IP was designated as $a_1 + a_2$ as the a_1 and a_2 orbitals lie close in energy and the corresponding IPs were not resolved experimentally in the photoelectron spectra available at that time. In their work several observed peaks were left unassigned and a few features were given tentative assignments. To the best of knowledge, there has been no other experimental photoabsorption study of CH_2Br_2 in the VUV region till date; also the related theoretical studies are restricted to the UV region [82, 87]. Thus a complete understanding of the UV-VUV spectrum of CH_2Br_2 is still lacking.

In this chapter UV-VUV spectroscopy of dibromomethane in energy region of 4.3–11.8 eV using synchrotron radiation is reported. A complete Rydberg series and vibronic analysis is carried out to build a better understanding of the high-lying excited states of CH_2Br_2. The analysis is further supported by performing quantum chemical calculations in DFT and TDDFT framework. The work has resulted in assignments of observed spectrum of CH_2Br_2 to *ns*, *np* and *nd* Rydberg series converging to four IPs. Proposed assignments are confirmed and consolidated by the UV-VUV photoabsorption spectrum of the deuterated species, diboromomethane-d_2 (CD_2Br_2), whose spectrum is reported here for the first time.

3.2 METHODOLOGY

3.2.1 EXPERIMENTAL

The photoabsorption studies are carried out using the Photophysics beamline which has been described in Chapter 1. Samples of CH_2Br_2 and CD_2Br_2 (Sigma Aldrich) with stated purities >99.5 %, are subjected to several freeze-pump-thaw cycles before introducing into the cell. In this study, absorption spectra are recorded at several sample pressures between 0.001 and 1 mbar. In the VUV region, the optimum pressure is found to be ~0.01 mbar, while in the UV region higher sample pressures ~1 mbar is used to obtain clear absorption features. Atomic lines of xenon are used as a reference to calibrate the wavelength scale. Details of the the experimental setup are described in Chapter 1.

3.2.2 COMPUTATIONAL

CH_2Br_2 belonging to the C_{2V} point group is analogous to CH_2I_2 and as before the coordinate system used for calculations is chosen such that the H–C–H group lies in the XZ plane and Br-C-Br group in the YZ plane. The ground state geometries of CH_2Br_2 and CD_2Br_2 are optimized and the vibrational frequencies are calculated using the density functional theory (DFT) and Møller-Plesset perturbation theory (MP2) with different basis sets like Pople's split valence basis set 6-311G with d- and p-type of polarization functions [33, 89], the correlation consistent basis sets cc-pV*n*Z and aug-cc-pV*n*Z (*n*=D, T, Q, 5) [36, 37]. Electron correlation in the DFT calculation is included by the use of hybrid exchange correlation functionals *viz.* B3LYP [25, 65] and PBE0 [64]. The ground state geometry optimization and vibrational frequency calculations for $CH_2Br_2^+$ and $CD_2Br_2^+$ are carried out using the unrestricted Hartree-Fock (UHF) reference. The vertical excited state energies of CH_2Br_2 up to ~12 eV are calculated using TDDFT at the optimized ground state geometry.

3.3 RESULTS AND DISCUSSION

3.3.1 COMPUTATIONAL RESULTS FOR THE GROUND STATES OF NEUTRAL AND IONIC SPECIES

The optimized ground state geometries, calculated by DFT and MP2 methods using aug-cc-pV5Z basis set, of CH_2Br_2 and $CH_2Br_2^+$ are shown in Tables 3.1 and 3.2 respectively. The combination MP2/aug-cc-pV5Z is found to yield the best agreement with the experimental values of the ground state bond lengths and bond angles of CH_2Br_2 [90]. Also, DFT produces better results with PBE0 than with B3LYP. The ground state vibrational frequencies of CH_2Br_2 and CD_2Br_2 for both neutral and ionized molecules at PBE0/aug-cc-pV5Z level are shown in Table 3.3. The values are compared with earlier experimental [90, 91] and theoretical [56, 92, 93] works.

Table 3.1: Optimized bond lengths (Å) and bond angles (deg.) of the ground state of CH_2Br_2 using DFT an MP2 methods

	r(C–Br)	**r(C–H)**	**∠(Br–C–Br)**	**∠(H–C–Br)**	**∠(H–C–H)**
B3LYP/aug-cc-pVQZ	1.945	1.080	114.1	107.6	112.5
B3LYP/aug-cc-pV5Z	1.945	1.080	114.1	107.6	112.5
PBE0/aug-cc-pVQZ	1.922	1.083	113.7	107.8	112.0
PBE0/aug-cc-pV5Z	1.922	1.083	113.7	107.8	112.0
MP2/aug-cc-pVQZ	1.921	1.081	113.2	107.9	111.9
Experimental[a]	1.925	1.097	112.9	108.3	110.9

[a] Ref. [90]

Table 3.2: Optimized bond lengths (Å) and bond angles (deg.) of the ground state of $CH_2Br_2^+$ using DFT an MP2 methods

	r(C–Br)	**r(C–H)**	**∠(Br–C–Br)**	**∠(H–C–Br)**	**∠(H–C–H)**
B3LYP/aug-cc-pVQZ	1.945	1.082	94.1	111.0	116.7
B3LYP/aug-cc-pV5Z	1.944	1.082	94.0	111.0	116.7
PBE0/aug-cc-pVQZ	1.921	1.084	92.6	111.3	116.5
PBE0/aug-cc-pV5Z	1.921	1.084	92.6	111.3	116.5
MP2/aug-cc-pVQZ	1.921	1.083	91.0	111.5	117.0

Table 3.3: Ground state vibrational frequencies (in cm^{-1}) of the neutral and ionic dibromomethane calculated at the level PBE0/aug-cc-pV5Z

	Neutral				**Ionic**		
Normal Mode (symmetry)	**CH_2Br_2**		**CD_2Br_2**		**$CH_2Br_2^+$**		**$CD_2Br_2^+$**
	This work	**Expt.[a]**	**This work**	**Expt.[a]**	**This work**	**Calc.[b]**	**This work**
ν_1: CH sym. stretch (a_1)	3143	3009	2278	2196	3140	3141	2272
ν_2: CH_2 bend (a_1)	1432	1382	1051	1027	1424	1438	1046
ν_3: CBr sym. stretch (a_1)	599	588	570	550	669	619	636
ν_4: CBr_2 bend (a_1)	171	169	170	172	180	162	179
ν_5: CH_2 twist (a_2)	1123	1095	796	784	1040	1053	738
ν_6: CH asym. stretch (b_2)	3231	3073	2406	2313	3255	3234	2429
ν_7: CH_2 rock (b_2)	806	812	635	636	888	883	681
ν_8: CH_2 wag (b_1)	1217	1195	916	901	1175	1202	887
ν_9: CBr asym. stretch (b_1)	668	653	629	610	578	527	550

[a]Ref. [91], [b]Ref. [56]

The molecular orbital configuration of CH_2Br_2 calculated by DFT is [*core*] $(1a_1)^2$ $(1b_2)^2$ $(2a_1)^2$ $(1b_1)^2$ $(3a_1)^2$ $(2b_2)^2$ $(4a_1)^2$ $(1a_2)^2$ $(2b_1)^2$ $(3b_2)^2$: X^1A_1. The ordering of the four highest occupied MOs in early PES studies has been rather controversial, *i.e.*, $3b_2$, $2b_1$, $1a_2$, $4a_1$ by Dixon *et al.* [72] and Kishimoto *et al.* [85] and $2b_1$, $1a_2$, $3b_2$, $4a_1$ by Potts *et al.* [70]. The present quantum chemical calculation clearly shows the order to be $3b_2$, $2b_1$, $1a_2$, $4a_1$ and is confirmed by repeating the calculations for several basis sets and methods.

The contour plots of the four HOMOs and the four LUMOs generated using the software MacMolPlt [20] are shown in Figure 3.1. In all four HOMOs, non-bonding character corresponding to bromine lone pair is observed with additional weak C–H bonding character in $4a_1$ and $2b_1$ orbitals. All the LUMOs show non-bonding character with $5a_1$ and $4b_2$ having lone pair on C and Br atoms while $6a_1$ and $3b_1$ show lone pair only on the C atom. The energy level diagram of these orbitals with a few of the Rydberg transitions marked is shown in Figure 3.2. The correlation of theoretically calculated energies and experimentally observed transitions are discussed in the next section.

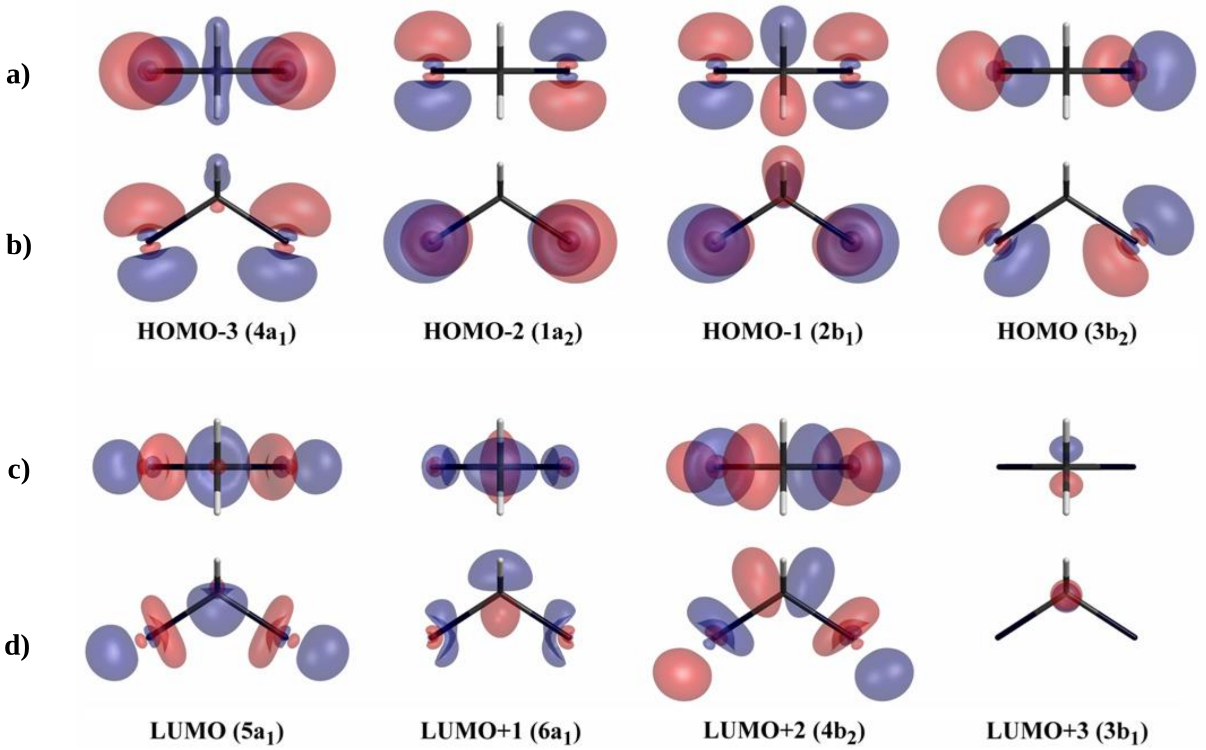

Fig. 3.1: Contour plots of the four HOMOs and four LUMOs of CH_2Br_2 at PBE0/aug-cc-pV5Z level of theory. HOMOs viewed along (a) Z axis and (b) X axis, LUMOs viewed along (c) Z axis and (d) X axis

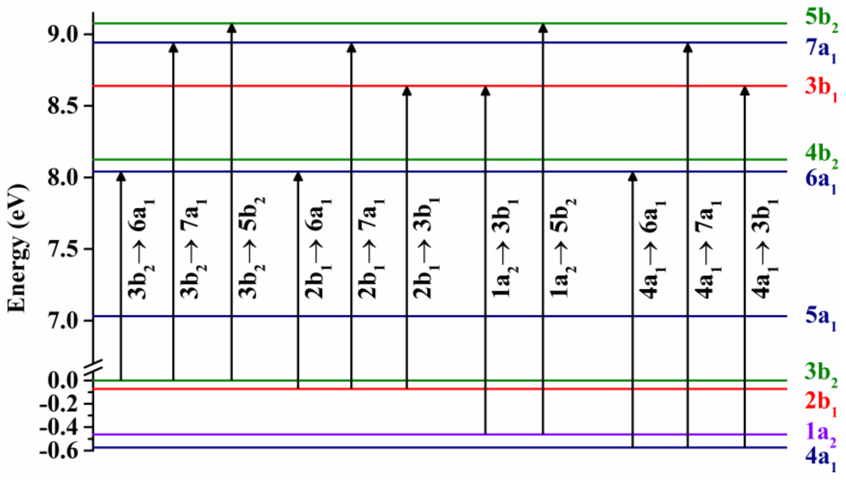

Fig. 3.2: Energy level diagram of CH_2Br_2 showing first few Rydberg transitions. The zero of the energy scale is fixed at the energy of the HOMO ($3b_2$).

3.3.2 Experimentally Observed Rydberg Series and Correlation with Computed Vertical Excited States

The photoabsorption spectra of CH_2Br_2 and CD_2Br_2 in the region 50,000–95,000 cm^{-1} (6.2–11.8 eV) are shown in Figure 3.3. The spectra are quite structured and may be divided into four energy regions (1) 6.8–7.8 eV with four diffuse bands, (2) 7.8–8.7 eV with sharp structure, (3) 8.6–9.6 eV with intense peaks and (4) >9.7 eV with diffuse peaks. Note here that the regions (1)–(3) are observed by Causley *et al.* [88] while the region (4) is additionally observed in this work. The first four IPs of CH_2Br_2 arising from excitation of an electron from the outermost Cl non-bonding orbitals have been measured at 11.32, 11.36, 12.16 and 12.27 eV by photoelectron spectroscopy [85]. Several Rydberg transitions of type *ns*, *np* and *nd* converging to these IPs are identified (*cf.* Tables 3.4–3.7), using the standard Rydberg formula (Eq. (1.5)).

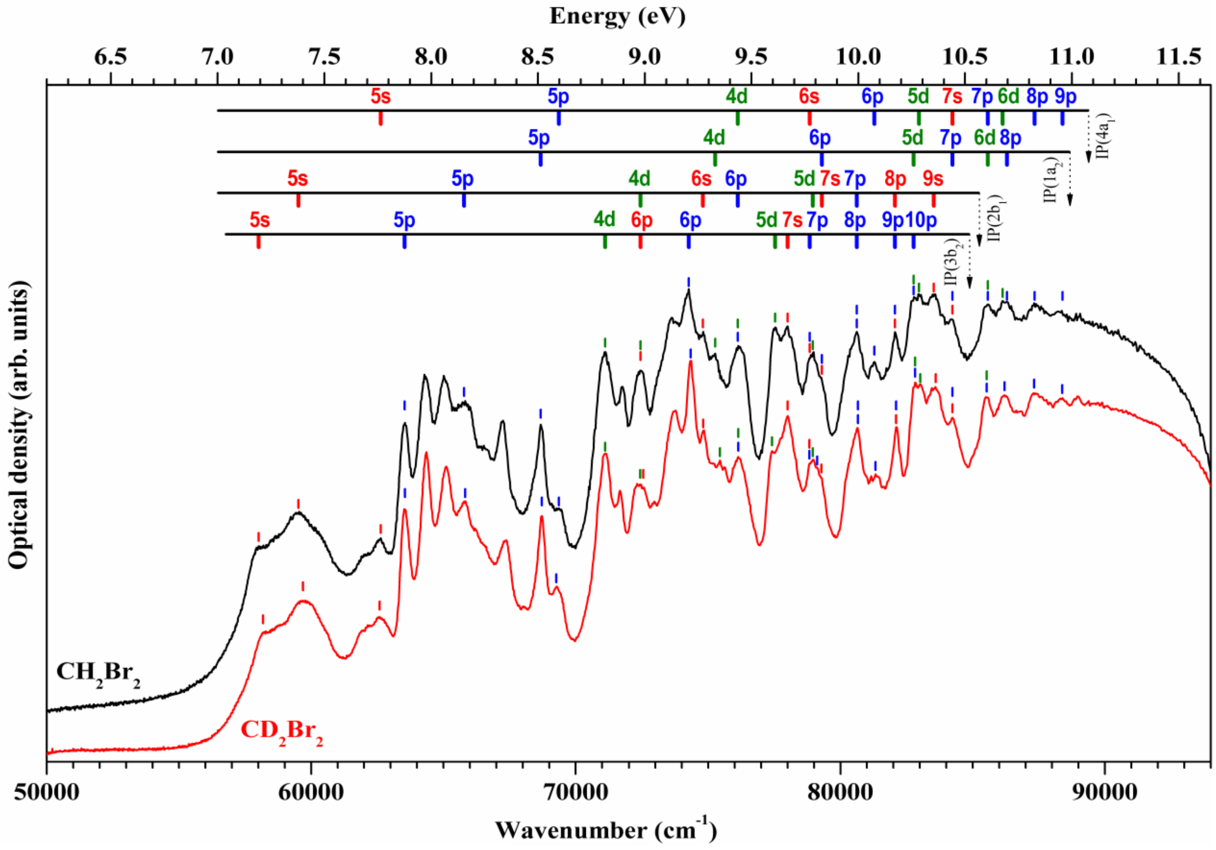

Fig. 3.3: VUV photoabsorption spectra of CH_2Br_2 and CD_2Br_2 showing Rydberg series converging to first four IPs at 10.52 ($3b_2$), 10.74 eV ($2b_1$), 11.21eV ($1a_2$) and 11.30ev ($4a_1$)

The *ns* orbitals are expected to have a_1 symmetry; therefore transitions of type $1a_2 \rightarrow ns$ are forbidden by the symmetry selection rules for C_{2v} point group and are expected to have zero oscillator strengths. Thus, *ns* series are observed only for IPs corresponding to

b_1, b_2 and a_1 while *np* and *nd* series are observed for all four IPs. In each Rydberg series, if n_{max} denotes the maximum observed value of *n*, then for the transitions $2b_1$, $3b_2$, $4a_1 \rightarrow ns$, n_{max}=9, 7, 7 respectively. In the case of *np* Rydberg series, n_{max} is found to be 10, 7, 8, 9 corresponding to the transitions $3b_2$, $2b_1$, $1a_2$, $4a_1 \rightarrow np$ respectively. Due to the closely spaced IPs, the higher members of the Rydberg series are overlapped. Consequently only the first few members of each series are clearly distinguishable, particularly in the case of the *nd* series, where n_{max}= 6 for $1a_2$ and $4a_1$ each and n_{max}=5 for $3b_2$ and $2b_1$ each could be identified. The quantum defect values obtained (*c.f.* Table 3.4–7) are close to the atomic quantum defect values for s, p and d orbitals of Br, *i.e.*, 2.96, 2.51 and 1.10 respectively [94].

Table 3.4: Rydberg series converging to IP ($3b_2$) = 10.52 eV observed in VUV photoabsorption spectrum of dibromomethane

Experimentally observed peak position[a]			**Calculated by TDDFT: PBE0/aug-cc-pV5Z**					**O–C**
Assignment	**CH_2Br_2**[b]	**CD_2Br_2**	**E (eV)**	***f***	**Transition**	***A***	**Λ**	
5s	7.192 (2.98) *7.193*	7.213 (2.97)	7.025	0.043	$3b_2 \rightarrow 6a_1$	-0.95	0.30	0.167
6s	8.983 (3.02)* *9.093*	8.206 (3.58)	8.591	0.023	$3b_2 \rightarrow 8a_1$	-0.88	0.25	0.392
7s	9.671 (3.00) *9.767*	9.672 (3.00)	9.214	0.008	$3b_2 \rightarrow 10a_1$	-0.65	0.38	0.457
5p	7.876 (2.73)	8.588 (2.35)	8.017	0.001	$3b_2 \rightarrow 7a_1$	0.98	0.23	-0.141
			8.169	0.019	$3b_2 \rightarrow 5b_2$	-0.93	0.37	-0.293
6p	9.208 (2.78)	9.217 (2.77)	8.991	0.003	$3b_2 \rightarrow 9a_1$	-0.81	0.27	0.216
			8.886	0.029	$3b_2 \rightarrow 6b_2$	0.90	0.26	0.321
7p	9.776 (2.72)*	9.774 (2.73)*	9.866	0.112	$3b_2 \rightarrow 11a_1$	0.70	0.30	-0.090
			9.543	0.014	$3b_2 \rightarrow 7b_2$	0.53	0.25	0.000
8p	9.996 (2.90)*	10.001 (2.88)*	10.991	0.149	$3b_2 \rightarrow 12a_1$	0.91	0.30	-0.995
			10.288	0.021	$3b_2 \rightarrow 8b_2$	0.89	0.30	-0.292
9p	10.174 (2.73)*	10.181 (2.67)*	11.714	0.002	$3b_2 \rightarrow 13a_1$	-0.75	0.36	-1.540
			11.646	0.236	$3b_2 \rightarrow 9b_2$	0.50	0.44†	0.000
10p	10.263 (2.73)*	10.269 (2.64)*	11.908	0.376	$3b_2 \rightarrow 14a_1$	-0.70	0.40	-1.645
			12.014	0.083	$3b_2 \rightarrow 10b_2$	-0.93	0.39	-1.751
4d	8.816 (1.17)	8.816 (1.17)	8.957	0.008	$3b_2 \rightarrow 2a_2$	-0.95	0.17	-0.140
5d	9.613 (1.13)	9.599 (1.16)	10.524	0.016	$3b_2 \rightarrow 3a_2$	0.89	0.33	-0.910

[a]quantum defect value in the parenthesis, [b]peak positions from Ref. [88] in italics, *blended line, *f*: oscillator strength, *A*: excitation amplitude, Λ: lambda diagnostic, †valence-Rydberg mixed nature, O–C: difference of observed and calculated energies in eV

Table 3.5: Rydberg series converging to IP ($2b_1$) = 10.74 eV observed in VUV photoabsorption spectrum of dibromomethane

Experimentally observed peak position[a]			**Calculated by TDDFT: PBE0/aug-cc-pV5Z**					**O–C**
Assignment	**CH_2Br_2**[b]	**CD_2Br_2**	**E (eV)**	***f***	**Transition**	***A***	**Λ**	
5s	7.378 (2.99) *7.378*	7.400 (2.98)	7.052	0.059	$2b_1 \rightarrow 6a_1$	0.91	0.35	0.326
6s	9.275 (2.95) *9.327*	9.277 (2.95)	8.698	0.037	$2b_1 \rightarrow 8a_1$	-0.86	0.31	0.576
7s	9.831 (3.13)* *9.991*	9.829 (3.13)	9.305	0.001	$2b_1 \rightarrow 10a_1$	0.98	0.27	0.526
8s	10.174 (3.10)* *10.288*	10.181 (3.07)*	11.062	0.067	$2b_1 \rightarrow 12a_1$	-0.91	0.38	-0.888
9s	10.357 (3.04) *10.466*	10.365 (2.98)	11.645	0.039	$2b_1 \rightarrow 13a_1$	0.75	0.37	-1.288
5p	8.155 (2.71)	8.160 (2.70)	8.089	0.047	$2b_1 \rightarrow 7a_1$	0.98	0.27	0.067
			7.847	0.010	$2b_1 \rightarrow 3b_1$	-0.98	0.22	0.309
6p	9.438 (2.77)*	9.439 (2.77)*	9.060	0.002	$2b_1 \rightarrow 9a_1$	-0.93	0.21	0.378
			8.982	0.005	$2b_1 \rightarrow 4b_1$	-0.94	0.28	0.456
7p	9.996 (2.72)*	10.001 (2.71)*	9.852	0.024	$2b_1 \rightarrow 11a_1$	0.97	0.29	0.144
			9.456	0.010	$2b_1 \rightarrow 5b_1$	-0.86	0.25	-0.540
4d	8.983 (1.22)*	8.160 (1.70)	9.039	0.128	$2b_1 \rightarrow 2a_2$	-0.79	0.29	-0.056
5d	9.791 (1.21)	9.790 (1.22)	10.573	0.005	$2b_1 \rightarrow 3a_2$	-0.65	0.41†	-0.782

[a]quantum defect value in the parenthesis, [b]peak positions from Ref. [88] in italics, *blended line, *f*: oscillator strength, *A*: excitation amplitude, Λ: lambda diagnostic, †valence-Rydberg mixed nature, O–C: difference of observed and calculated energies in eV

Table 3.6: Rydberg series converging to IP ($1a_2$) = 11.21 eV observed in VUV photoabsorption spectrum of dibromomethane

Experimentally observed peak position[a]			**Calculated by TDDFT: PBE0/aug-cc-pV5Z**					**O–C**
Assignment	**CH_2Br_2**[b]	**CD_2Br_2**	**E (eV)**	***f***	**Transition**	***A***	**Λ**	
5p	8.514 (2.75)	8.520 (2.75)	8.240	0.024	$1a_2 \rightarrow 3b_1$	-0.97	0.19	0.274
			8.525	0.015	$1a_2 \rightarrow 5b_2$	-0.81	0.33	-0.011
6p	9.831 (2.86)	9.810 (2.88)	9.290	0.073	$1a_2 \rightarrow 4b_1$	-0.55	0.29	0.000
			9.335	0.001	$1a_2 \rightarrow 6b_2$	0.96	0.23	0.497
7p	10.445 (2.78)	10.444 (2.79)*	9.847	0.004	$1a_2 \rightarrow 5b_1$	0.84	0.22	0.598
			10.065	0.034	$1a_2 \rightarrow 7b_2$	-0.97	0.24	0.380
8p	10.699 (2.84)	10.688 (2.90)*	10.408	0.144	$1a_2 \rightarrow 6b_1$	-0.86	0.44†	0.291
			10.797	0.105	$1a_2 \rightarrow 8b_2$	-0.95	0.34	-0.099
4d	9.332 (1.31)	9.353 (1.29)	9.413	0.001	$1a_2 \rightarrow 2a_2$	0.65	0.26	0.081
5d	10.263 (1.21)	10.269 (1.20)*	10.823	0.007	$1a_2 \rightarrow 3a_2$	0.57	0.53†	0.000
6d	10.610 (1.24)	10.604 (1.26)*	–	–	–	–	–	–

[a]quantum defect value in the parenthesis, *blended line, *f*: oscillator strength, *A*: excitation amplitude, Λ: lambda diagnostic, †valence-Rydberg mixed nature, O–C: difference of observed and calculated energies in eV

Table 3.7: Rydberg series converging to IP ($4a_1$) = 11.30 eV observed in VUV photoabsorption spectrum of dibromomethane

Experimentally observed peak position[a]			Calculated by TDDFT: PBE0/aug-cc-pV5Z					O–C
Assignment	**CH_2Br_2[b]**	**CD_2Br_2**	**E (eV)**	***f***	**Transition**	***A***	**Λ**	
5s	7.764 (3.04) *7.765*	7.760 (3.04)	7.609	0.027	$4a_1\rightarrow6a_1$	0.96	0.32	0.155
6s	9.776 (3.01)* *9.665*	9.774 (3.01)*	9.195	0.027	$4a_1\rightarrow8a_1$	-0.94	0.29	0.580
7s	10.445 (3.01)* *10.369*	10.444 (3.01)*	9.825	0.005	$4a_1\rightarrow10a_1$	-0.90	0.33	0.619
5p	8.600 (2.76)	8.588 (2.76)	8.578	0.023	$4a_1\rightarrow7a_1$	0.91	0.29	0.022
			8.340	0.000	$4a_1\rightarrow3b_1$	0.96	0.15	0.260
6p	10.079 (2.66)	10.083 (2.66)	9.650	0.005	$4a_1\rightarrow9a_1$	0.67	0.25	0.000
			9.455	0.027	$4a_1\rightarrow4b_1$	0.94	0.21	-0.624
7p	10.610 (2.56)*	10.604 (2.58)*	10.405	0.054	$4a_1\rightarrow11a_1$	-0.88	0.34	0.205
			9.948	0.000	$4a_1\rightarrow5b_1$	-0.96	0.17	0.662
8p	10.830 (2.62)	10.826 (2.64)	11.524	0.002	$4a_1\rightarrow12a_1$	0.91	0.33	-0.694
			10.398	0.001	$4a_1\rightarrow6b_1$	-0.90	0.36	0.431
9p	10.960 (2.67)	10.958 (2.69)	–	–	–	–	–	–
4d	9.438 (1.30)	9.439 (1.30)*	9.409	0.056	$4a_1\rightarrow6b_2$	0.72	0.29	0.029
5d	10.288 (1.33)	10.293 (1.32)	10.146	0.013	$4a_1\rightarrow7b_2$	0.97	0.25	0.141
6d	10.679 (1.32)	10.688 (1.29)*	10.864	0.050	$4a_1\rightarrow8b_2$	-0.81	0.32	-0.185

[a]quantum defect value in the parenthesis, [b]assignments from Ref. [88] in italics, *blended line, *f*: oscillator strength, *A*: excitation amplitude, Λ: lambda diagnostic, O–C: difference of observed and calculated energies in eV

Based on the quantum defect analysis (*c.f.* Tables 3.4, 3.5 and 3.7), the three transitions at 7.192, 7.378 and 7.764 eV are identified as corresponding to excitations $3b_2$, $2b_1$, $4a_1\rightarrow5s$ respectively, in agreement with the assignment of the bands at 7.193, 7.378, 7.686 eV by Causley and Russell [88]. The transitions $3b_2$, $2b_1$, $4a_1\rightarrow6s$ are identified at 8.982, 9.275 and 9.776 eV respectively. Transitions corresponding to excitations $3b_2$, $2b_1$, $4a_1\rightarrow7s$ are observed at 9.671, 9.831 and 10.445 eV respectively. Higher *ns* series members (n>7) are observed only for $2b_1\rightarrow ns$. The bands at 10.174 and 10.357 eV are assigned to $2b_1\rightarrow8s$ and $2b_1\rightarrow9s$ respectively.

Using term value calculations, Causley and Russell [88] assigned the b_1, b_2, $(a_1+a_2)\rightarrow5p$, 4d transitions, *i.e.*, the first members of *np* and *nd* series, but did not assign higher members of these series. In this work, several higher members of *np* and *nd* Rydberg series are observed and assigned. Assignments of *ns* series in this work differ from those of Causley and Russell [88] in some places. For instance, the peaks 9.665, 10.369, 9.767 and 10.288 eV assigned by them to $4a_1 \rightarrow 6s$, $4a_1 \rightarrow 7s$, $3b_2 \rightarrow 7s$ and $2b_1 \rightarrow 8s$ are reassigned in this work to $3b_2 \rightarrow 7s$, $2b_1 \rightarrow 9s$, $4a_1 \rightarrow 6s$ and $4a_1 \rightarrow 5d$ respectively. The peak reported earlier [88] at 9.991 for the transition $2b_1 \rightarrow 7s$ is found in the present study to belong to the blended transitions $3b_2 \rightarrow 8p$ and $2b_1 \rightarrow 7p$ at 9.996 eV. The peak observed by Causley and Russell [88] at 9.991 eV has appeared as a weak shoulder in the present spectrum while the clearer peak at 10.445 eV (*c.f.* Fig. 3.3) was not reported by them. The $3b_2 \rightarrow 6s$ transition assigned by them at 9.093 eV is observed in the present study at 8.983 eV consisting of blended transition $3b_2 \rightarrow 6s$ and $3b_1 \rightarrow 4s$. Note here that Causley and Russell used only three values of IPs 10.61, 10.82 and 11.28 eV corresponding to b_2, b_1 and (a_1+a_2) as known at that time. Recently, from advanced experimental techniques [56, 85] the values of IPs for $1a_2$ and $4a_1$ are distinguishably known (11.21 and 11.30 eV) together with more precise values of other IPs.

In addition to the availability of precise values of IPs, the spectrum of the deuterated isotopologue (CD_2Br_2) has played an important role in successful identification and assignment of Rydberg series in the present study. The comparative study of two isotopic species helped in assigning a few transitions which are not well resolved for one of the isotopic species but resolved clearly in other. For example, the transitions $3b_2 \rightarrow 6s$ and $2b_1 \rightarrow 4d$, blended at 8.983 eV in CH_2Br_2 are resolved at 8.996 and 8.980 eV respectively for CD_2Br_2. Similarly, the peak observed at 9.831 eV corresponding to $2b_1 \rightarrow 7s$ and $1a_2 \rightarrow 6p$ for CH_2Br_2 appear distinctly at 9.829 and 9.810 eV in CD_2Br_2. Transitions $1a_2 \rightarrow 8p$ and $4a_1 \rightarrow 6d$ at 10.699 and 10.679 eV respectively are resolved in CH_2Br_2 which are blended in CD_2Br_2 at 10.688 eV. The comparative study of CD_2Br_2 and CD_2Br_2 thus has served well to resolve uncertainties such as these.

Taking the ionic frequencies (*cf.* Table 3.3) to be a reasonable estimate of the excited Rydberg state frequencies, the isotopic shift between the Rydberg series origins in CH_2Br_2 and CD_2Br_2 is calculated from Eq (1.7) to be ~200 cm^{-1} (0.025 eV). A comparison of the spectra of CH_2Br_2 and CD_2Br_2 (*c.f.* Fig. 3.3) shows that there exists an isotope shift of ~–180 to +110 cm^{-1} (–0.022 to +0.014 eV) in the peak positions of Rydberg states. The variation of isotopic shift from state to state may be attributed to excited state vibrational frequencies being somewhat different from the calculated ionic frequencies. It may also be noted that since the experimental resolution is ~0.006 eV at 6 eV and ~0.01 eV at 10 eV, shifts within these values are not really significant.

Correlation of vertical excitation energies, oscillator strengths and Λ diagnostic values calculated by TDDFT with PBE0/aug-cc-pV5Z with experimental energies are shown in Tables 3.4–7. The correspondence between theoretical and experimental data is established by taking into account the energy and symmetries of the initial and final MOs associated with every Rydberg member. The final MOs is expected to be of a_1 symmetry for the *ns* Rydberg series while for the *np* and *nd* series, the final orbitals are expected to be of the same symmetry within a given series converging to a particular IP. The correlation of calculated oscillator strengths with experimentally observed intensities is feasible in lower energy regions but becomes difficult in higher energy regions due to increased blending of transitions. As mentioned in Chapter 1, the accuracy of calculated excited state energies is expected to be very good up to 1 eV higher than the energy of the HOMO [31], *i.e.*, ~9.2 eV in this case. For higher excitation energies (>9.2 eV), the accuracy of the calculation decreases and the difference between observed and calculated energies (*cf.* Tables 3.4–3.7) becomes larger. While low lying excited states result from single orbital excitations, mixing of two or more molecular orbital excitations with comparable amplitude becomes more common for high lying states (*cf.* Tables 3.4–3.7). In our analysis, only those excitations are considered for which the absolute value of TDDFT excitation amplitude is ≥0.5. In case of *np* series, two sets of calculated transitions are correlated with experimentally observed energies (*cf.* Tables 3.4–3.7). Observation of more than one series for a particular angular momentum *l*>0 is possible in principle but they are not distinguished in the present experiment.

3.3.3 VIBRONIC ASSIGNMENTS

In the region 63,000–74,000 cm^{-1} region, a few spectral features can be attributed to vibronic transitions as marked in Figure 3.4. Here, to a greater extent than in the Rydberg series analysis, the isotopic shift in vibronic bands is very important in verifying the assignments. The Rydberg transition 3b$_2$→5p (63,523 cm^{-1}) of CH_2Br_2 is accompanied by vibronic peaks at 64,310, 65,018, 65,778 cm^{-1} at intervals of ~787, 1495 and 2255 cm^{-1}.

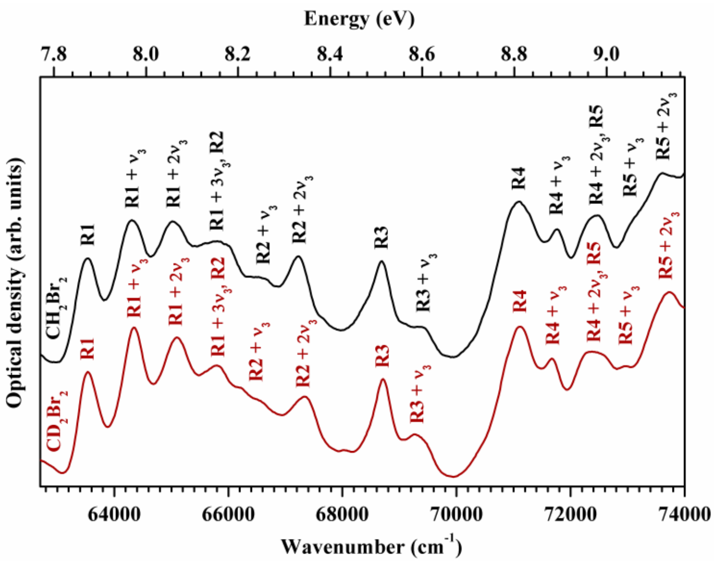

Fig. 3.4: Vibrational features in the photoabsorption spectra of CH_2Br_2 and CD_2Br_2. R1, R2, R3, R4 and R5 denote the Rydberg transitions 3b$_2$→5p, 2b$_1$→5p, 1a$_2$→5p, 3b$_2$→4d and 2b$_1$→4d respectively.

Causley and Russell [88] assigned the first two peaks to the totally symmetric modes ν_3' and ν_2' respectively (primes denote vibrational frequencies in the upper electronic states) since these two intervals match with the vibrational frequencies of these two modes in the ground state. These peaks are observed at 64,344, 65,088 and 65,813 cm^{-1} with intervals 804, 1548 and 2273 cm^{-1} from the origin 63,540 cm^{-1} in CD_2Br_2 spectrum. Isotopic shift in the peak positions is found to be very small (<70 cm^{-1}). Assignment of the band at 65,018 cm^{-1} to the ν_2' (CH_2 bend) mode is ruled out on the basis of the observation that the frequency of ν_2' changes from 1382 to 1027 cm^{-1} in going from CH_2Br_2 to CD_2Br_2 in the ground state (*c.f.* Table 3.8) and similar trend is expected in the excited state. Relative insensitivity to deuterium substitution suggests that the vibrational mode contributing to these peaks should involve the CBr_2 group. Therefore these three peaks are assigned to the progression of $n\nu_3'$ (n=1, 2 and 3) of $3b_2 \rightarrow 5p$ Rydberg state. Using the same logic, bands at 66,518 and 67,235 cm^{-1} of CH_2Br_2 observed at 66,539 and 67,353 cm^{-1} in CD_2Br_2 can be assigned to $n\nu_3'$ (n=1 and 2) of $2b_1 \rightarrow 5p$ Rydberg state in contrast to the earlier study [88] where they are assigned to ν_3' and ν_2' modes respectively.

It should be noted that the peak at 69,265 cm^{-1} (blue shifted by ~550 cm^{-1} from 68,716 cm^{-1}) in CD_2Br_2 spectrum is sharp and it is assigned to $4a_1 \rightarrow 5p$ transition on the basis of quantum defect value. In case of CH_2Br_2 the same transition is observed at 69,362 cm^{-1} and the vibrational mode $1a_2 \rightarrow 5p+\nu_3'$ may be coinciding with Rydberg transition $4a_1 \rightarrow 5p$ which is consistent with the earlier assignment [88]. Similarly peaks observed in CH_2Br_2 (CD_2Br_2) at 71,747 (71,686) and 72,327 (72,316) cm^{-1} are assigned to ν_3' of $3b_2 \rightarrow 4d$ Rydberg state. Peaks of CD_2Br_2 at 72,963 and 73,668 cm^{-1} are assigned to $n\nu_3'$ (n=1 and 2) of $3b_2 \rightarrow 4d$ Rydberg state. In this case, n=1 component is not resolved in the CH_2Br_2 spectrum and n=2 component appears at 73,669 cm^{-1}. Table 3.8 shows vibronic assignment for CH_2Br_2 and CD_2Br_2 in the present study and comparison with previous assignments for CH_2Br_2. Here it is worth mentioning that the spectrum of CD_2Br_2 in the present study plays an important role in confirming all above vibronic assignments to excitation of the ν_3 mode alone instead of ν_3' and ν_2' as suggested by Causley and Russell [88].

Table 3.8: Vibrational features (values in cm^{-1}) observed in VUV photoabsorption spectra of dibromomethane. ΔE is the difference in energy between the Rydberg series origin and the vibronic band.

Assignment	**Present study**				**Previous study for CH_2Br_2 [88]**	
	CH_2Br_2		**CD_2Br_2**			
	Peak position	**ΔE**	**Peak position**	**ΔE**	**Position**	**Assignment**
$3b_2\rightarrow 5p$	**63,523**		**63,540**			
$3b_2\rightarrow 5p+\nu_3'$	64,310	787	64,344	804	64,310	4p (b_2)$\rightarrow$5p+ν_3'
$3b_2\rightarrow 5p+2\nu_3'$	65,018	1495	65,088	1548	65,063	4p (b_2)$\rightarrow$5p+ν_2'
$3b_2\rightarrow 5p+3\nu_3'$	65,778	2255	65,813	2273		
$2b_1\rightarrow 5p$	**65,778**		**65,813**			
$2b_1\rightarrow 5p+\nu_3'$	66,518	740	66,539	726	66,495	4p (b_1)$\rightarrow$5p+ν_3'
$2b_1\rightarrow 5p+2\nu_3'$	67,235	1457	67,353	1540	67,233	4p (b_1)$\rightarrow$5p+ν_2'
$1a_2\rightarrow 5p$	**68,668**		**68,716**			
$1a_2\rightarrow 5p+\nu_3'$	69,362	694	69,265	549	69,330	4p (a_1 +a_2)$\rightarrow$5p+ν_3'
$3b_2\rightarrow 4d$	**71,108**		**71,105**			
$3b_2\rightarrow 4d+\nu_3'$	71,747	639	71,686	581		
$3b_2\rightarrow 4d+2\nu_3'$	72,327	1219	72,316	1211		
$2b_1\rightarrow 4d$	**72,452**		**72,432**			
$2b_1\rightarrow 4d+\nu_3'$	–	–	72,963	531		
$2b_1\rightarrow 4d+2\nu_3'$	73,669	1217	73,668	1236		

From the above assignments, the values of excited state vibrational frequencies of CBr symmetric stretching mode (ν_3') in CH_2Br_2 (CD_2Br_2) are estimated to be 753 (766), 731 (761), 694 (549), 615 (601) and 609 (601) cm^{-1} for $3b_2\rightarrow 5p$, $2b_1\rightarrow 5p$, $1a_2\rightarrow 5p$, $3b_2\rightarrow 4d$ and $2b_1\rightarrow 4d$ respectively. The broad and irregular intensity pattern of the vibronic bands may suggest contributions due to perturbations from other states and from hot/sequence bands involving the low frequency ν_4'' (the double-prime denoting the lower electronic state) mode.

3.3.4 VALENCE TRANSITIONS

Valence transitions calculated at the at PBE0/aug-cc-pV5Z level are shown in Table 3.9. The valence-Rydberg mixed type of transitions which are not assigned to any experimentally observed Rydberg state are also included in this table. The first few excited states of CH_2Br_2 occurring in UV region are valence in nature. In the region 4.3–6.7 eV two broad humps centered at 5.58 and 6.32 eV are observed at high (~1 mbar) sample pressure (*cf.* Fig. 3.5). These were earlier reported at 5.562 and 6.323 eV by Causley and Russell [88].

These features are also reported by Ito *et al.* in the solution spectrum of CH_2Br_2 [43]. The lower energy band was tentatively assigned to *n* (b_1)→σ* and *n* (b_2)→σ*, while the higher energy band was proposed to be composed of contributions from *n* (a_1)→σ* and *n* (b_1+b_2)→σ** [88]. Later, on the basis of spin- orbit *ab-initio* investigations, Liu *et al.* [87] assigned these two bands to the 1^1B_2 and 2^1A_1 states respectively.

Table 3.9: Valence transitions for CH_2Br_2 calculated by TDDFT: PBE0/aug-cc-pV5Z

Symmetry	E (eV)	*f*	Λ	Transition	*A*
B1	5.598	0.000	0.56	$2b_1 \rightarrow 5a_1$	0.99
B2	5.671	0.029	0.58	$3b_2 \rightarrow 5a_1$	0.97
A1	6.154	0.001	0.60	$4a_1 \rightarrow 5a_1$	0.96
A1	6.808	0.007	0.47	$3b_2 \rightarrow 4b_2$	0.94
B1	7.304	0.000	0.43	$1a_2 \rightarrow 4b_2$	0.90
B2	7.572	0.159	0.50	$4a_1 \rightarrow 4b_2$	0.90
B2	8.672	0.031	0.33	$4a_1 \rightarrow 5b_2$	0.81
A1	9.881	0.024	0.62	$3a_1 \rightarrow 5a_1$	-0.77
A1	10.038	0.002	0.54	$2b_1 \rightarrow 6b_1$	-0.81
B1	10.918	0.003	0.48	$1b_1 \rightarrow 5a_1$	-0.93
A1	11.254	0.007	0.40	$3a_1 \rightarrow 6a_1$	0.78

f: oscillator strength, Λ: lambda diagnostic, *A*: excitation amplitude

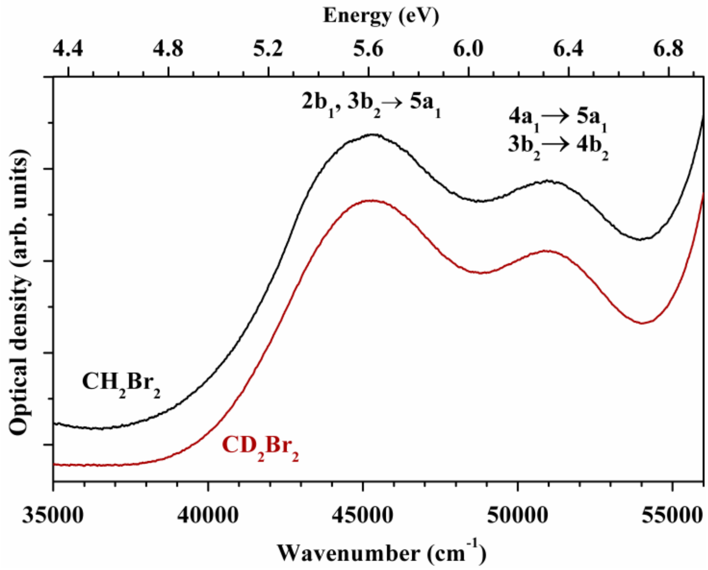

Fig. 3.5: Photoabsorption spectra of CH_2Br_2 and CD_2Br_2 in the region 35,000–56,000 cm^{-1}

It is evident from the present TDDFT calculations (*c.f.* Table 3.9) that the first four vertical excited states lying in 5.59–6.81 eV region with nonzero oscillator strength correspond to the first four excited states 1^1B_1, 1^1B_2, 2^1A_1 and 3^1A_1. These states exhibit valence character as evident from the relatively high values of Λ. Therefore, the lower energy band (5.58 eV) is assigned to the excited states 1^1B_1 and 1^1B_2, in agreement with the assignment of Ito *et al.* [43]. Of these two transitions, the major contribution to intensity is expected from 1^1B_2 owing to higher oscillator strength (~0.03). The higher energy band at 6.32 eV may be assigned to the excited states 2^1A_1 and 3^1A_1 with calculated energies of 6.154 eV and 6.808 eV and oscillator strengths of 0.001 and 0.007 respectively.

The structure of the two broad bands in UV region can be better understood with the help of excited state potential energy curves (PECs). The PECs of the ground state and the first eight singlet excites states at PBE0/aug-cc-pVQZ level of theory with respect to CH_2Br–Br bond length are shown in Figure 3.6. The present results are consistent with those reported earlier by Liu *et al.* [87] using the complete active space second order perturbation theory (CASPT2). As can be seen from Figure 3.6, the PECs for 1^1B_2 and 1^1B_1 are strongly repulsive and 1^1A_2, 2^1A_1 and 3^1A_1 have shallow minima with respect to CH_2Br–Br bond stretch. This is consistent with the large breadth of the experimentally observed features at 5.58 and 6.32 eV.

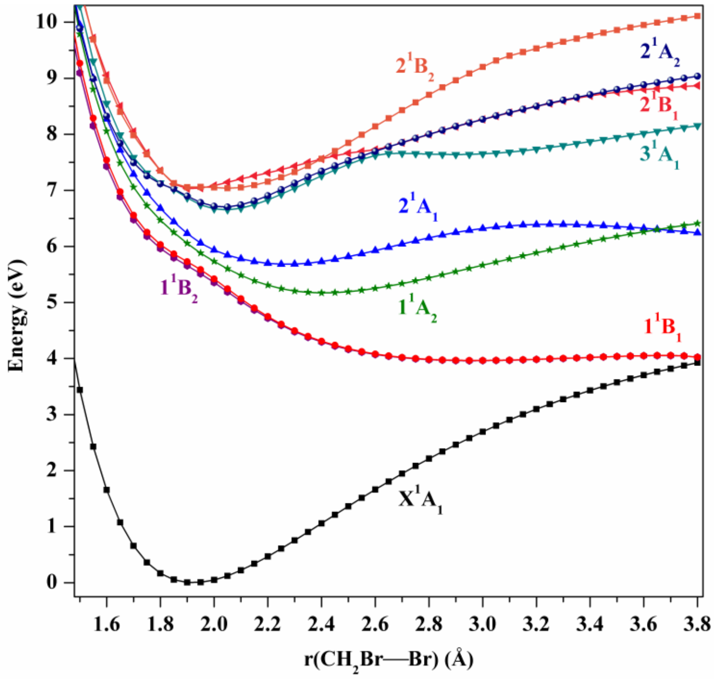

Fig. 3.6: Potential energy curves for the ground and first eight singlet excited states of CH_2Br_2 with respect to CH_2Br–Br bond stretch generated by at PBE0/aug-cc-pVQZ level of theory.

In the energy region 6.8–7.8 eV, four broad absorption features (7.192, 7.378, 7.686 and 7.764 eV) are observed in contrast to three in the earlier study [88]. Of these, the three peaks at 7.192, 7.378 and 7.764 eV are assigned to 5s Rydberg states as discussed in Section 3.3.1. The additional peak observed at 7.686 eV may be assigned to the TDDFT predicted valence transitions $^1B_1$ and $^1B_2$ at 7.304 eV (Λ=0.43) and 7.572 eV (Λ=0.50) respectively; the latter transition with calculated oscillator strength of 0.159 is most likely to be main contributor to the intensity.

In the higher energy region (>7.8 eV), the Rydberg features appear on several broad intensity pedestals. Causley and Russell [88] proposed that this high underlying intensity could be due to the presence of valence states and mentioned three $\sigma \rightarrow \sigma^*$ transitions contributing to the underlying intensity around 9.1, 9.7 and 10.4 eV. A close scrutiny of the spectrum (*c.f.* Fig. 3.3) shows four regions centered at ~8.3, 9.4, 10.3 and 10.7 eV. Interestingly, these energies essentially correspond to the TDDFT predicted transitions that are not assigned to any Rydberg transition (*c.f.* Table 3.9) and most of these have relatively high Λ values indicating valence nature. We propose that these valence transitions are responsible for exhibiting broad underlying intensity in above identified region. For example the excited state $^1B_2$ at 8.672 is likely to contribute to the background intensity around 8.3 eV. Similarly the valence excited state $^1A_1$ at 9.811 eV with oscillator strength of 0.024 appears to be responsible for the underlying intensity around 9.4 eV. Analogous inference can be drawn for the other intensity regions, *i.e.*, 10.3 and 10.7 eV.

CHAPTER 4

ELECTRONIC SPECTROSCOPY OF DICHLOROMETHANE AND DICHLOROMETHANE-d$_2$

4.1 INTRODUCTION

Sources of dichloromethane (CH_2Cl_2) in the atmosphere are largely anthropogenic, arising from industrial and commercial uses [95, 96]. Natural emissions from oceans [97] and biomass burning [98] also contribute CH_2Cl_2 in the atmosphere. Although removal of CH_2Cl_2 in the troposphere is facilitated by reaction with hydroxyl radicals (·OH) limiting the atmospheric lifetime to 5–6 months, ~2% of CH_2Cl_2 emissions do reach the stratosphere [99] where it plays an important role in ozone layer destruction.

Several theoretical and experimental studies on CH_2Cl_2 have been reported over the years with a considerable number on the photodissociation dynamics of CH_2Cl_2 in UV/VUV region [56, 96, 100-112]. Absorption cross-sections of CH_2Cl_2 in the UV region (<50,000 cm^{-1}) at room temperature and lower stratospheric temperatures have been measured by several workers [113-115]. One of the earliest studies of the VUV photo absorption spectrum of CH_2Cl_2 was by Zobel *et al.* [116] who tentatively assigned a few Rydberg transitions along with vibronic features attributed to the ν_3 (CCl s-stretch), ν_2 (CH_2 bend) and ν_4 (CCl_2 bend) modes. Tsubomura *et al.* [117] reported the spectrum of CH_2Cl_2 in the region 1600–1900 Å (52,630–62,500 cm^{-1}) using a hydrogen discharge lamp and assigned the band in the region 50,000–60,000 cm^{-1} to a $n \rightarrow \sigma^*$ transition. Subsequently, Russell *et al.* [118] and Robin [14] assigned a few bands to Rydberg transitions, based on then available IP measurements for CH_2Cl_2. Lee *et al.* [119] reported photoabsorption and fluorescence cross-sections of CH_2Cl_2 in the region 1050–2100 Å (47,600–95,240 cm^{-1}) using synchrotron radiation. They identified six progressions attributed to the ν_3 and ν_5 (CH_2 twist) modes. However they did not assign the corresponding Rydberg series origins. The Rydberg series and vibronic analysis of this molecule reported in literature is incomplete and not well understood.

In this chapter, a consolidated experimental and theoretical investigation of the excited states of CH_2Cl_2 is presented. The VUV photoabsorption spectrum is recorded in the region 50,000–95,000 cm^{-1} (6.2–11.8 eV) using synchrotron radiation. Analysis of the experimental spectrum is supported by density functional theory (DFT) calculations of vibrational frequencies and time dependent DFT (TDDFT) calculations of excited state energies. The assignments are confirmed with the help of the spectrum of CD_2Cl_2 whose VUV spectrum is reported here for the first time.

4.2 METHODOLOGY

4.2.1 EXPERIMENTAL

Photoabsorption studies presented in this chapter are performed using the Photophysics beamline. The samples of CH_2Cl_2 and CD_2Cl_2 are procured from Sigma-Aldrich with stated purity of >99.5%. Several freeze-pump-thaw cycles are performed on the liquid samples to remove volatile impurities before introducing them into the gas cell. Since the absorption cross sections vary significantly over the wide spectral range covered, spectra are recorded at several pressures in the range 10^{-3} to 1 mbar. It is found that the optimum pressure to obtain clear absorption bands the low energy region (<60,000 cm^{-1}) is ~0.3 mbar, while spectral features in higher energy regions (>60,000 cm^{-1}), with higher absorption cross sections are readily obtained at relatively lower sample pressures (0.1–0.001 mbar). Details of the experimental setup and procedure are given in Chapter 1.

4.2.2 COMPUTATIONAL

CH_2Cl_2 in the ground state has C_{2V} symmetry and the coordinate system for the calculations is chosen identical to the choice for CH_2I_2 and CH_2Br_2 given in Chapters 2 and 3 respectively. Ground state geometry optimization and vibrational frequency calculations are performed using MP2 and DFT methods with several different basis sets like 6-311G+(2d,2p) [33], the correlation consistent basis sets cc-pV*n*Z and aug-cc-pV*n*Z (*n* = D, T, Q, 5) [36, 37]. DFT calculations are performed using hybrid exchange correlation functionals B3LYP [25, 65] and PBE0 [64]. As mentioned in Chapter 1, the vibrational frequencies associated with a Rydberg state can be approximated by the ionic ground state frequencies. Hence ground state geometry optimization and vibrational frequency calculations for $CH_2Cl_2^+$ and $CD_2Cl_2^+$ are performed using the unrestricted Hartree-Fock (UHF) reference. Vertical excited states of CH_2Cl_2 are calculated using the TDDFT methodology. Of the basis sets used in the present work, the aug-cc-pV5Z in conjunction with the PBE0 functional is found to yield best overall agreement with experimental values.

4.3 RESULTS AND DISCUSSION

4.3.1 COMPUTATIONAL RESULTS FOR THE GROUND STATES OF NEUTRAL AND IONIC SPECIES

The ground state bond lengths and bond angles, calculated by DFT and MP2 methods using aug-cc-pV5Z basis set, of CH_2Cl_2 and $CH_2Cl_2^+$ are shown in Tables 4.1 and 4.2 respectively. In case of CH_2Cl_2, results obtained using MP2 method agree better than DFT with the experimental values (*cf.* Table 4.1) [120] and also DFT calculation yields better result with the energy functional PBE0 than with B3LYP. The values obtained by PBE0/aug-cc-pV5Z are chosen for further calculations. For the cationic ground state, bond lengths and bond angles are compared with theoretically computed complete active space perturbation theory (CASPT2) values [121] since experimental values are not available in literature (*cf.* Table 4.2). Ground state vibrational frequencies of CH_2Cl_2 and CD_2Cl_2 computed at the PBE0/aug-cc-pV5Z level of theory (*cf.* Table 4.3) are also in good agreement with experimental values wherever available [122, 123]. For the vibrational frequencies of the ground state of $CH_2Cl_2^+$, several computational reports [56, 121, 124] exist (Table 4.3), whereas for $CD_2Cl_2^+$ no earlier experimental or theoretical values are available.

Table 4.1: Optimized bond lengths (Å) and bond angles (deg.) of the ground state of CH_2Cl_2 using DFT and MP2 methods

	r(C–Cl)	r(C–H)	∠(Cl–C–Cl)	∠(H–C–Cl)	∠(H–C–H)
B3LYP/aug-cc-pV5Z	1.781	1.082	113.0	108.0	111.9
PBE0/aug-cc-pV5Z	1.761	1.084	112.9	108.1	111.4
MP2/aug-cc-pV5Z	1.759	1.081	112.2	108.3	111.6
Experimental[a]	1.764	1.085	112.3	–	111.9

[a]Ref. [120]

Table 4.2: Optimized bond lengths (Å) and bond angles (deg.) of the ground state of $CH_2Cl_2^+$ using DFT and MP2 methods

	r(C–Cl)	r(C–H)	∠(Cl–C–Cl)	∠(H–C–Cl)	∠(H–C–H)
B3LYP/aug-cc-pV5Z	1.786	1.083	92.1	111.3	116.7
PBE0/aug-cc-pV5Z	1.766	1.086	90.8	111.7	116.5
MP2/aug-cc-pVQZ	1.765	1.083	89.3	111.8	117.2
CASSCF/ANO-L[a]	1.763	1.080	90.6	–	116.5

[a]Ref. [121]

Table 4.3: Ground state vibrational frequencies (in cm^{-1}) for neutral and ionic dichloromethane calculated at the PBE0/aug-cc-pV5Z level of theory

Mode (symmetry)	**CH_2Cl_2**		**CD_2Cl_2**		**$CH_2Cl_2^+$**				**$CD_2Cl_2^+$**
	This work	**Expt.**[a]	**This work**	**Expt.**[a]	**This work**	**B3LYP/ 6-311G***[b]	**CASSCF /ANO-L**[c]	**B3LYP/6-311+G(d,p)**[c]	**This work**
ν_1: CH sym. stretch (a_1)	3124	2998	2265	2206	3129	2850	3044	3125	2266
ν_2: CH_2 bend (a_1)	1457	1435	1069	1061	1449	1224	1459	1448	1066
ν_3: CCl sym. stretch (a_1)	734	713	705	688	798	682	757	741	763
ν_4: CCl_2 bend (a_1)	286	282	284	279	290	316	294	261	289
ν_5: CH_2 twist (a_2)	1175	1153	836	825	1081	1071			770
ν_6: CH asym. stretch (b_1)	3201	3055	2384	2304	3240	2896			2419
ν_7: CH_2 rock (b_1)	903	899	716	713	953	803			735
ν_8: CH_2 wag (b_2)	1282	1269	968	961	1234	1174			931
ν_9: CCl asym. stretch (b_2)	773	760	742	730	652	540			630

[a]Ref. [123], [b]Ref. [56], [c]Ref. [121]

The ground state electronic configuration of CH_2Cl_2 as predicted by the present DFT calculations is [*core*] $(1a_1)^2(1b_2)^2(2a_1)^2(1b_1)^2(3a_1)^2(2b_2)^2(4a_1)^2(1a_2)^2(3b_2)^2(2b_1)^2$: X^1A_1, where the numbering does not include the core electrons. The ordering of the four HOMOs reported in earlier computational studies [72, 96, 109, 121, 124-130] shows several discrepancies. This may be partly due to ambiguity in b_1 and b_2 symmetries arising from the choice of XZ and YZ planes. With respect to the $4a_1$ and $1a_2$ orbitals, the ordering of MOs predicted by HF [124, 125, 127], CASPT2 [121], complete active space self-consistent field (CASSCF) [121] and MP2 [96] methods is $1a_2 < 4a_1$. On the other hand, the present DFT calculations are in agreement with the results of the outer valence Green's function (OVGF) calculations by Niessen *et al*. [128] and DFT calculations by Bohinc *et al*. [130] which predict $4a_1 < 1a_2$. Since these orbitals are very close in energy, it is not surprising that their ordering is interchanged in different computational methods. Contour plots of the four highest HOMOs and lowest LUMOs are shown in Figure 4.1.

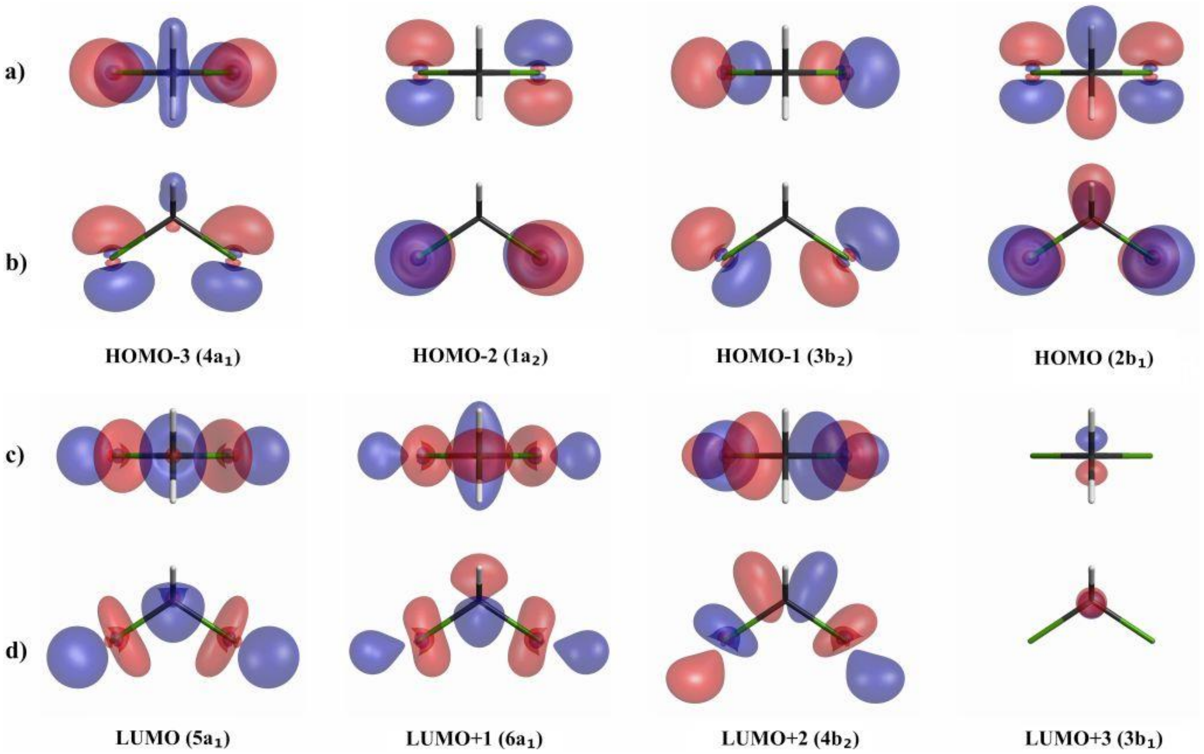

Fig. 4.1: Contour plots of the four HOMOs and four LUMOs of CH_2Cl_2 at PBE0/aug-cc-pV5Z level of theory. HOMOs viewed along (a) Z axis and (b) X axis. LUMOs viewed along (c) Z axis and (d) X axis.

Non-bonding character corresponding to the chlorine lone pair is observed in all the four HOMOs with an additional weak C–H bonding character in $4a_1$ and $2b_1$ orbitals. The first three LUMOs ($5a_1$, $6a_1$ and $4b_2$) may be approximated to non-bonding type with lone pair character on C and Cl, while the fourth one ($3b_1$) shows a lone pair on the central C atom. The energy level diagram corresponding to these orbitals, with a few electronic transitions marked, is shown in Fig. 4.2. Correlation of theoretically predicted transitions with experimental observations is discussed in the next section.

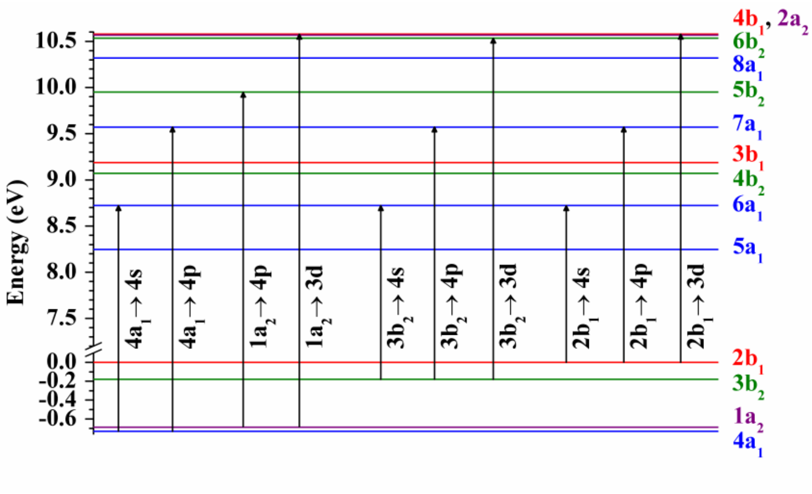

Fig. 4.2: Energy level diagram of CH_2Cl_2 showing first few Rydberg transitions. The zero of the energy scale is fixed at the energy of the HOMO ($2b_1$).

4.3.2 EXPERIMENTALLY OBSERVED RYDBERG SERIES AND CORRELATION WITH COMPUTED VERTICAL EXCITED STATES

The photoabsorption spectra of CH_2Cl_2 and CD_2Cl_2 in the VUV region are shown in Figure 4.3. The first four IPs arising from excitation of an electron from the outermost Cl non-bonding orbitals ($2b_1$, $3b_2$, $1a_2$ and $4a_1$) have been measured at 11.320, 11.357, 12.152 and 12.271 eV respectively by photoelectron spectroscopy [131]. Several Rydberg series of type *ns*, *np* and *nd* (*cf.* Tables 4.4–4.7 and Fig. 4.3) converging to these IPs are identified and assigned using Eq. (1.5). The quantum defect values for these series are expected to be close to atomic chlorine values [94] since the excitations are from chlorine lone pair orbitals.

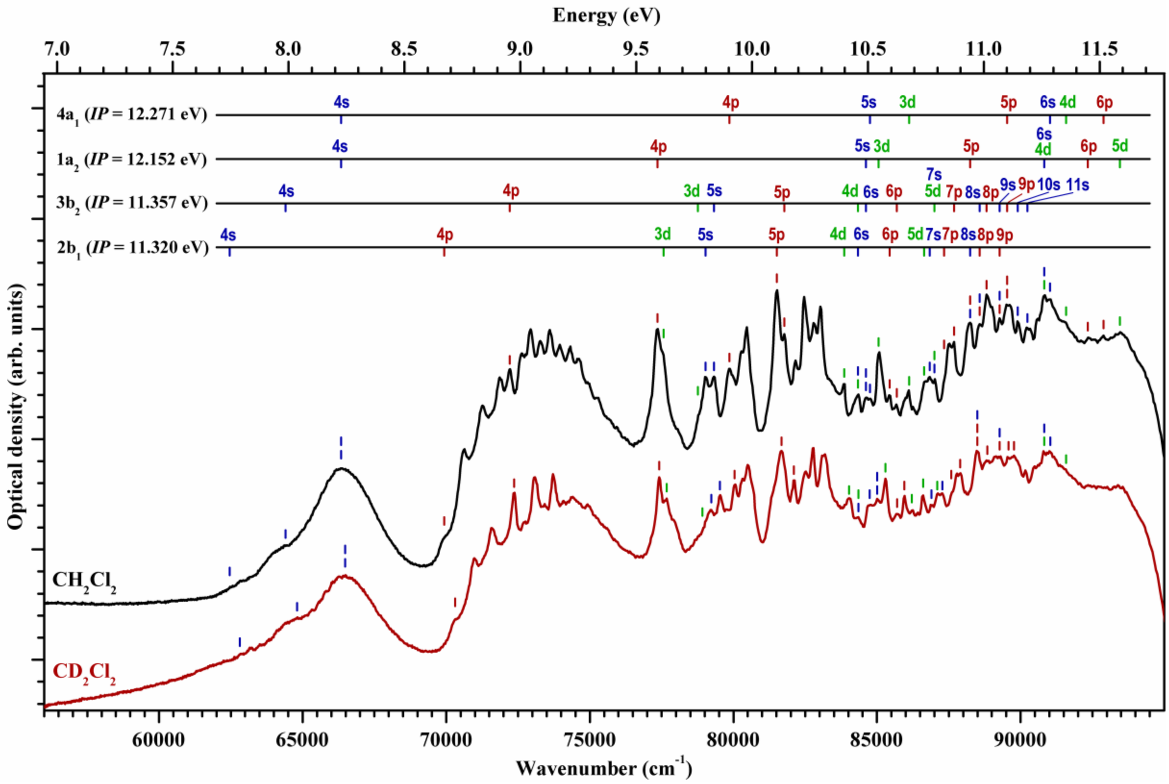

Fig. 4.3: VUV photoabsorption spectra of CH_2Cl_2 and CD_2Cl_2 in the region 55,000–95,000 cm^{-1}. Rydberg series converging to first four IPs are marked.

Table 4.4: Rydberg series converging to IP ($2b_1$) = 11.320 eV observed in the VUV photoabsorption spectrum of dichloromethane

Experimentally observed peak position (eV)[a]			Calculated by TDDFT: PBE0/aug-cc-pV5Z					O–C
Assignment	**CH_2Cl_2**	**CD_2Cl_2**	**E (eV)**	***f***	**Λ**	**Transition**	***A***	
4s	~7.7 (2.06)	~7.7 (2.06)	7.560	0.022	0.39	$2b_1 \rightarrow 6a_1$	0.92	~0.1
5s	9.798 (2.01)	9.823 (1.99)	9.238	<0.001	0.31	$2b_1 \rightarrow 8a_1$	-0.94	0.560
6s	10.457 (2.03)*	10.459 (2.03)*	9.841	0.008	0.20	$2b_1 \rightarrow 10a_1$	-0.55	0.617
7s	10.766 (2.05)*	10.774 (2.01)	10.887	0.043	0.32	$2b_1 \rightarrow 11a_1$	0.98	-0.121
8s	10.941 (2.01)*	–						
4p	8.670 (1.73)	8.717 (1.71)	8.578	0.043	0.29	$2b_1 \rightarrow 7a_1$	-0.97	0.092
			8.283	0.020	0.22	$2b_1 \rightarrow 3b_1$	0.98	0.388
5p	10.106 (1.65)*	10.127 (1.62)	9.815	0.001	0.22	$2b_1 \rightarrow 9a_1$	0.86	0.291
			9.739	0.023	0.28	$2b_1 \rightarrow 4b_1$	-0.56	0.368
6p	10.592 (1.68)	10.625 (1.57)	9.854	0.004	0.24	$2b_1 \rightarrow 10a_1$	0.75	0.738
			9.896	0.011	0.32	$2b_1 \rightarrow 5b_1$	-0.89	0.697
7p	10.828 (1.74)	10.859 (1.57)						
8p	10.982 (1.66)*	10.972 (1.75)*						
9p	11.069 (1.64)*	11.068 (1.65)*						
3d	9.617 (0.17)	9.631 (0.16)	9.759	<0.001	0.27	$2b_1 \rightarrow 4b_1$	-0.73	-0.141
			9.695	0.016	0.22	$2b_1 \rightarrow 2a_2$	0.97	-0.078
4d	10.397 (0.16)	10.419 (0.11)	10.855	0.006	0.31	$2b_1 \rightarrow 6b_1$	-0.54	-0.458
5d	10.742 (0.15)	10.738 (0.17)						

[a] quantum defect value in the parenthesis, *blended line, *f*: oscillator strength, *A*: excitation amplitude, Λ: lambda diagnostic, O–C: difference of observed and calculated energies in eV

Table 4.5: Rydberg series converging to IP ($3b_2$) = 11.357 eV observed in the VUV photoabsorption spectrum of dichloromethane

Experimentally observed peak position (eV)[a]			Calculated by TDDFT: PBE0/aug-cc-pV5Z					O–C
Assignment	**CH_2Cl_2**	**CD_2Cl_2**	**E (eV)**	***f***	**Λ**	**Transition**	***A***	
4s	7.985 (1.99)	8.035 (1.98)	7.804	0.059	0.38	$3b_2 \rightarrow 6a_1$	-0.92	0.181
5s	9.835 (2.01)	9.861 (1.98)	9.449	0.005	0.23	$3b_2 \rightarrow 8a_1$	0.95	0.386
6s	10.491 (2.04)*	10.539 (1.92)*	10.080	0.002	0.26	$3b_2 \rightarrow 10a_1$	0.89	0.411
7s	10.787 (2.11)*	10.820 (1.97)	11.136	0.095	0.37	$3b_2 \rightarrow 11a_1$	0.71	-0.349
8s	10.982 (1.98)*	10.972 (2.06)*						
9s	11.069 (2.14)*	11.068 (2.14)*						
10s	11.146 (1.97)	–						
11s	11.188 (2.03)	–						
4p	8.953 (1.62)	8.972 (1.61)	8.759	0.001	0.27	$3b_2 \rightarrow 7a_1$	0.96	0.195
			9.031	0.018	0.40	$3b_2 \rightarrow 5b_2$	-0.88	-0.078
5p	10.138 (1.66)	10.180 (1.60)	9.994	0.043	0.24	$3b_2 \rightarrow 9a_1$	0.91	0.144
			9.759	<0.001	0.27	$3b_2 \rightarrow 6b_2$	-0.64	0.380
6p	10.624 (1.69)	10.657 (1.59)	10.910	0.012	0.41	$3b_2 \rightarrow 11a_1$	-0.63	-0.286
			10.817	0.002	0.38	$3b_2 \rightarrow 7b_2$	-0.52	-0.194
7p	10.871 (1.71)	10.884 (1.63)*						
8p	11.012 (1.72)	11.014 (1.70)						
9p	11.100 (1.72)*	11.106 (1.64)						
3d	9.765 (0.08)	9.784 (0.06)	9.739	0.023	0.28	$3b_2 \rightarrow 6b_2$	0.64	0.027
			9.841	0.008	0.20	$3b_2 \rightarrow 2a_2$	-0.72	-0.075
4d	10.457 (0.11)*	10.459 (0.11)*	10.855	0.006	0.31	$3b_2 \rightarrow 7b_2$	0.78	-0.398
5d	10.787 (0.11)*	10.798 (0.07)*						

[a] quantum defect value in the parenthesis, *blended line, *f*: oscillator strength, *A*: excitation amplitude, Λ: lambda diagnostic, O–C: difference of observed and calculated energies in eV

Table 4.6: Rydberg series converging to IP ($1a_2$) = 12.152 eV observed in the VUV photoabsorption spectrum of dichloromethane

Experimentally observed peak position (eV)[a]			Calculated by TDDFT: PBE0/aug-cc-pV5Z					O–C
Assignment	**CH_2Cl_2**	**CD_2Cl_2**	**E (eV)**	***f***	**Λ**	**Transition**	***A***	
4s	8.225 (2.14)*	8.243 (2.13)*	8.297	0.000	0.36	$1a_2 \rightarrow 6a_1$	0.92	-0.072
5s	10.491 (2.14)*	10.539 (2.10)*	9.969	0.000	0.24	$1a_2 \rightarrow 8a_1$	0.88	0.522
6s	11.260 (2.09)*	11.260 (2.09)*	10.543	0.000	0.20	$1a_2 \rightarrow 9a_1$	0.64	0.717
4p	9.592 (1.69)	9.598 (1.69)	9.244	0.000	0.27	$1a_2 \rightarrow 7a_1$	0.93	0.348
			8.979	0.020	0.17	$1a_2 \rightarrow 3b_1$	0.97	0.613
5p	10.941 (1.65)*	10.972 (1.60)*	10.396	0.000	0.18	$1a_2 \rightarrow 9a_1$	-0.55	0.545
			10.558	0.005	0.25	$1a_2 \rightarrow 4b_1$	-0.59	0.383
6p	11.449 (1.60)		10.710	0.000	0.22	$1a_2 \rightarrow 10a_1$	0.41	0.738
3d	10.546 (0.09)	10.575 (0.06)	10.398	0.019	0.28	$1a_2 \rightarrow 4b_1$	-0.73	0.148
			10.269	<0.001	0.26	$1a_2 \rightarrow 6b_2$	-0.96	0.276
4d	11.260 (0.09)*	11.260 (0.09)*	10.558	0.005	0.25	$1a_2 \rightarrow 5b_1$	-0.75	0.702
5d	11.588 (0.09)	–						

[a] quantum defect value in the parenthesis, *blended line, *f*: oscillator strength, *A*: excitation amplitude, Λ: lambda diagnostic, O–C: difference of observed and calculated energies in eV

Table 4.7: Rydberg series converging to IP ($4a_1$) = 12.271 eV observed in the VUV photoabsorption spectrum of dichloromethane

Experimentally observed peak position (eV)[a]			Calculated by TDDFT: PBE0/aug-cc-pV5Z					O–C
Assignment	CH_2Cl_2	CD_2Cl_2	E (eV)	*f*	Λ	Transition	*A*	
4s	8.225 (2.17)*	8.243 (2.16)*	8.391	0.010	0.39	$4a_1 \to 6a_1$	0.93	-0.166
5s	10.508 (2.22)	10.508 (2.22)	10.029	0.022	0.30	$4a_1 \to 8a_1$	-0.94	0.479
6s	11.286 (2.28)*	11.287 (2.28)*	10.608	0.006	0.29	$4a_1 \to 10a_1$	0.88	0.678
4p	9.902 (1.60)	9.924 (1.59)	9.320	0.034	0.32	$4a_1 \to 7a_1$	-0.94	0.582
			9.011	0.001	0.14	$4a_1 \to 3b_1$	0.97	0.891
5p	11.100 (1.59)*	11.130 (1.55)*	10.530	0.001	0.24	$4a_1 \to 9a_1$	0.86	0.575
			10.583	0.001	0.22	$4a_1 \to 4b_1$	-0.58	0.522
6p	11.516 (1.75)	–						
3d	10.677 (0.08)*	10.689 (0.07)	10.428	0.018	0.20	$4a_1 \to 4b_1$	-0.78	0.248
			10.334	0.016	0.32	$4a_1 \to 6b_2$	-0.89	0.343
4d	11.356 (0.14)*	11.355 (0.15)	10.583	0.001	0.22	$4a_1 \to 5b_1$	-0.77	0.773

[a] quantum defect value in the parenthesis, *blended line, *f*: oscillator strength, *A*: excitation amplitude, Λ: lambda diagnostic, O–C: difference of observed and calculated energies in eV

Taking the ionic frequencies (*cf.* Table 4.3) to be a reasonable estimate of the excited Rydberg state frequencies, the isotopic shift between CH_2Cl_2 and CD_2Cl_2 is calculated from Eq. (1.7) to be very small (~few cm^{-1}). It is experimentally observed that Rydberg transitions of CD_2Cl_2 are blue shifted by up to ~380 cm^{-1} (0.047 eV). This discrepancy may be due to the fact that the actual excited state vibrational frequencies (and therefore the ZPEs) are different from the ionic ones and vary from state to state. It may be noted that the shift is larger for low lying Rydberg states which may have considerable valence character.

The structureless broad band between 62,000–69,000 cm^{-1} (7.93–8.55 eV) has been assigned by Robin [14] and Lee *et al.* [119] to transitions $2b_2 \to 4s$, $1a_2 \to 4s$, of which the latter is dipole forbidden. In our study, this broad band is assigned to the transitions $2b_1$, $3b_2$, $4a_1 \to 4s$ (*cf.* Fig. 4.3). The underlying intensity in this region could be due to the presence of valence states (*cf.* section 4.4). The *ns* Rydberg series members are identified up to n = 8, 11, 6 and 6 corresponding to excitation from $2b_1$, $3b_2$, $1a_2$ and $4a_1$ respectively, in both CH_2Cl_2 and CD_2Cl_2. Since s orbitals have a_1 symmetry, transitions of the type $1a_2 \to ns$ are dipole forbidden, therefore they are not expected to appear in the spectrum. However, the energies at which they would occur, *viz*. 8.225, 10.491 and 11.260 eV (*cf.* Table 4.6 and Fig. 4.3), it can be noted that fairly intense bands do appear. The observed intensity at these energies corresponding to the $1a_2 \rightarrow 4s$, 5s and 6s excitations may be attributed to blending of these features with other Rydberg transitions, *viz*., $4a_1 \rightarrow 4s$, $3b_2 \rightarrow 6s$ and $1a_2 \rightarrow 4d$ respectively (*cf.* Tables 4.7, 4.5 and 4.6). Alternatively the IP at 12.152 eV belongs to $4a_1$ (as predicted by the MP2 calculations; in the present work as well as Ref. [96]) and these bands are actually due to the transitions $4a_1 \rightarrow 4s$, 5s and 6s. However, this would mean that the 4s, 5s and 6s states at 8.225, 10.508 and 11.286 eV are assigned to $1a_2 \rightarrow 4s$, 5s and 6s respectively. While the peak at 8.225 eV could be equally assigned to either $4a_1 \rightarrow 4s$ or $1a_2 \rightarrow 4s$, the assignment of the 10.508 and 11.286 eV to forbidden transitions $1a_2 \rightarrow 5s$ and 6s is not justified, as the observed intensity at these energies cannot be explained by blending with other valence/Rydberg transitions. Therefore it is concluded that the orbital energy ordering predicted by the present DFT calculation ($2b_1 > 3b_2 > 1a_2 > 4a_1$) is consistent with the experimental observations.

The *np* Rydberg series corresponding to excitation from $2b_1$ and $3b_2$ are observed up to *n*=9 whereas fewer members of these series (up to *n*=6) are observed arising from $1a_2$ and $4a_1$. Three members of the *nd* series (*n*=3, 4, 5) are observed for excitations arising from $2b_1$, $3b_2$ and $1a_2$, while only two members (*n*=3, 4) are observed for excitation from $4a_1$. It may be seen from Fig. 4.3 that relatively low lying Rydberg transitions (<10.41 eV) are quite distinct, but as one goes to higher members (>10.41 eV), bands may be severely overlapped. The higher members of the Rydberg series are expected to be weaker owing to the n^{-3} dependence of intensity. Relative higher intensity observed for higher Rydberg series (*cf.* Fig. 4.3) is probably due to underlying valence transitions and/or overlap with vibronic transitions.

TDDFT predicted transition energies calculated at the PBE0/aug-cc-pV5Z level, corresponding to the observed Rydberg series, are tabulated alongside with the experimental values for both CH_2Cl_2 and CD_2Cl_2 in Tables 4.4–4.7. Here, assignment of calculated electronic states to experimentally observed Rydberg (and valence) transitions is essentially based on the symmetries of initial and final MOs involved in the transition. For the *ns* series, the final MOs is expected to be of a_1 symmetry. For the *np* and *nd* series, the symmetries of the final orbitals are expected to be the same within a given series that converges to a particular IP. In this manner, all experimentally observed transitions are correlated with theoretically calculated energies. Excitation amplitudes (*A*) for the major orbital excitations (*A*>0.4) contributing to each transition, oscillator strengths (*f*) and lambda diagnostic (Λ) values are also tabulated. It may be mentioned that correlation of calculated oscillator strengths with experimentally observed intensities is possible to some extent in lower energy regions, but is difficult in higher energy regions due to increased blending of transitions. The accuracy of calculated excited state energies is expected to be very good up to 1 eV higher than the energy of the HOMO [31], *i.e.* ~9.7 eV in the present case. For higher excitation energies (>9.7 eV), the accuracy of the calculation decreases, as is evident from the larger differences between observed and calculated values (*cf.* Tables 4.4–7). It is also seen that low lying excited states result essentially from single orbital excitations whereas mixing of two or more molecular orbital excitations with comparable amplitude becomes more common for high lying excited states (*cf.* Tables 4.4–4.7).

In the case of *np* and *nd* series, more than one set of calculated transitions can be associated with a given series. For example, theoretically predicted transitions corresponding to $2b_1 \rightarrow 7a_1$, $9a_1$…. as well as $2b_1 \rightarrow 3b_1$, $4b_1$… can be assigned to the experimentally observed series $2b_1 \rightarrow np$ (*cf.* Table 4.4). Similarly, the $2b_1 \rightarrow 3d$ transition (*cf.* Table 4.4) can be correlated with the theoretically predicted transitions $2b_1 \rightarrow 4b_1$ as well as $2b_1 \rightarrow 2a_2$. Although, in principle, observation of more than one series of a given angular momentum is possible, they are not distinguishable in the present experiment. Therefore, both sets of transitions which may be assigned to the *np*/*nd* series are included in Tables 4.4–7. It should be noted that the symmetries of the final orbital predicted by the TDDFT calculation is a_1, both for the *ns* series as well as one of the two *np* series. Likewise, the symmetry of the final orbital in the second set of predicted *np* series is same as one of the *nd* series. The first set (corresponding to the upper entries in Table 4.6) of theoretically predicted $1a_2 \rightarrow np$ (a_1) series is therefore dipole forbidden. The observed intensities of these bands in the experimental spectrum may be attributed to blending with other Rydberg transitions or to the second set of predicted transitions (lower entries in Table 4.6). A special mention must be made to the $1a_2 \rightarrow 4p$ transition at 9.592 eV which is not blended with any other Rydberg transition. The high intensity of this band may be attributed to the alternate theoretically predicted transition $1a_2 \rightarrow 3b_1$ with oscillator strength 0.02 or a nearby valence transition as discussed in 4.3.4.

4.3.3 VIBRONIC ASSIGNMENTS

In the region 69,000–92,000 cm^{-1} (8.55–11.41 eV), several spectral features may be attributed to vibronic bands accompanying the Rydberg transitions as listed in Table 4.8 and marked appropriately in Figure 4.4. In the 69,900–76,800 cm^{-1} (8.67–9.52 eV) region (*cf.* Fig. 4.4), the Rydberg series origins $2b_1 \rightarrow 4p$ and $3b_2 \rightarrow 4p$, at 69,930 and 72,213 cm^{-1} respectively show extensive progressions of the ν_3' mode (*cf.* Table 4.8), where the prime denotes the vibrational mode in the excited electronic state. These vibrational features were also observed by Lee and Suto and tentatively assigned to progressions of the ν_3' mode without specifying the associated Rydberg state origins. In the present study, the series are clear and free from blending and the Rydberg series origins to which the progressions belong are unambiguously identified. From the long progressions observed, the average value of ν_3' is found to be 668±52 (625±55) cm^{-1} and 700±70 (648±62) cm^{-1} for the transitions $2b_1 \rightarrow 4p$ and $3b_2 \rightarrow 4p$ of

CH_2Cl_2 (CD_2Cl_2) respectively. These values are quite close to the neutral ground state fundamental ν_3''. This indicates that the geometry of the molecule in these low lying Rydberg states does not change appreciably from the ground state. Moreover, within the experimental uncertainty, a measurable isotope shift is not seen for the ν_3' mode in these Rydberg states.

Table 4.8: Vibronic bands (cm^{-1}) observed in the VUV photoabsorption spectrum of dichloromethane

This work			**Previous study for CH_2Cl_2[a]**	
Assignment	**CH_2Cl_2**	**CD_2Cl_2**	**Assignment[b]**	**cm^{-1}**
$2b_1\rightarrow4p$	**69,930**	**70,311**	**X**	**69,930**
$2b_1\rightarrow4p+\nu_3'$	70,648	70,963	$X+\nu_3'$	70,626
$2b_1\rightarrow4p+2\nu_3'$	71,266	71,583	$X+2\nu_3'$	71,270
$2b_1\rightarrow4p+3\nu_3'$	71,870	—	$X+3\nu_3'$	71,890
$2b_1\rightarrow4p+4\nu_3'$	72,627	72,737	$X+4\nu_3'$	72,611
$2b_1\rightarrow4p+5\nu_3'$	73,267	73,421	$X+5\nu_3'$	73,287
$2b_1\rightarrow4p+6\nu_3'$	73,946	74,073	$X+6\nu_3'$	73,948
$2b_1\rightarrow4p+7\nu_3'$	74,586	74,650	$X+7\nu_3'$	74,644
$2b_1\rightarrow4p+8\nu_3'$	75,227	75,194	$X+8\nu_3'$	75,324
$2b_1\rightarrow4p+9\nu_3'$	75,945	75,889	$X+9\nu_3'$	75,999
$3b_2\rightarrow4p$	**72,213**	**72,363**	**Y**	**72,239**
$3b_2\rightarrow4p+\nu_3'$	72,937	73,079	$Y+\nu_3'$	72,945
$3b_2\rightarrow4p+2\nu_3'$	73,616	73,720	$Y+2\nu_3'$	73,632
$3b_2\rightarrow4p+3\nu_3'$	74,334	74,372	$Y+3\nu_3'$	74,333
$3b_2\rightarrow4p+4\nu_3'$	74,928	74,921	$Y+4\nu_3'$	75,024
$3b_2\rightarrow4p+5\nu_3'$	75,712	75,601	$Y+5\nu_3'$	75,706
$1a_2\rightarrow4p$	**77,361**	**77,417**		
$1a_2\rightarrow4p+\nu_3'$	78,040	78,004		
$2b_1\rightarrow5s$	**79,030**	**79,225**		
$2b_1\rightarrow5s+\nu_8'$	80,272	80,313		
$2b_1\rightarrow5s+2\nu_8'$	81,513*	81,284*		
$2b_1\rightarrow5s+3\nu_8'$	82,794*	82,515		
$2b_1\rightarrow5s+\nu_2'$	80,465	80,495		
$2b_1\rightarrow5s+\nu_1'$	82,173	81,284*		
$2b_1\rightarrow5p$	**81,513**	**81,681**		
$2b_1\rightarrow5p+\nu_8'$	82,794*	82,771*		
$3b_2\rightarrow5p$	**81,770**	**82,106**		
$3b_2\rightarrow5p+\nu_3'$	82,464*	82,771*		
$3b_2\rightarrow5p+\nu_8'$	83,027	83,134		
$2b_1\rightarrow6p$	**85,433**	**85,699**	**Z**	**85,609**
$2b_1\rightarrow6p+\nu_3'$	86,112*	86,415	$Z+\nu_3'$	86,289
$2b_1\rightarrow6p+2\nu_3'$	86,830*	87,093*	$Z+2\nu_3'$	87,009
$2b_1\rightarrow6p+3\nu_3'$	87,509	87,783*	$Z+3\nu_3'$	87,712
$2b_1\rightarrow6p+4\nu_3'$	88,246*	88,493*	$Z+4\nu_3'$	88,370
$2b_1\rightarrow6p+5\nu_3'$	89,002	89,118	$Z+5\nu_3'$	89,055
$2b_1\rightarrow6p+6\nu_3'$	89,631	89,770*	$Z+6\nu_3'$	89,767
$2b_1\rightarrow6p+7\nu_3'$	90,331	90,497	$Z+7\nu_3'$	90,424
$2b_1\rightarrow6p+8\nu_3'$	91,024	91,035*	$Z+8\nu_3'$	91,066
$2b_1\rightarrow6p+9\nu_3'$	91,590*	—	—	—

[a]Ref. [119]; [b]The transition A was assigned to ($2b_2,1a_2\rightarrow4p$) in Ref. [14], Origins of Rydberg transition Y, Z were unassigned.

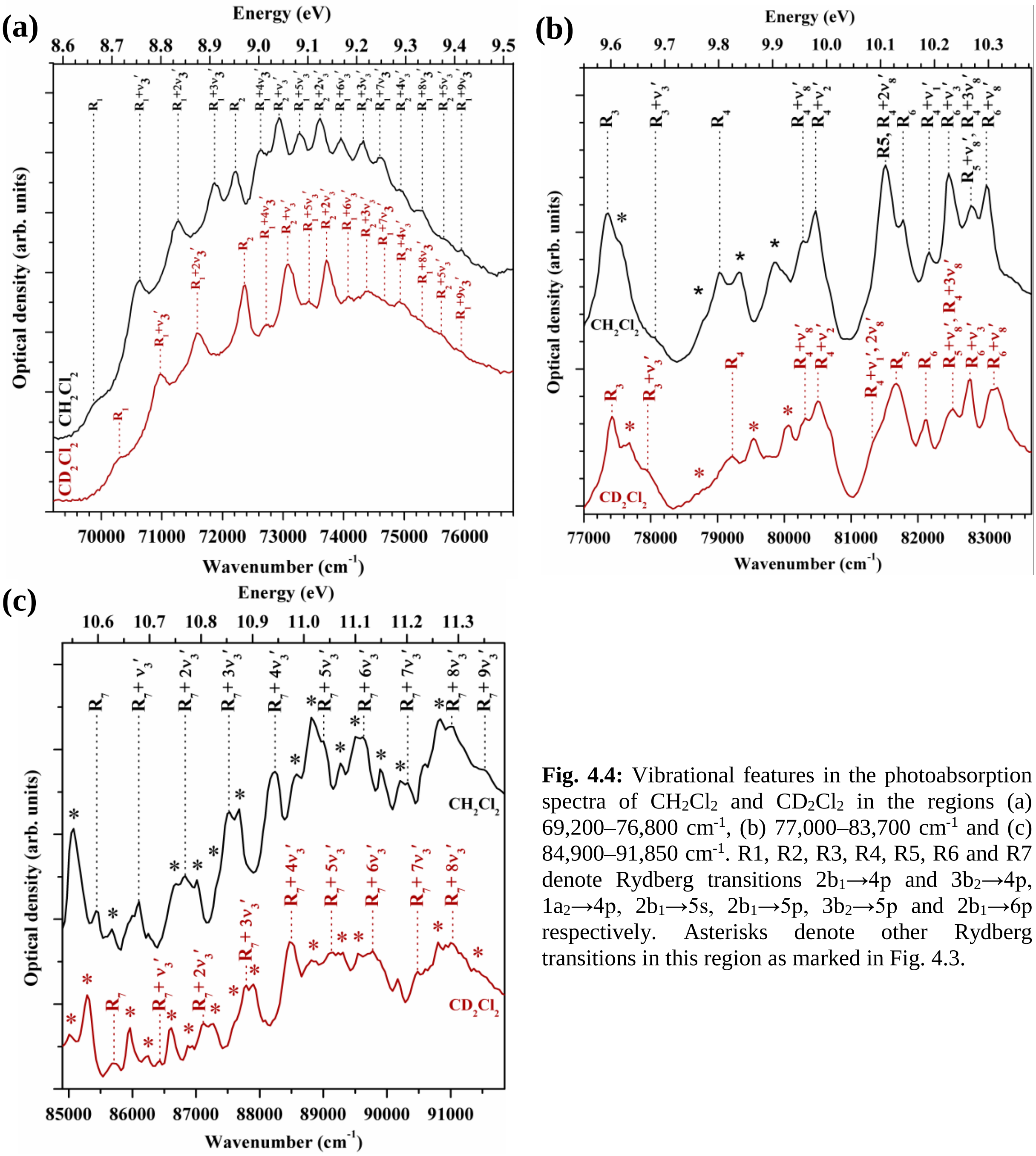

Fig. 4.4: Vibrational features in the photoabsorption spectra of CH_2Cl_2 and CD_2Cl_2 in the regions (a) 69,200–76,800 cm^{-1}, (b) 77,000–83,700 cm^{-1} and (c) 84,900–91,850 cm^{-1}. R1, R2, R3, R4, R5, R6 and R7 denote Rydberg transitions $2b_1\rightarrow4p$ and $3b_2\rightarrow4p$, $1a_2\rightarrow4p$, $2b_1\rightarrow5s$, $2b_1\rightarrow5p$, $3b_2\rightarrow5p$ and $2b_1\rightarrow6p$ respectively. Asterisks denote other Rydberg transitions in this region as marked in Fig. 4.3.

In the region >77,000 cm^{-1} (*cf.* Fig.4.4), the $1a_2\rightarrow4p$ transition at 77,361 cm^{-1} is accompanied by a single excitation of the ν_3' mode. In the 80,200–83,500 cm^{-1} region, vibronic structures associated with the $2b_1\rightarrow5s$, 5p and $3b_2\rightarrow5p$ Rydberg series are observed. The ν_8' mode is excited along with all three Rydberg transitions. Additionally, the ν_1', ν_2' modes are excited along with $2b_1\rightarrow5s$, and the ν_3' mode appears with $3b_2\rightarrow5p$. These bands appear at expected positions in the spectrum of CD_2Cl_2 thus confirming the validity of the assignments. It may be noted that due to the relatively low frequency of ν_1' in CD_2Cl_2, the $2b_1 \rightarrow 5s+\nu_1'$ transition observed in CH_2Cl_2 as a distinct peak at 82,173 cm^{-1} is shifted considerably to the lower energy side (81,284 cm^{-1}) where it is partly merged into the rising part of the very strong Rydberg transition peaking at 81,681 cm^{-1} and appears as a shoulder (*cf*. Fig. 4.4, Table 4.8). Experimentally observed frquencies of the ν_1', ν_2' and ν_8' modes in the $2b_1 \rightarrow 5s$ state are 3143 (2189), 1435 (1270), 1246 (1093) cm^{-1} respectively for CH_2Cl_2 (CD_2Cl_2). Similarly, in the $3b_2 \rightarrow 5p$ Rydberg state, observed frequencies of the ν_3' and ν_8' modes are 694 (665) and 1257 (1028) cm^{-1} respectively for CH_2Cl_2 (CD_2Cl_2).

In the 85,400–91,600 cm^{-1} region, a long progression of ν_3' is observed and is assigned to the $2b_1 \rightarrow 6p$ Rydberg series (*cf.* Fig. 4.4). This series was also reported by Lee and Suto but the origin was not specified by them. In this series, a few of the lines are blended with higher Rydberg series origins. The present assignments are verified by the observation of corresponding peaks in the spectrum of CD_2Cl_2. The average value of ν_3' for the $2b_1 \rightarrow 6p$ Rydberg series is found to be 684±52 (666±63) for CH_2Cl_2 (CD_2Cl_2).

It can be seen that, while the frequencies of ν_1' and ν_2' are close to ionic frequencies, the frequency of the ν_3' mode accompanying the $3b_2 \rightarrow 4p$, 5p and $2b_1 \rightarrow 4p$, 5s transitions is somewhat reduced from both ground state and ionic values. The frequency of the ν_8' mode observed in the $2b_1 \rightarrow 5s$, $2b_1 \rightarrow 5p$ and $3b_2 \rightarrow 5p$ states for CH_2Cl_2 is close to the calculated ionic frequency whereas in the case of CD_2Cl_2, it is observed to be somewhat higher than the predicted ionic value. It should be mentioned that Lee and Suto assigned three progressions to the ν_5' mode in the region 78,800–83,200 cm^{-1}, however there are a few discrepancies in their assignments. In the series starting from 78,871 cm^{-1}, of the four members assigned to ν_5', the vibrational interval for the second band (879 cm^{-1}) deviates from the others (~1050 cm^{-1}) and in the series starting from 79,145 cm^{-1}, the successive differences between bands varies considerably (869–1241 cm^{-1}). In the present study, while trying to fit the bands in this region into progressions of ν_5', it is found that almost all the bands are blended with Rydberg transitions and several bands are not observed at expected positions in the spectrum of CD_2Cl_2. Moreover, if the assignment to a ν_5' progression is correct, an isotope shift of ~300 cm^{-1} should be seen, which is contrary to the experimental observations. This leads to the conclusion that the vibronic and Rydberg series assignments for these bands in the present work are more favorable/justified. It may be noted that, the comparative study of CH_2Cl_2 and CD_2Cl_2 has helped greatly in validating the vibronic assignments, which is an important aspect of the present work.

4.3.4 VALENCE TRANSITIONS

The energy region 6.2–7.5 eV (*cf*. Fig. 4.5) corresponds to the first few excited states of CH_2Cl_2 that are valence in nature. Several earlier studies [101-103, 107] have reported that the molecule dissociates primarily by rupture of the C–Cl bond upon 193 nm photon absorption. Valence transitions calculated at the at PBE0/aug-cc-pV5Z level are shown in Table 4.9. Also included in this table are valence-Rydberg mixed type of transitions which are not assigned to any experimentally observed Rydberg state.

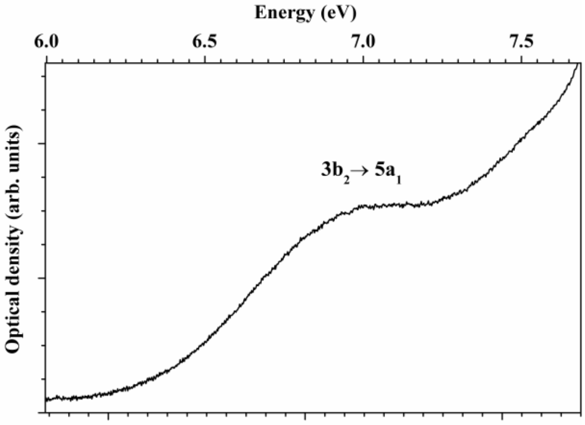

Fig. 4.5: Photoabsorption spectrum of CH_2Cl_2 in the region 48,500–62,000 cm^{-1}

Table 4.9: Valence transitions of CH_2Cl_2 calculated by TDDFT: PBE0/aug-cc-pV5Z

Energy (eV)[a]	***f*** [a]	**Λ**	**Symmetry.**	**Transition**	***A***
6.694	<0.001	0.50	B_1	$2b_1 \rightarrow 5a_1$	0.93
(6.71)	(0.007)				
6.998	0.014	0.49	B_2	$3b_2 \rightarrow 5a_1$	-0.94
(6.80)	(0.022)				
7.472	0.003	0.51	A_1	$4a_1 \rightarrow 5a_1$	-0.91
7.931	0.010	0.41	A_1	$3b_2 \rightarrow 4b_2$	-0.88
8.467	0.013	0.38	B_1	$1a_2 \rightarrow 4b_2$	0.92
8.719	0.138	0.43	B_2	$4a_1 \rightarrow 4b_2$	-0.88
9.031	0.018	0.40	A_1	$3b_2 \rightarrow 5b_2$	-0.88
9.463	0.028	0.36	B_1	$1a_2 \rightarrow 5b_2$	0.81
9.528	0.062	0.41	B_2	$4a_1 \rightarrow 5b_2$	0.87

[a]Values from Ref. [109] in the parenthesis, *f*: oscillator strength, *A*: excitation amplitude, Λ: lambda diagnostic

According to the present calculations, the broad peak between 6.20 and 7.45 eV may be attributed to the predicted transitions $2b_1$, $3b_2$, $1a_2$, $4a_1 \rightarrow 5a_1$ (LUMO), of which the transition $1a_2 \rightarrow 5a_1$ is dipole forbidden. As can be seen from Table 4.9, the transitions originating from $2b_1$ and $4a_1$ have very low oscillator strength (0.0003 and 0.003), therefore the major contribution to the observed band intensity is due to $3b_2 \rightarrow 5a_1$ having an oscillator strength of 0.014. The structure of the absorption band can be better understood by studying the excited state potential energy curves (PECs). PECs as a function of the CH_2Cl–Cl bond distance for the first eight singlet excited states are shown in Figure 4.6.

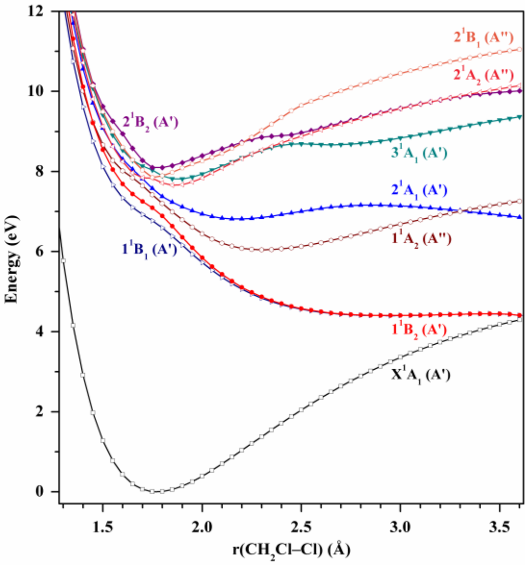

Fig. 4.6: Potential energy curves for the ground and first eight singlet excited states of CH_2Cl_2 with respect to change in CH_2Cl–Cl bond length generated at PBE0/6-311G+(2d,2p) level of theory.

The PECs for the first two singlet excited states agree well with those reported by Xiao *et al*. [109] using the CASSCF method. In Fig.4.6, the 1^1B_1 and 1^1B_2 states are strongly repulsive and the 2^1A_1 state has a shallow minimum with respect to CH_2Cl–Cl bond stretch. This is in line with the observation of a very broad absorption band between 6.20 and 7.45 eV. Further, transition to a repulsive state typically results in dissociation of the molecule, reaffirming the conclusion that the 193 nm photodissociation of CH_2Cl_2 is essentially due to excitation to the 1^1B_1, 1^1B_2 and 2^1A_1 states [109].

To the higher energy side (>7.45 eV), although most of the peaks are satisfactorily assigned to Rydberg series, there are regions where there is a broad underlying intensity which is not explained. For example, in the region of the 4s Rydberg states (7.93–8.55 eV), the intensity and width of the observed band cannot be accounted for by the 4s Rydberg states alone. TDDFT calculations (*cf.* Table 4.9) predict two valence transitions in this region, *viz.* $3b_2$, $1a_2 \rightarrow 4b_2$ at 7.931 and 8.467 eV respectively, with almost equal oscillator strength, which can contribute to the underlying intensity in this region. From the PEC (*cf.* Fig. 4.6), it can be seen that the ($3b_2 \rightarrow 4b_2$) 2^1A_1 state has a shallow minimum which may be responsible for the broadness of this band. Similarly, in the region between 8.55–9.48 eV, Rydberg and vibronic transitions seem to be riding on underlying intensity pedestals. The three valence transitions, *viz*,. $4a_1 \rightarrow 4b_2$ and $3b_2$, $1a_2 \rightarrow 5b_2$ at 8.719, 9.031 and 9.463 eV respectively (*cf.* Table 4.9) may be contributing to this intensity. Of these, the $4a_1 \rightarrow 4b_2$ has a larger contribution due to its higher oscillator strength (0.14) compared to the other two (0.02 and 0.03). The observed band at 9.592 eV has a much higher intensity than expected from a dipole forbidden Rydberg transition ($1a_2 \rightarrow 4p$). The valence transition $4a_1 \rightarrow 5b_2$ predicted at 9.528 eV with a relatively high oscillator strength of 0.62 could account for the intensity of this transition. Such underlying intensity pedestals are also seen in higher energy regions and may be attributed to valence and valence-Rydberg mixed transitions with high oscillator strengths.

CHAPTER 5

ELECTRONIC SPECTROSCOPY OF DIMETHYL SULPHOXIDE AND DIMETHYL SULPHOXIDE-d_6

5.1 INTRODUCTION

Dimethyl sulphoxide (DMSO) is the simplest member of the sulphoxide family of compounds. It is a versatile solvent widely used in industrial applications and is a natural product of biodegradation of organo-sulphur compounds in the biosphere [132]. It is postulated to be an intermediate in the atmospheric oxidation of alkyl sulphides to sulphur dioxide, and it is the sulphur analogue of the well studied acetone molecule [133]. The electronic structure of DMSO and its photodissociation dynamics have elicited considerable interest due to its important role in the atmospheric sulphur balance [134]. Understanding of the excited states of DMSO is of crucial importance in understanding photochemical reactions involving this compound.

The electronically excited states of DMSO have been studied by a variety of experimental and theoretical methods [132, 134-138]. The earliest study of the electronic absorption spectrum of DMSO was by Gollnick and Stracke [135]. Subsequently, Sze *et al.* [136] carried out photoabsorption and electron energy loss studies and also reported some theoretical calculations. The photoabsorption spectrum of DMSO in the region from 30,000 to 87,000 cm^{-1} using synchrotron radiation has been reported recently by Drage *et al*. [132]. However, there are several discrepancies in their spectral assignments. Moreover, Rydberg series and vibronic analysis of the observed transitions reported in literature [132, 136] is incomplete.

The motivation behind the present work is to sort out some of these issues and obtain a complete set of Rydberg series and vibronic assignments for the electronic absorption spectrum of DMSO. Isotopic substitution is a valuable tool for confirmation of vibrational assignments [17] and in this context, it is of interest to examine the VUV photoabsorption spectrum of the deuterated isotopologue DSMO-d_6, on which there are no published reports to the best of our knowledge. In the present work, photoabsorption spectra of DMSO and DMSO-d_6 are studied in the region 35,000–80,000 cm^{-1} (~4.3–9.9 eV) using synchrotron radiation. Details of the experiments performed and the analysis of the spectra carried out with the help of quantum chemical calculations are presented in this chapter. In the course of the study some interesting results pertaining to the photodissociation of DMSO upon VUV excitation are obtained which are also discussed.

5.2 METHODOLOGY

5.2.1 EXPERIMENTAL

Photoabsorption studies are performed using the Photophysics beamline at an average spectral resolution of 1.5 Å (~4 meV at 4 eV and ~9 meV at 9 eV) and the HRVUV beamline at an average resolution of 0.5 Å (1.3 meV at 4 eV and 3 meV at 9 eV). DMSO and DMSO-d_6 of stated purities 99 % and supplied by M/s. Sigma Aldrich and Heavy water board, Baroda, India respectively are used in the present study. Samples are subjected to several freeze-pump-thaw cycles before introduction into the cells. The absorption cells are evacuated to a base pressure of ~10^{-6} mbar prior to sample introduction. In the present studies, pressures are varied from 0.001 mbar to 1 mbar, in order to take care of the vastly varying absorption cross sections in the VUV region. Wavelength calibration is done using xenon atomic absorption lines (in the region >62,500 cm^{-1}) or absorption bands of molecules like O_2 and SO_2 (in the region 48,000–62,500 cm^{-1}). Details of the beamlines and experimental stations are described in Chapter 1.

5.2.2 COMPUTATIONAL

Ground state geometry optimization and vibrational frequency calculations for DMSO and DMSO-d_6 are performed using DFT as well as MP2 methods with several different basis sets like 6-311G+(3d), the correlation consistent basis sets cc-pV*n*Z (*n* = D, T, Q, 5) [139, 140]. DFT calculations are performed using hybrid exchange correlation functionals B3LYP [141, 142] and PBE0 [143]. The ground state geometry optimization and vibrational frequency calculations for the ionic species $DMSO^+$ and DMSO-d_6^+ are performed using the unrestricted Hartree-Fock (UHF) reference. Vertical excited states of DMSO are calculated using the TDDFT method.

5.3 RESULTS AND DISCUSSION

5.3.1 COMPUTATIONAL RESULTS

DMSO belongs to the C_s point group, with the mirror plane passing through the S=O bond. Its ground state configuration is given by [*core*] $(7a')^2(8a')^2(3a'')^2(9a')^2(10a')^2(11a')^2$ $(4a'')^2(5a'')^2(12a')^2(6a'')^2(13a')^2(7a'')^2(14a')^2$: X^1A'. Contour plots of the two highest occupied MOs and four lowest occupied MOs are shown in Figure 5.1. The simple MO picture in the analogous acetone molecule where the HOMO is a lone pair localized on the oxygen atom is disturbed in DMSO, as the sulphur d orbitals also contribute to the MOs and considerable delocalization is seen [135].

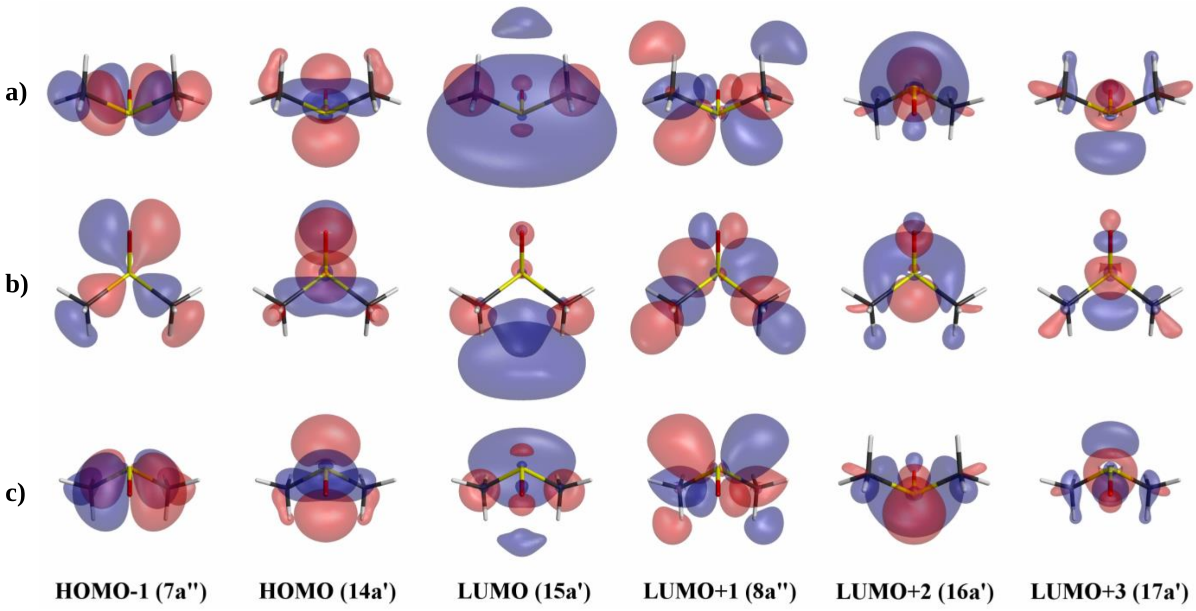

Fig. 5.1: Contour plots of the two HOMOs and four LUMOs of DMSO from different directions (a), (b) and (c) at B3LYP/cc-pV5Z level of theory

Results of ground state geometry optimization for the neutral and ionized molecule, carried out using DFT (B3LYP and PBE0) as well as MP2 methods, are listed in Tables 5.1 and 5.2. The best agreement with experimental values [144, 145] is obtained at the B3LYP/cc-pV5Z level of theory, for which ground state vibrational frequencies for both neutral and ionized species are listed in Table 5.3. Ionic frequencies are calculated in the anticipation that these would help in the assignment of vibronic bands associated with Rydberg transitions. Note here that there exists no experimental data on vibrational frequencies of ionic DMSO-h_6 (d_6). The predicted frequencies for neutral and ionic DMSO-h_6 (d_6) are found to be close to each other. Vertical excited states of DMSO are calculated at the B3LYP/cc-pV5Z and CAMB3LYP/6-311G+(3d) levels of theory, of which the latter are tabulated in Table 5.4 for convenience of comparison with recent theoretical work [134].

Table 5.1: Optimized bond lengths (Å) and bond angles (deg.) of the ground state of DMSO using DFT and MP2 methods

	r(S–O)	**r(S–C)**	**∠(O–S–C)**	**∠(C–S–C)**
B3LYP/cc-pVQZ	1.486	1.819	106.8	96.5
B3LYP/cc-pV5Z	1.486	1.818	106.8	96.6
PBE0/cc-pVQZ	1.478	1.798	106.8	96.4
PBE0/cc-pV5Z	1.478	1.798	106.9	96.5
MP2/cc-pVQZ	1.484	1.793	106.7	95.7
Experimental[a]	1.485	1.808	106.6	96.6

[a] Ref. [144]

Table 5.2: Optimized bond lengths (Å) and bond angles (deg.) of the ground state of DMSO$^+$ using DFT and MP2 methods

	r(S–O)	**r(S–C)**	**∠(O–S–C)**	**∠(C–S–C)**
B3LYP/cc-pVQZ	1.466	1.795	112.5	109.3
B3LYP/cc-pV5Z	1.465	1.795	112.6	109.4
PBE0/cc-pVQZ	1.456	1.771	113.0	109.4
PBE0/cc-pV5Z	1.454	1.770	113.1	109.5
MP2/cc-pVQZ	1.420	1.760	116.2	109.8

Table 5.3: Vibrational frequencies (cm^{-1}) of dimethyl sulphoxide calculated at the B3LYP/cc-pV5Z level of theory

Mode (symmetry)	**Neutral**				**Ionic**	
	DMSO		**DMSO-d_6**		**DMSO$^+$**	**DMSO-d_6^+**
	This work	**Experimental[a]**	**This work**	**Experimental[a]**	**This work**	**This work**
ν_1 (A')	3138	3010	2328	2253	3151	2342
ν_2 (A')	3128	3010	2321	2253	3139	2330
ν_3 (A')	3033	2933	2170	2132	3035	2169
ν_4 (A')	1478	1455	1109	1055	1447	1117
ν_5 (A')	1455	1440	1068	1025	1434	1042
ν_6 (A')	1334	1319	1050	1025	1352	1031
ν_7 (A')	1112	1102	1027	1096	1131	1024
ν_8 (A')	1023	1016	821	814	1020	815
ν_9 (A')	958	953	769	–	962	754
ν_{10} (A')	635	672	583	607	596	557
ν_{11} (A')	373	382	331	340	297	274
ν_{12} (A')	286	308	245	262	251	216
ν_{13} (A')	261	231	188	–	183	133
ν_{14} (A")	3137	3010	2325	2253	3149	2337
ν_{15} (A")	3124	3010	2318	2253	3136	2327
ν_{16} (A")	3030	2933	2168	2132	3031	2166
ν_{17} (A")	1460	1419	1057	1043	1430	1033
ν_{18} (A")	1443	1405	1043	1025	1419	1025
ν_{19} (A")	1314	1304	1017	1015	1325	1004
ν_{20} (A")	930	933	755	756	949	767
ν_{21} (A")	890	–	671	–	895	674
ν_{22} (A")	663	695	594	615	682	622
ν_{23} (A")	318	333	292	307	329	306
ν_{24} (A")	234	207	166	–	158	112

[a] Ref. [145]

Table 5.4: Vertical excited states of DMSO calculated using TDDFT

CAMB3LYP/6-311G+(3d)					**Bodo *et al.*[a]**
Energy (eV)[b]	**Major Transition**	**Λ**	***A***	**Nature of transition**	**Energy (eV)[b]**
5.844 (0.005)	14a'→17a'	0.40	0.70	V/R	5.785 (0.004)
	14a'→16a'		0.50		
6.018 (0.060)	14a'→8a"	0.36	-0.85	V/R	6.043 (0.060)
6.285 (0.018)	14a'→15a'	0.30	-0.87	R	6.325 (0.029)
6.766 (0.094)	14a'→16a'	0.36	-0.77	V/R	6.777 (0.104)
6.952 (0.005)	7a"→17a'	0.32	-0.73	V/R	6.916 (0.009)
	7a"→16a'		-0.46		
7.241 (0.055)	14a'→19a'	0.40	0.72	V/R	7.218 (0.050)
	14a'→17a'		-0.49		
7.328 (<0.001)	14a'→18a'	0.36	0.81	V/R	7.320 (0.002)
7.381 (0.017)	7a"→15a'	0.27	0.77	R	7.361 (0.001)
7.424 (0.056)	7a"→8a"	0.35	0.83	V/R	7.505 (0.056)
7.512 (0.011)	7a"→15a'	0.29	0.52	R	7.511 (0.019)
	14a'→10a"		-0.51		
	14a'→9a"		0.43		
7.874 (0.023)	14a'→9a"	0.25	-0.79	R	7.925 (0.034)
8.062 (0.019)	7a"→16a'	0.28	0.77	R	8.100 (0.005)
8.139 (0.003)	14a'→20a'	0.28	0.94	R	8.134 (0.001)
	14a'→11a"	0.38	-0.74	V/R	
	14a'→10a"		-0.53		
8.414 (0.010)	7a"→19a'	0.32	0.65	V/R	8.231 (0.004)
	7a"→17a'		-0.46		
	7a"→18a'	0.31	0.78	V/R	8.435 (0.025)
	7a"→19a'		0.46		
8.681 (0.001)	7a"→10a"	0.33	-0.60	V/R	8.628 (0.050)
	14a'→21a'		0.45		
	7a"→9a"		0.34		
8.697 (0.034)	14a'→21a'	0.32	-0.81	V/R	8.709 (0.017)
8.802 (0.019)	14a'→22a'	0.43	0.92	V/R	
9.123 (0.040)	7a"→9a"	0.24	0.87	R	
9.222 (0.016)	14a'→12a"	0.35	0.88	V/R	
9.316 (0.004)	7a"→20a'	0.24	-0.91	R	
9.469 (0.039)	7a"→11a"	0.38	0.80	V/R	
9.511 (0.021)	13a'→8a"	0.35	0.80	V/R	
9.553 (0.086)	13a'→17a'	0.40	-0.68	V/R	
9.679 (0.009)	14a'→13a"	0.28	0.93		

[a]Ref.[134], [b]oscillator strength in parenthesis, *A*: amplitude, Λ: lambda diagnostic, V/R: valence/Rydberg character

5.3.2 EXPERIMENTAL RESULTS

5.3.2.1 MEDIUM RESOLUTION STUDIES: RYDBERG/VALENCE STATES AND VIBRONIC ASSIGNMENTS

The medium resolution (~1.5 Å) photoasborption spectra of DMSO-h_6(d_6) recorded using the Photophysics beamline are shown in Figure 5.2. The broad band at ~39,000 cm^{-1} (4.84 eV) is attributed to a valence S_o–S_1 transition in agreement with earlier work [135]. The first three IPs of DMSO corresponding to removal of an electron from the highest three MOs (14a′, 7a″, 13a′) are reported to lie at 9.10, 10.10 and 12.13 eV respectively [146]. Several Rydberg series converging to the first two IPs and a single Rydberg transition (4s) converging to the third IP are observed in the present work (*cf.* Table 5.5). For the first IP at 9.1 eV, *ns*, *np* and *nd* series are observed up to n=10, 10 and 8 respectively, while for the second IP at 10.1 eV, members are observed up to n=5, 6 and 3 respectively. Quantum defects calculated using the standard Rydberg formula are close to the atomic quantum defect values for sulphur atom, as expected. As can be seen from Table 5.5, the Rydberg series have been extended to several higher members as compared to earlier work [132] and a few bands have been reassigned. A few valence transitions have been reported by earlier workers [132, 136]. Most of these are observed in the present work (*cf.* Table 5.6), however a few of them are reassigned to Rydberg series on the basis of quantum defect analysis.

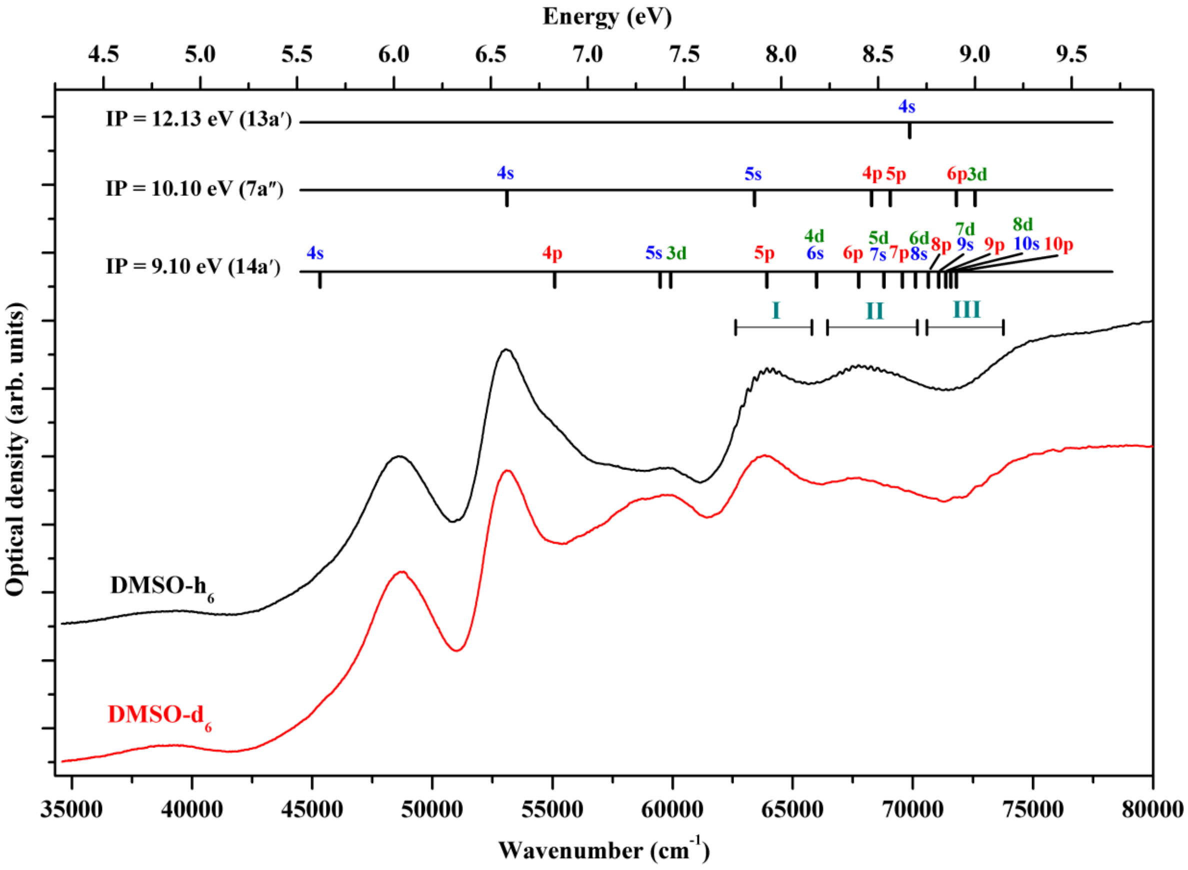

Fig. 5.2: The Photoabsorption spectra of DMSO and DMSO-d$_6$ in the region 35,000–80,000 cm^{-1}

Table 5.5: Rydberg series observed in the photoabsorption spectrum of DMSO

This work			**Drage *et al.* [132]**		**Sze *et al.* [136]**	
Peak Position (eV)	**Assignment**	**Quantum defect**	**Peak Position (eV)**	**Assignment**	**Peak Position (eV)**	**Assignment**
5.619	14a′→4s	2.02	5.572	14a′→4sσ		
6.831	14a′→4p	1.55	6.896	$n_s \to \sigma^*$	6.896	14a′→4p, 16a′
7.375	14a′→5s	2.19	7.384	14a′→3dδ		
7.440	14a′→3d	0.14	7.433	–	7.432	14a′→4d, 5s
7.926	14a′→5p	1.60	7.927	4pλ	7.924	14a′→5p; 7a″→4p, 16a′
8.182	14a′→6s	2.15				
	14a′→ 4d	0.15				
8.399	14a′→6p	1.60	8.400	3dδ	8.394	14a′→6p; 7a″→4d, 5s
8.530	14a′→7s	2.11				
	14a′→5d	0.11				
8.626	14a′→7p	1.64				
8.693	14a′→8s	2.22				
	14a′→6d	0.22				
8.758	14a′→8p	1.69				
8.813	14a′→9s	2.12				
	14a′→7d	0.12				
8.848	14a′→9p	1.65				
8.875	14a′→10s	2.22				
	14a′→8d	0.22				
8.904	14a′→10p	1.68				
6.584	7a″→4s	2.03	6.595	$n_s \to \sigma^*$	6.594	7a″→8a″, 4s
8.562	7a″→5s	2.03	8.562	7a″→5sσ		
7.862	7a″→4p	1.54				
8.904	7a″→5p	1.63				
8.999	7a″→6p	1.48	8.997	5pλ		
8.465	7a″→3d	0.12				
8.662	13a′→4s	2.02	8.664	$\sigma_{SO} \to \pi^*$	8.666	13a′→8a″, 4s

Table 5.6: Valence states observed in the spectrum of DMSO

Peak positions (eV)			**New assignments**
This work	**Drage *et al.* [132]**	**Sze *et al.* [136]**	
5.619	5.525	5.526	
6.027	6.030	6.029	
6.584	6.595	6.594	7a″→4s
6.831	6.896	6.896	14a′→4p
7.139	7.121	7.123	
7.430	7.433	7.432	14a′→3d
7.926	7.922	7.924	14a′→5p
8.395	8.394	8.394	
8.663	8.664	8.666	

Drage *et al.* [132] have reported three series (sub-regions marked as I, II and III in Figure 5.2). They have assigned all the three series to progressions of the CSO out of plane bending mode overlapped with SO stretching mode. However, the origins of the series are not specified by them. In the present study, only two vibronic progressions (series I and II) are observed. Of these, series II may be assigned to vibronic structure accompanying the 14a′→6s (3d) transition at 8.182 eV. However series I which starts at ~7.76 eV cannot be assigned to any of the Rydberg transitions predicted by the quantum defect analysis (*cf.* Table 5.5). The origin of this series may be a valence transition which however has not been identified in any of the works reported so far. The spectrum of the deuterated isotopologue, which is studied in an attempt to sort out these issues, shows only a few of the vibronic structures in series I and II and no structure in the region of series III (*cf.* Figure 5.2). This seems to imply that the vibrations that are excited may involve H atoms as opposed to the earlier assignment to CSO out of plane bending and SO stretching modes [132].

5.3.2.2 HIGH RESOLUTION STUDIES

In order to study the vibronic structure in more detail, high resolution studies of DMSO were performed using the HRVUV beamline. It is observed that the absorption features of DMSO obtained in the medium resolution studies and reported by earlier workers are reproduced only with respect to the overall broad profiles peaking at ~48,600 and 53,000 cm^{-1}, while several new spectral features appeared in various sub-regions. This may be attributed to photodissociation of DMSO due to the intense broadband radiation incident on the sample in the HRVUV beamline configuration.

The photodissociation dynamics of DMSO has been studied by several workers using 193 nm laser excitation [135, 147-151]. The electronic excitation at 193 nm corresponds to the $\pi^* \leftarrow \pi_{SO}$ transition in the S–O group which is well above the energy required to break the two C–S bonds in $(CH_3)_2SO$, and results in formation of the primary products $(CH_3)_2$ and SO [150]. At shorter wavelengths the electronic σ*(d)←n transition (210 nm) and π*←n transition (222 nm) have also been shown to release the primary products $(CH_3)_2$ and SO [133]. It has been established from these experiments [135, 147-151] that most of the other possible fragments require extensive nuclear rearrangements that make their production unlikely. The most favorable reactions are:

$$(CH_3)_2SO \begin{cases} \rightarrow CH_3 + CH_3SO & (\Delta H^o=218\ \text{kJ/mol; } 2.26\ \text{eV}) \\ \rightarrow CH_3 + CH_3 + SO & (\Delta H^o=431\ \text{kJ/mol; } 4.47\ \text{eV}) \\ \rightarrow CH_3 + CH_2SO + H & (\Delta H^o=456\ \text{kJ/mol; } 4.73\ \text{eV}) \end{cases}$$

In all the above experiments, emphasis has been placed on the fact that DMSO photolysis proceeds through initial loss of one methyl group at low energies followed by secondary decomposition of CH_3SO to produce the second methyl group and SO fragments rather than a direct three body fragmentation to release of two methyl group and SO as primary products. Analysis of the peaks obtained in the present study shows that a large number of spectral features match very well with the absorption bands of the SO radical reported in earlier literature [152-155]. Moreover, the spectral features of the dissociation products obtained are reproduced in both DMSO-h_6 and DMSO-d_6. This supports the conjecture that the observed bands are due to dissociation products which do not contain H atoms. The spectrum can be conveniently divided into three sub-regions for analysis.

The 48,000–52,000 cm^{-1} region

The absorption spectrum of SO obtained in the photodissociation of DMSO-h_6 and DMSO-d_6 recorded on the HRVUV beamline in the region 48,000–52,000 cm^{-1} is shown in Figure 5.3. The major electronic transition lying in this energy region is the $e^1\Pi$–$X^3\Sigma^-$ system, although vibronic bands accompanying the $d^1\Pi$, $B^3\Sigma^-$ and $C^3\Pi$ systems also may appear here

[154]. Most of the bands observed in the present study could be fitted to the vibronic transitions belonging to the $e^1\Pi$–$X^3\Sigma^-$ system, assuming the ground and excited state vibrational wavenumbers of SO to be 1148 cm^{-1} and 705 cm^{-1} respectively [154, 156]. These have been marked in Figure 5.3 and listed in Table 5.7. It may be mentioned here, that inverted population distributions for the photodissociated SO fragment have been reported earlier [133, 147, 148]; in particular for photoexcitation at 193, 210 and 220 nm, population has been found to be maximum in the v″= 2, 1 and 1 levels respectively.

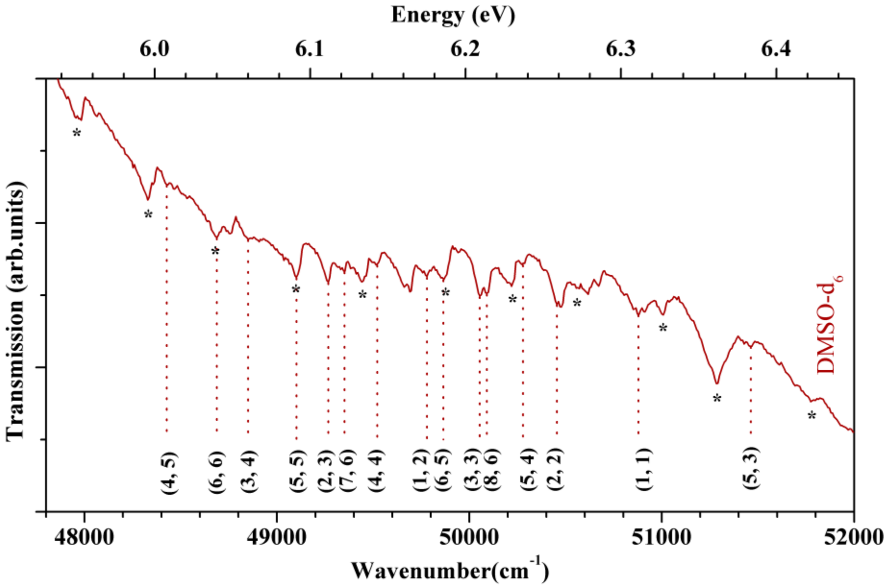

Fig. 5.3: The absorption spectrum of SO obtained in the photodissociation of DMSO-d$_6$ recorded on the HRVUV beamline in the region 48,000–52,000 cm^{-1}

Table 5.7: Transitions of SO observed in the photodissociation of DMSO

<table>
<tr><th colspan="4">$e^1\Pi$-$X^3\Sigma^-$ system in the region 48,000–52,000 cm^{-1}</th></tr>
<tr><th>Peak position (cm^{-1})</th><th>Assignment (v′,v″)</th><th>Peak position (cm^{-1})</th><th>Assignment (v′,v″)</th></tr>
<tr><td>48,429</td><td>(4, 5)</td><td>49,863</td><td>(6, 5)</td></tr>
<tr><td>48,684</td><td>(6, 6)</td><td>50,054</td><td>(3, 3)</td></tr>
<tr><td>48,849</td><td>(3, 4)</td><td>50,091</td><td>(8, 6)</td></tr>
<tr><td>49,099</td><td>(5, 5)</td><td>50,278</td><td>(5, 4)</td></tr>
<tr><td>49,268</td><td>(2, 3)</td><td>50,455</td><td>(2, 2)</td></tr>
<tr><td>49,352</td><td>(7, 6)</td><td>50,879</td><td>(1, 1)</td></tr>
<tr><td>49,521</td><td>(4, 4)</td><td>51,463</td><td>(5, 3)</td></tr>
<tr><td>49,776</td><td>(1, 2)</td><td></td><td></td></tr>
<tr><th colspan="4">Absorption bands in the region 62,500–76,500 cm^{-1}</th></tr>
<tr><th colspan="2">Rydberg series</th><th colspan="2">Vibrational features</th></tr>
<tr><th>Peak position (cm^{-1})</th><th>Assignment</th><th>Peak position (cm^{-1})</th><th>Assignment (v′,v″)</th></tr>
<tr><td>62,757</td><td>$4p\pi^3\Delta$ (F)</td><td>67,695</td><td>(0, 0)</td></tr>
<tr><td>66,240</td><td>$3d\delta^3\Pi$ (E)</td><td>69,106</td><td>(1, 0)</td></tr>
<tr><td>67,695</td><td>$3d\sigma^3\Pi$ (G)</td><td>70,488</td><td>(2, 0)</td></tr>
<tr><td>74,816</td><td>4d</td><td>71,927</td><td>(3, 0)</td></tr>
<tr><td>76,380</td><td>6d</td><td></td><td></td></tr>
</table>

In the present work vibronic bands corresponding to excitation from higher v″ levels (up to v″=6) are observed. Throughout this energy region, several peaks identified as belonging to the B–X absorption system of SO_2 [157] are also observed (marked with * in Figure 5.3). Since it is very unlikely that the parent molecule produces SO_2 on photodissociation [135, 147-151], these are attributed to residual SO_2 which was used for wavelength calibration.

The 52,000–62,000 cm^{-1} region

In this energy region, the broad hump seen in the spectrum of DMSO-h_6/d_6. The 4s Rydberg state of SO also appears at ~55,000 cm^{-1}. No other features attributable to SO are observed.

The 62,000–78,000 cm^{-1} region

In this energy region, the absorption bands observed are assigned mainly to the Rydberg states converging to the first ionization potential of SO at 10.30 eV [158, 159] and accompanying vibronic features of the SO radical as listed in Table 5.7 and marked appropriately in Figure 5.4.

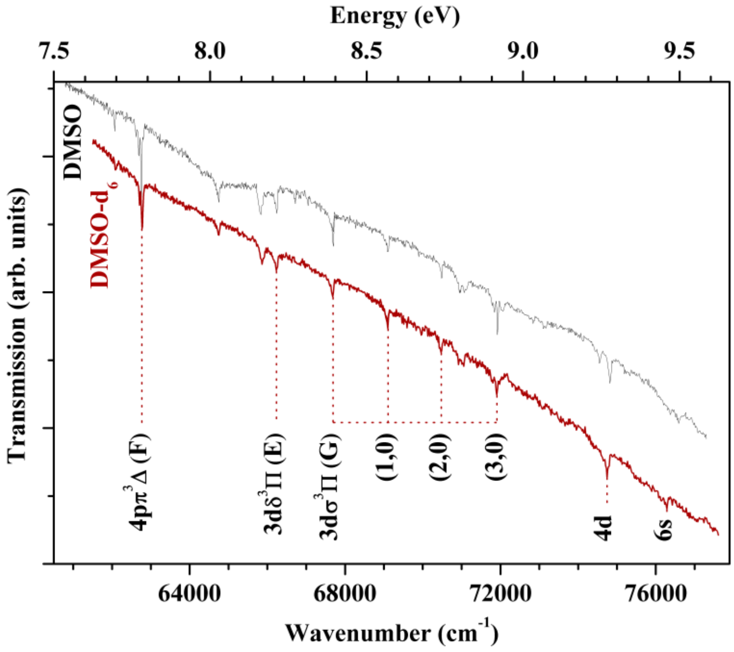

Fig. 5.4: The absorption spectrum of SO obtained as the photodissociated product of DMSO and DMSO-d_6 recorded on the HRVUV beamline in the 62,000–78,000 cm^{-1} region

The quantum defect values obtained using the standard Rydberg formula and are consistent with atomic quantum defect values of the sulphur atom. A few peaks however could not be assigned to Rydberg series or vibronic bands of SO. Further investigations are required to ascertain the origin of these peaks, some of which could be due to other dissociation products. It may be noted that all the features assigned to bands of SO in the present work are exactly reproduced in the spectra obtained by photodissociation of DMSO-h_6 as well as DMSO-d_6. This reaffirms the interpretation of these peaks in terms of photoabsorption by the SO radical.

CHAPTER 6

ELECTRONIC SPECTROSCOPY OF NITROUS OXIDE

6.1 INTRODUCTION

There has been continued interest in the spectroscopy of the nitrous oxide (N_2O) molecule due to its important role in atmospheric and astrophysical processes [160-164]. For example, the isotopic fractionation of nitrogen atoms in the upper atmosphere has been ascribed to the UV photodissociation dynamics of N_2O [162]. Photodissociation of N_2O is known to produce metastable species such as O (^1S, ^1D) which participate in important atmospheric photochemical reactions. Recent studies show that N_2O is the single largest anthropogenic threat to the ozone layer in the 21st century and also has a very high global warming potential [160]. It has been found to be involved in the catalytic destruction of ozone in the stratosphere and to be the main source of odd nitrogen which regulates the ozone layer, and also could be the only interstellar compound in which the N atom uses all five valence electrons [163]. Understanding of its excited state structure and dynamics has been greatly enhanced by studies carried out using a variety of experimental techniques [162-184] as well as theoretical calculations [185-194]. Nevertheless, a thorough understanding of the excited states of this molecule still remains a challenging problem.

The electronic absorption spectrum of N_2O spans a wide energy region, from the UV region (5.58 eV) and extending deep into the VUV region, where a number of electronic transitions comprising of both valence transitions and Rydberg series converging to the lowest two ionization limits at ~12.89 and 12.91 eV [176] are observed. The first VUV absorption spectrum of nitrous oxide was reported by Duncan in 1936 [165] and subsequently revisited by Sponer and Teller [166], Zelikoff *et al*. [167] and Tanaka *et al.* [168]. Early work on nitrous oxide is well summarized in the review by Rabalais *et al*. [169]. The only synchrotron radiation based photoabsorption study of this molecule was by Nee *et al.* [170] who reported absolute cross sections up to the first IP, but no new spectral assignments were given. Additionally, there have also been a number of reports on the electronic spectrum of N_2O, focusing on specific aspects in small energy regions. From a theoretical perspective, the electronic spectroscopy of nitrous oxide presents many challenges with additional complications introduced due to perturbations like Renner-Teller coupling and spin-orbit splitting. There have been a wide range of theoretical studies covering various aspects like geometry and stability of its three isomers [185], photodissociation dynamics [186-190], excited electronic states [191-194], etc. A special mention must be made about the work by Hopper [193] which remains one of the most comprehensive theoretical studies of the electronic structure of N_2O till date. Also worth citing are the frozen core calculations by Cossart-Magos *et al.* [176] which have helped in assigning many Rydberg transitions.

The Rydberg states of N_2O (energy region >9.3 eV) have been studied experimentally by several authors using a variety of techniques like photoabsorption spectroscopy [168, 170, 174, 176, 177], resonance enhanced multiphoton ionization (REMPI) [178-181] and electron impact/electron energy loss spectroscopy [182-184]. Assignments of Rydberg series and accompanying vibronic structures reported in these works are at wide variance with each other and a clear set of assignments is still not available. For example, the strong sharp band at ~10.5eV has been assigned to the origin of the $3p\sigma\,^1\Pi$ transition in some works [176, 183], and to the 3_0^1 vibronic band of $3p\sigma\,^1\Pi$ by others [178, 179]. Although some of these discrepancies were resolved in the work by Cossart-Magos *et al*. [176], still several issues in assignments of transitions in the region 10.5–11.8 eV region remain unresolved. In this chapter, the Rydberg states of N_2O are revisited by a synchrotron radiation based study of its VUV spectrum in the region 8.9–11.8 eV, with the help of quantum chemical calculations.

6.2 METHODOLOGY

6.2.1 EXPERIMENTAL

Photoabsorption spectra of N_2O are recorded using the gas phase absorption setup on the Photophysics beamline as described in Chapter 1. Nitrous oxide (procured from M/s. Alchemie Gases) of stated purity of 99.9 % is used without further purification. The 0.5 litre cylinder is connected to the system though a standard ¼″ ferrule connector and introduced into the cell through a system of Swagelok needle valves. Due to the widely varying absorption cross sections in different wavelength regions, optimum pressures also differ from region to region. To take care of this aspect, spectra are recorded at several pressures. The optimum pressure for obtaining clear absorption features in the 8.9–11.8 eV region is found to be ~0.001 mbar. Standard atomic lines of xenon are used for calibration of the spectra.

6.2.2 COMPUTATIONAL

N_2O is a 16 valence electron system with a linear $C_{\infty v}$ geometry, the ground state molecular orbital configuration being given by: $1\sigma^2\ 2\sigma^2\ 3\sigma^2\ 4\sigma^2\ 5\sigma^2\ 6\sigma^2\ 1\pi^4\ 7\sigma^2\ 2\ \pi^4$: $^1\Sigma^+$. There have been several theoretical studies [185-194] on the electronic states of N_2O, the most exhaustive one being the work by Hopper in 1984 [193] reporting extensive MCSCF/CI calculations of several vertically excited singlet and triplet states as well as some potential energy surfaces. To the best of our knowledge, there is no reported calculation of excited states up to the first ionization limit using TDDFT.

In the present study, as in the earlier chapters, the DFT and MP2 methods are used for geometry optimization and computation of vibrational wavenumbers of the neutral and ionic ground states, while TDDFT calculations are used for prediction of vertical excited states. Basis sets used in the calculations include Pople's split valence basis set 6-31G(3d) with three d-type polarization functions [33], correlation consistent polarized basis sets of Dunning cc-pV*n*Z [36, 37] and the polarization consistent basis sets of Jensen, pc-4 [195, 196]. DFT computations are carried out using two hybrid exchange correlation GGA functionals, *viz.*, PBE0 [64] and B3LYP [25, 65].

6.3 RESULTS AND DISCUSSION

6.3.1 GEOMETRY OPTIMIZATION AND COMPUTATION OF VIBRATIONAL FREQUENCIES

The contour plots of the HOMO ($2\pi_x, 2\pi_y$) and the LUMO ($3\pi_x, 3\pi_y$) calculated at the PBE0/pc-4 level of theory are shown in Fig 6.1. The HOMO (2π) has an N–N bonding and N–O antibonding character while the LUMO (3π) is antibonding with respect to both N–N and N–O. It is observed experimentally that in the ground state of the N_2O^+ ion, the molecule remains linear with an increase in r(N–N) bond length by 0.027 Å while the r(N–O) bond length remains almost the same as in the neutral molecule (*cf.* Table 6.1). This is also borne out by the N–N bonding and N–O antibonding character of the HOMO, from which the electron is removed. The optimized bond lengths of the ground states of N_2O and N_2O^+

calculated by DFT using PBE0 are shown in Tables 6.1. The ground state vibrational frequencies of N_2O and N_2O^+ at the PBE0/pc-4 level of theory are shown in Table 6.2. Differences between the calculated and observed [197] frequencies may be attributed to neglect of anharmonicity in the calculation.

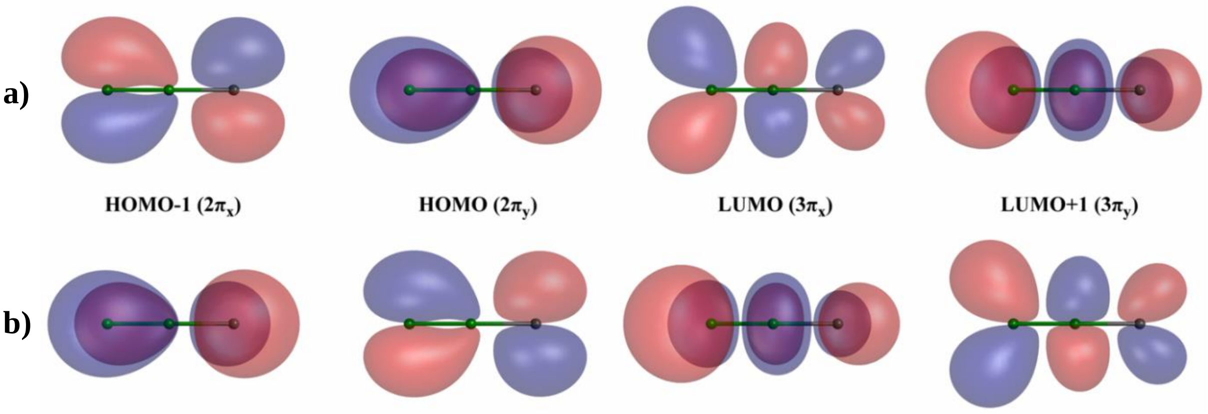

Fig. 6.1: Contour plots of HOMO ($2\pi_x$, $2\pi_y$) and the LUMO ($3\pi_x$, $3\pi_y$) of N_2O viewed along a) X-axis and b) Y-axis

Table 6.1: Optimized bond lengths (Å) of ground states of N_2O and N_2O^+ calculated by DFT using the functional PBE0

Basis set	N_2O: $X^1\Sigma^+$		N_2O^+: $^2\Pi$	
	r(N–N)	r(N–O)	r(N–N)	r(N–O)
6-311G+d	1.122	1.176	1.135	1.178
cc-pV5Z	1.117	1.175	1.132	1.178
pc-4	1.117	1.174	1.132	1.177
Experimental	1.127[a]	1.185[a]	1.154[b]	1.185[b]

[a]Ref. [197], [b]Ref. [198]

Table 6.2: The ground state vibrational frequencies (cm^{-1}) of N_2O and N_2O^+ calculated by DFT using PBE0/pc-4

Vibrational Mode	N_2O		N_2O^+	
	This work	Experimental[a]	This work	Experimental[b]
ν_1	1376	1284.9	1247	1127
ν_2	637	588.8	499	457
ν_3	2405	2223.8	1876	1738

[a]Ref. [197], [b]Ref. [198]

6.3.2 VERTICAL EXCITED STATE ENERGIES

Vertical excited states are calculated at the ground state optimized geometry using the TDDFT method with several basis sets and DFT functionals. The best results in terms of overall agreement with current experimental data and earlier theoretical work [193] are obtained for the PBE0 functional using the pc-4 basis set. Predicted singlet and triplet excited states up to ~14 eV along with calculated oscillator strengths (f) and lambda diagnostic values Λ are presented in Table 6.3. In the present work, it is found that although most Rydberg transitions are predicted with lambda value of <0.3, there are a few transitions which are clearly Rydberg type from the nature of the final orbital, but predicted with Λ = 0.3–0.4. It is also observed that for N_2O, when the final orbital is 3π, the transition is typically valence in nature, whereas for 4π, 8σ, 9σ, 10σ… the excited state is Rydberg in nature (*cf.* Table 6.3). Valence-Rydberg mixed transitions result when there are two excitations predicted with comparable amplitude, typically one of valence type and the other of Rydberg type.

6.3.3 EXPERIMENTAL OBSERVATIONS AND CORRELATION WITH COMPUTATIONAL RESULTS

The VUV photoabsorption spectrum of N_2O in the region 8.9–11.8 eV is shown in Figure 6.2. Analysis and interpretation of the absorption bands are discussed in the following sections, aided by theoretical calculations wherever relevant. The correspondence of theoretically predicted excitation energies and experimentally observed bands is based on initial and final state molecular orbitals involved as well as comparison of the observed and calculated energies. As mentioned in Chapter 1, the accuracy of the calculated values is expected to be very good up to the energy of the HOMO plus 1 eV [31], which in the present case corresponds to ~10.85 eV. Above this energy, the agreement with experimental values becomes somewhat poorer.

Table 6.3: Singlet and triplet vertical excited states of N_2O calculated using TDDFT: PBE0/pc-4

State	E (eV)	Major Transitions	*f*	Λ	Assignment (Nature)	Observed energy (eV)
$^3\Sigma^+$	5.244	2π→3π	0.000	0.762	a$^3\Sigma^+$ (V)	–
$^3\Delta$	5.898	2π→3π	0.000	0.481/0.768*	b$^3\Delta$ (V)	–
$^3\Sigma^-$	6.857	2π→3π	0.000	0.487	c$^3\Sigma^-$ (V)	–
$^1\Sigma^-$	6.857	2π→3π	0.000	0.487	A$^1\Sigma^-$ (V)	5.6–7.7
$^1\Delta$	7.242	2π→3π	0.000	0.488/0.779*	B$^1\Delta$ (V)	
$^3\Pi$	8.376	2π→8σ	0.000	0.390	3sσ$^3\Pi$ (R)	7.7–8.9
$^1\Pi$	8.757	2π→8σ	0.000	0.389	3sσC$^1\Pi$ (R)	
$^3\Pi$	9.473	7σ→3π	0.000	0.616	7σ→π*(V)	
$^1\Sigma^+$	10.034	2π→3π; 2π→4π	0.423	0.539	3pπ D$^1\Sigma^+$(R+V)	9.1–10.1
$^3\Sigma^+$	10.383	2π→4π	0.000	0.391	(R)	–
$^3\Pi$	10.484	2π→9σ	0.000	0.206	3pσ $^3\Pi$ (R)	10.47
$^3\Delta$	10.526	2π→4π	0.000	0.245/0.390*	(R)	–
$^1\Pi$	10.576	2π→9σ	0.078	0.205	3pσ $^1\Pi$ (R)	10.53
$^1\Delta$	10.658	2π→4π	0.000	0.241/0.384*	(R)	–
$^1\Sigma^-$	10.693	2π→4π	0.000	0.243	(R)	–
$^3\Sigma^-$	10.693	2π→4π	0.000	0.243	3pπ $^3\Sigma^-$(R)	10.48
$^3\Sigma^+$	11.049	1π→3π	0.000	0.788	(V)	–
$^1\Pi$	11.477	7σ→3π; 2π→10σ	0.022	0.522	7σ→π*(V+R)	10.84
$^3\Pi$	11.552	2π→10σ	0.000	0.234	4sσ $^3\Pi$ (R)	10.94
$^1\Pi$	11.659	2π→10σ; 7σ→3π	0.050	0.320	4sσ $^1\Pi$ (R)	11.05
$^3\Delta$	11.745	1π→3π	0.000	0.471/0.751*	(V+R)	–
$^3\Sigma^+$	12.103	2π→5π	0.000	0.328	(R)	–
$^3\Pi$	12.219	2π→10σ; 2π→11σ	0.000	0.423	4pσ $^3\Pi$ (R)	11.74
$^1\Sigma^+$	12.245	7σ→8σ; 2π→4π	0.267	0.426	4pπ $^1\Sigma^+$ (R)	11.64
$^3\Delta$	12.270	2π→5π	0.000	0.237/0.378*	(R)	–
$^1\Delta$	12.280	2π→5π	0.000	0.179/0.287*	(R)	–
$^3\Sigma^-$	12.324	2π→5π	0.000	0.185	4pπ $^3\Sigma^-$ (R)	11.74
$^1\Sigma^-$	12.324	2π→5π	0.000	0.188	(R)	–
$^3\Sigma^+$	12.436	7σ→8σ	0.000	0.268	(R)	–
$^1\Sigma^+$	12.584	2π→5π	0.104	0.303	(R)	–
$^1\Sigma^+$	12.725	7σ→8σ	0.312	0.291	(R)	–
$^3\Sigma^-$	12.892	1π→3π	0.000	0.519	(V)	–
$^1\Sigma^-$	12.892	1π→3π	0.000	0.519	(V)	–
$^1\Pi$	12.962	1π→12σ; 2π→12σ	0.001	0.423	4pσ $^1\Pi$ (R)	–
$^1\Delta$	13.297	1π→3π	0.000	0.527/0.841*	(V)	–
$^3\Pi$	13.636	7σ→ 3π	0.000	0.578	(V)	–
$^3\Sigma^+$	13.837	7σ→9σ	0.000	0.268	(R)	–
$^1\Pi$	13.940	2π→11σ; 2π→12σ	0.046	0.403	4pσ $^1\Pi$ (R)	11.76

Λ: Lambda diagnostic, R:Rydberg, V: valence; *f*: oscillator strength, *two values of Λ for the two components of the degenerate Δ state

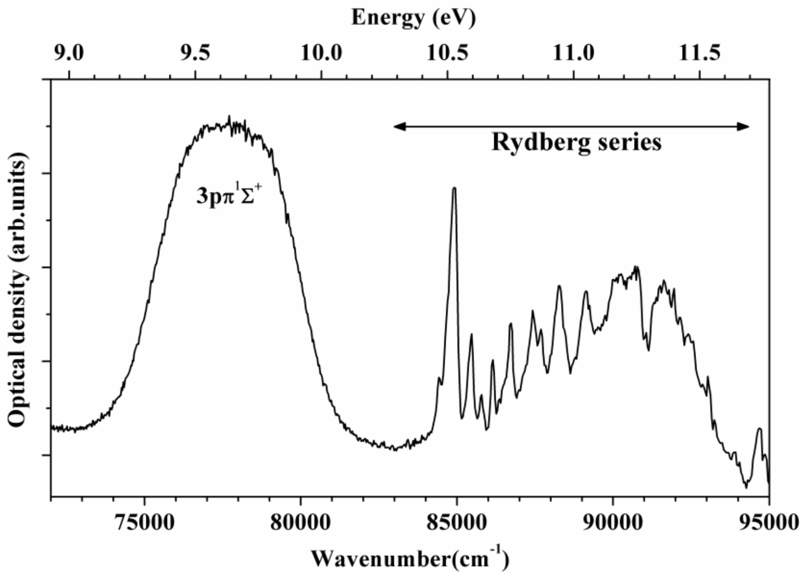

Fig. 6.2: Photoabsorption spectrum of N_2O in the region 8.9–11.8 eV (72,000–95,000 cm^{-1})

In the region 8.9–10.2 eV, a single highly intense and broad peak (~9.62 eV) is observed. At all pressures used, no vibronic features are distinguished riding on the continuum. This peak has been observed in earlier photoabsorption studies [170] and was assigned to the $3p\pi\,^1\Sigma^+$ Rydberg transition converging to the (adiabatic) IP 12.89 eV $(^2\Pi_{3/2})$ by Cossart-Magos *et al.* [176]. The rather high quantum defect value of 0.96 (*cf.* Table 6.4) obtained for this transition is uncharacteristic of a p-type Rydberg state and had been attributed to a bond bending stabilization effect by Cossart-Magos *et al.* [176]. As can be seen in Table 6.3, the only excited state in this energy region with high oscillator strength is the $D\,^1\Sigma^+$ state at 10.034 eV. Dominant contributions to this transition are from 2π–3π (valence) and 2π–4π (Rydberg), with lambda diagnostic value of 0.54. Thus, it is concluded that the state $D\,^1\Sigma^+$ has a mixed valence-Rydberg character, thereby explaining the unusual quantum defect.

The energy region 10.2–11.8 eV (*cf.* Figure 6.3) is dominated by richly structured Rydberg series converging to the spin-orbit components of the ionic ground state of N_2O at 12.89 eV $(^2\Pi_{3/2})$ and 12.91 $(^2\Pi_{1/2})$ [176]. Previous studies of this region include several

REMPI experiments [178-180], photoabsorption studies with laboratory sources [168, 176] and with synchrotron radiation source [170]. In this energy region 9.3–12.9 eV, the work by Cossart-Magos *et al.* [176] is the most extensive study available, in which several Rydberg series are assigned based on frozen core (FRC) calculations. There is considerable discrepancy in spectral assignments made by different authors [170, 176, 178-180]. In this work, an attempt has been made to sort out some of the discrepancies and to arrive at a consistent set of assignments as discussed in the subsequent sections. Several distinct bands are observed with good intensity in the present study which were either absent or reported as weak in the work by Cossart_Magos *et al.* [176]. Rydberg series and vibronic structures observed in the present study are listed in Table 6.4 along with previous studies for comparison. Quantum defect values calculated in the present study are also indicated in the table.

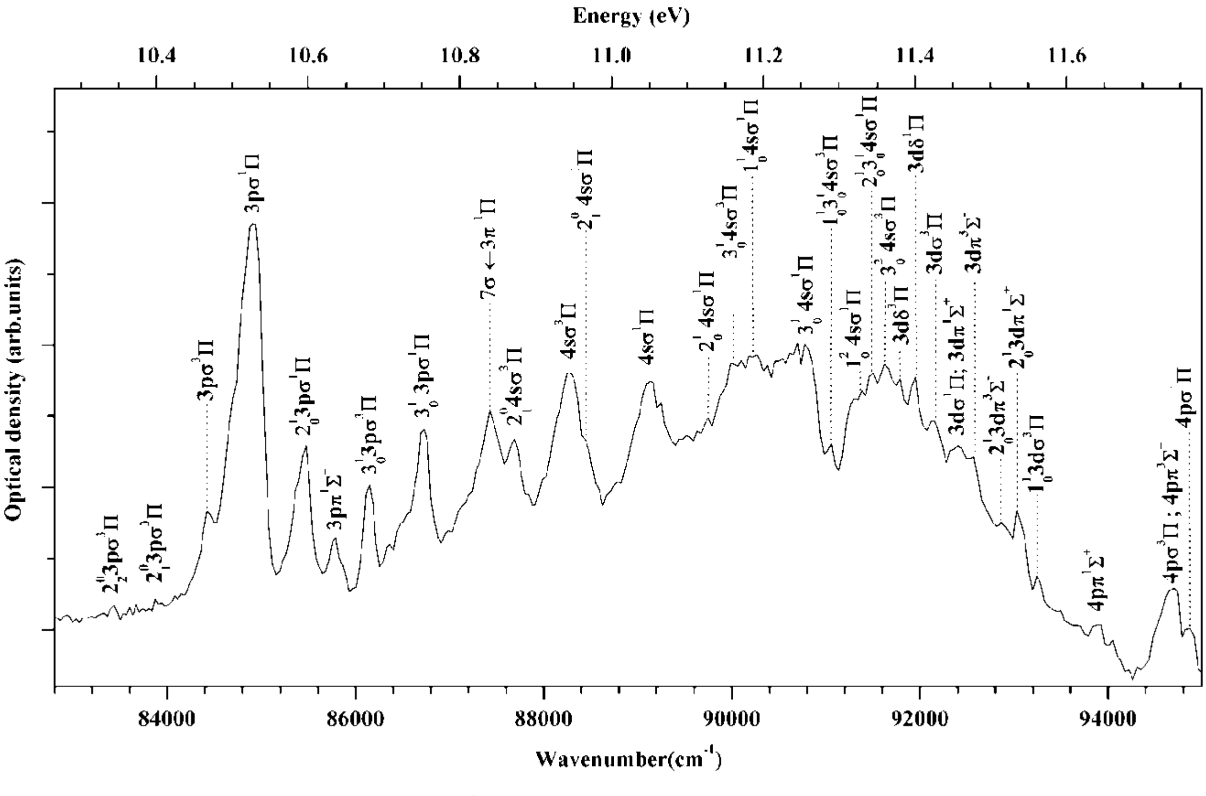

Fig. 6.3: VUV photoabsorption spectrum of N_2O showing Rydberg series in the region 10.2–11.8 eV (82,000–95,000 cm^{-1})

Table 6.4: Observed transitions in the VUV photoabsorption spectrum of N_2O in the region 9.3–11.8 eV

Present study			**Ref. [176]**		**Ref. [170]**		**Ref. [180]**		**Ref. [179]**		**Ref. [178]**	
Peak[a]	**Assignment**	**Q. D.**	**Peak**	**Assignment**	**Peak**	**Assignment**	**Peak**	**Assignment**	**Peak**	**Assignment**	**Peak**	**Assignment**
9.621	$3p\pi\ ^1\Sigma^+$	0.96	–	$3p\pi\ ^1\Sigma^+$	9.611	$D^1\Sigma^+$						
							10.257	$3p\sigma\ ^3\Pi$	10.294		10.259	$3^1_1\ 3p\sigma\ ^1\Pi$
											10.296	$2^1_1\ 3p\sigma\ ^1\Pi$
					10.323	$3p\sigma\ ^1\Pi$	10.313	$3p\sigma\ ^1\Pi$	10.314	$0^0_0\ 3p\pi\ ^1\Delta$	10.315	$0^0_0\ 3p\sigma\ ^1\Pi$
									10.335	$2^1_1\ \Delta\ (N_2O^+?)$		
10.344	$2^0_2\ 3p\sigma\ ^3\Pi$											
									10.368	$2^2_1\ \Sigma^+$	10.369	$2^1_0\ 3p\sigma\ ^1\Pi$
10.404	$2^0_1\ 3p\sigma\ ^3\Pi$								10.404	$2^1_0\ \Delta$		
									10.422	$2^2_0\ \Phi$	10.422	$2^2_0\ 3p\sigma\ ^1\Pi$
									10.456	$1^1_0\ 3p\sigma\ ^1\Pi$	10.457	$1^1_0\ 3p\sigma\ ^1\Pi$
10.469	$0^0_0\ 3p\sigma\ ^3\Pi$	0.63	10.462	$3p\sigma\ ^3\Pi$								
			10.493	$3p\pi\ ^3\Sigma^-$					10.511	$3^1_0\ 2^1_1$		
10.528	$0^0_0\ 3p\sigma\ ^1\Pi$	0.61	10.528	$0^0_0\ 3p\sigma\ ^1\Pi$	10.516	$3^1_0\ 3p\sigma\ ^1\Pi$			10.531	$3^1_0\ 3p\sigma\ ^1\Pi$	10.530	$3^1_0\ 3p\sigma\ ^1\Pi$
10.596	$2^1_0\ 3p\sigma\ ^1\Pi$		10.598	$2^1_0\ 3p\sigma\ ^1\Pi$	10.588	$1^1_0\ 3p\sigma\ ^1\Pi$			10.593		10.596	$1^2_0\ 3p\sigma\ ^1\Pi$
10.636	$3p\pi\ ^3\Sigma^-$	0.55										
10.681	$3^1_0\ 3p\sigma\ ^3\Pi$		10.678	$3^1_0\ 3p\sigma\ ^3\Pi$							10.664	$0^0_0\ 3p\pi\ ^1\Sigma^+;\ ^1\Delta$
10.708 (w)												
10.726 (sh)									10.722			

[a] $^1\Sigma^+$ and $^3\Pi$ converge to $^2\Pi_{3/2}$ at 12.89 eV ; $^3\Sigma^-$ and $^1\Pi$ converge to $^2\Pi_{1/2}$ at 12.91 eV

Table 6.4 (*continued from previous page*)

Present study			**Ref. [176]**		**Ref. [170]**		**Ref. [180]**		**Ref. [179]**		**Ref. [178]**	
Peak[a]	**Assignment**	**Q. D.**	**Peak**	**Assignment**	**Peak**	**Assignment**	**Peak**	**Assignment**	**Peak**	**Assignment**	**Peak**	**Assignment**
10.751	3^1_0 3pσ $^1\Pi$		10.746	3^1_0 3pσ $^1\Pi$	10.744	3^2_0 3pσ $^1\Pi$			10.742		10.749	1^3_0 3pσ $^1\Pi$
10.784 (w)											10.774	3^2_0 3pσ $^1\Pi$
10.811 (sh)											10.802	1^1_0 3pπ $^1\Sigma^+$; $^1\Delta$
10.840	7σ → 3π $^1\Pi$				10.828	1^2_0 3pσ $^1\Pi$					10.841	0^0_0 3dσ $^1\Pi$
10.872	2^0_1 4sσ $^3\Pi$										10.875	3^1_0 3pπ $^1\Sigma^+$; $^1\Delta$
10.911 (sh)											10.914	0^0_0 3dπ $^1\Sigma^+$; $^1\Delta$
10.943	4sσ $^3\Pi$	1.36	10.943	4sσ $^3\Pi$	10.933	3^3_0 3pσ $^1\Pi$						
10.965 (sh)	2^0_1 4sσ $^1\Pi$											
11.007 (w)												
11.051	4sσ $^1\Pi$	1.29	11.053	4sσ $^1\Pi$								
11.065 (w)												
					11.031	3^1_0 3dδ $^1\Pi$ $^1\Phi$					11.031	0^0_0 3dδ $^1\Pi$ $^1\Phi$
11.098 (w)												
11.128	2^1_0 4sσ $^1\Pi$											
11.163	3^1_0 4sσ $^3\Pi$											
11.187	1^1_0 4sσ $^1\Pi$											
11.222												
11.250	3^1_0 4sσ $^1\Pi$				11.241							
11.289	1^1_0 3^1_0 4sσ $^3\Pi$											

[a] $^1\Sigma^+$ and $^3\Pi$ converge to $^2\Pi_{3/2}$ at 12.89 eV ; $^3\Sigma^-$ and $^1\Pi$ converge to $^2\Pi_{1/2}$ at 12.91 eV

Table 6.4 (*continued from previous page*)

Present study			Ref. [176]		Ref. [170]		Ref. [180]		Ref. [179]		Ref. [178]	
Peak[a]	**Assignment**	**Q. D.**	**Peak**	**Assignment**	**Peak**	**Assignment**	**Peak**	**Assignment**	**Peak**	–	**Peak**	**Assignment**
11.330	1^2_0 4sσ $^1\Pi$						11.318	4sσ $^3\Pi$				
11.344	$2^1_0\,3^1_0$ 4sσ $^1\Pi$						11.337	4sσ $^1\Pi$				
11.360	3^2_0 4sσ $^3\Pi$				11.354							
11.380	3dδ $^3\Pi$	-0.002										
11.401	3dδ $^1\Pi$	-0.006										
11.424	3dσ $^3\Pi$	-0.05										
11.456	3dσ $^1\Pi$	-0.06										
	3dπ $^1\Sigma^+$	-0.08										
11.476 (sh)	3dπ $^3\Sigma^-$	-0.08										
11.513	2^1_0 3dπ $^3\Sigma^-$											
11.534	3dπ $^1\Sigma^+$											
11.560	1^1_0 3dσ $^3\Pi$											
11.640	4pπ $^1\Sigma^+$	0.70					11.643	4pσ $^3\Pi$				
11.659 (w)			11.665	4pπ $^1\Sigma^+$	11.674	4pσ $^1\Pi$	11.664	4pσ $^1\Pi$				
11.741	4pσ $^3\Pi$	0.56	11.741	4pσ $^3\Pi$								
	4pπ $^3\Sigma^-$	0.58										
			11.748	4pπ $^3\Sigma^-$			11.742	4pπ $^3\Sigma^+$				
11.763	4pσ $^1\Pi$	0.55	11.766	2^1_1 4pσ $^1\Pi$			11.766	4pπ $^1\Sigma^+$				
			11.767	4pσ $^1\Pi$								

[a] $^1\Sigma^+$ and $^3\Pi$ converge to $^2\Pi_{3/2}$ at 12.89 eV ; $^3\Sigma^-$ and $^1\Pi$ converge to $^2\Pi_{1/2}$ at 12.91 eV

Rydberg series observed in the electronic absorption spectrum of N_2O are due to transitions from the ground state to excited orbitals of type nlλ. Since the excitation is primarily from the HOMO 2π orbital, it can be deduced from the character table of $C_{\infty v}$ point group, that the nsσ, npσ and ndσ series give rise to $^{1,3}\Pi$ states, whereas the npπ and ndπ series give rise to $^{1,3}\Sigma^{\pm}$ and $^{1,3}\Delta$ states. Similarly, the ndδ series give rise to $^{1,3}\Pi$ and $^{1,3}\Phi$ states. From electric dipole selection rules, only transitions to $^1\Sigma^+$ and $^1\Pi$ states are expected to appear in the photoabsorption spectrum. However due to spin orbit coupling, triplet states also become allowed. The $^3\Pi_{2,1}$ series converge to the spin-orbit split ionic state $^2\Pi_{3/2}$ whereas $^3\Pi_0$ and $^1\Pi_1$ converge to the ionic state $^2\Pi_{1/2}$ [176, 199]. In case of Σ states arising from a $\pi \rightarrow \pi^*$ excitation, the spin orbit operator couples states with opposite behavior with respect to the σ_v operator, *i.e.*, Σ^+ is coupled to Σ^- [199]. Thus, transitions from the $^1\Sigma^+$ ground state become allowed to excited states of $^1\Sigma^+$ and $^3\Sigma^-$ symmetry through the spin-orbit mixing mechanism and $^1\Sigma^+$ series converge to $^2\Pi_{3/2}$, whereas the $^3\Sigma^-$ series converge to $^2\Pi_{1/2}$ [176, 198]. It is worth mentioning that, for most of the Rydberg transitions observed, triplet states appear with intensity comparable to that of singlets. This is an indication of strong spin-orbit coupling (Hund's case c) which one would normally expect only for high *n* Rydberg states. In the present study, which is restricted to the region below 11.8 eV, Rydberg series are observed up to n=3 and 4 members. Assignments have been largely made based on the calculated FRC quantum defect values reported by Cossart-Magos *et al.* [176]. It may be noted that the adiabatic ionization energies 12.89 and 12.91 eV from pulsed field ionization studies [200] are used throughout in the Rydberg series analysis.

6.3.3.1 THE nsσ RYDBERG SERIES

The first member of this series, *viz.*, $3s\sigma\,^{1,3}\Pi$ lies in the 7.7–8.7 eV region. The next higher members of this series, *viz.*, $4s\sigma\,^{3,1}\Pi$ are observed at 10.943 and 11.051 eV (*cf.* Fig. 6.3) with quantum defect values of 1.36 and 1.29 respectively. These states arise from the 2π→10σ orbital excitation and are theoretically predicted at 11.552 and 11.659 eV (*cf.* Table 6.3). The peak at 10.872 eV may be assigned to the hot band transition $2_1^0\,4s\sigma\,^3\Pi$ due to population of the ν_2'' bending mode at room temperature, where the double-prime denotes vibrational frequency of the lower electronic state. The corresponding hot band of the $4s\sigma\,^1\Pi$ transition at 10.965 eV appears as a shoulder to the intense $4s\sigma\,^3\Pi$ peak.

6.3.3.2 THE npσ AND npπ RYDBERG SERIES

The 3pσ configuration gives rise to the $3p\sigma\,^{3,1}\Pi$ states which are observed at 10.469 and 10.528 eV respectively with a quantum defect of ~0.6. The intensity of the triplet transition is considerably less than that of the corresponding singlet transition, thus indicating a weak spin-orbit coupling. These states can be identified with the theoretically predicted vertical excited states at 10.484 and 10.576 eV corresponding to the orbital excitation 2π→9σ. The assignment of the origin of the $3p\sigma\,^1\Pi$ transition in literature has been controversial. In some of the earlier REMPI works [178, 179], the 10.528 eV band has been assigned to $3_0^1\,3p\sigma\,^1\Pi$ with the origin of the Rydberg transition being located at 10.315 eV, whereas other workers [176, 183] have assigned the 10.528eV peak to the origin of $3p\sigma\,^1\Pi$. In the current photoabsorption study, the peak at 10.528 eV is observed to be the most intense in the entire 10.3–11.8eV region, whereas no line is observed at 10.315 eV at any of the pressures used, reaffirming the assignment of the origin to 10.528 eV. The large predicted oscillator strength (*cf.* Table 6.3) for the $3p\sigma\,^1\Pi$ transition supports the validity of this assignment. Two weak but distinct bands at 10.344 and 10.404 eV are observed to the lower wavenumber side of the strong 10.528 eV band, at relatively higher pressures. These bands are assigned to the hot band transitions $2_1^0\,3p\sigma\,^3\Pi$ and $2_2^0\,3p\sigma\,^3\Pi$ respectively. Vibronic bands corresponding to excitation of the ν_2' and ν_3' modes in the excited $3p\sigma\,^{3,1}\Pi$ states are observed at 10.596 eV, 10.681 eV and 10.751 eV as listed in Table 6.4, where the primes denote vibrational frequencies of the upper electronic state. The next pair of this series $4p\sigma\,^{3,1}\Pi$ appear at 11.741and 11.763 eV respectively with a quantum defect of ~0.55. Theoretically, the triplet component is predicted at 12.219 eV, while the singlet component is predicted at 13.940 eV, based on the orbital excitations involved. This discrepancy in experimental and theoretical values may be due to the spin-orbit coupling which is not accounted for in the theoretical model used.

The $3p\pi\,^1\Sigma^+$ state has been assigned to the strong and broad band observed at ~9.62 eV. The corresponding $3p\pi\,^3\Sigma^-$ state is assigned to a weak feature at 10.493 eV by Cossart-Magos *et al.* [176]. In the present study, no peak is observed at 10.493 eV. However, the $3p\pi\,^3\Sigma^-$ state is theoretically predicted at 10.693 eV, higher in energy than $3p\sigma\,^1\Pi$ by ~ 0.12 eV (*cf.* Table 6.3).Therefore the peak observed at 10.636 eV (*cf.* Figure 6) is assigned to $3p\pi\,^3\Sigma^-$. The obtained quantum defect of 0.55 confirms the assignment of this peak to a p state. It may be noted that this peak was not observed at all in the work by Cossart-Magos *et al.* [176], while other more intense spectral features in this region are reported as weak features by them. The next pair of this series, *viz.,* $4p\pi\,^1\Sigma^+$ and $4p\pi\,^3\Sigma^-$ are observed at 11.640 and 11.741 eV with quantum defects of 0.70 and 0.58 respectively. Correspondence of $4p\pi\,^3\Sigma^-$ to the theoretically predicted transition at 12.324 eV is straightforward. On the other hand, it is seen that $4p\pi\,^1\Sigma^+$ can be correlated with the theoretically predicted energies at 12.245 eV or 12.584 eV based on orbital excitations (*cf.* Table 2). As one goes to higher Rydberg states, complications due to multiple orbital excitations and spin-orbit interaction render unambiguous correspondence of experimental and theoretical values difficult.

6.3.3.3 THE ndσ, ndπ AND ndδ RYDBERG SERIES

There is considerable discrepancy in assignment of the 3d states in earlier works. Although Cossart-Magos *et al.* have predicted the 3dλ transitions to lie in the region ~11.2–11.5eV, they have not been able to experimentally identify any clear peaks [176]. In the present study, several clear and distinct peaks are observed in this region as seen in Figure 6.3. In the earlier REMPI-PES study by Scheper *et al.* [180], observed peaks at 11.318 and 11.337 eV have been assigned to $4s\sigma\,^{3,1}\Pi$. However, the theoretical calculations of Cossart-Magos *et al.* [176] suggest that this region corresponds to excitation to the 3d Rydberg series. Moreover, as explained by Scheper *et al.* [180], the PES experiments may not correctly predict the symmetry of the excited Rydberg state. Patsilinakou *et al.* [178] have assigned 3dλ (λ=σ, π, δ) origins to peaks at 10.841, 10.914 and 11.031 eV. This implies a quantum defect of ~0.29–0.42, which seems too high for a d state. Based on the calculated quantum defect values and the observed positions of the higher members (*n*=4, 5) [176], the five observed peaks in this region (11.380–11.476 eV) are assigned to singlet and triplet components of the 3dλ states as given in Table 5. The quantum defects obtained lie in the range –0.002 to –0.08, which is in agreement with the theoretical values of Cossart-Magos *et al.* [176], thus confirming the validity of the present assignments. Most of the remaining bands in this region could be assigned to vibronic features accompanying the Rydberg series 4sσ and 3dπ (*cf.* Table 6.4); however a few transitions in 11.2–11.8 eV remain unassigned. A clearer picture may emerge by performing studies at higher resolution or using better theoretical models.

6.3.3.4 VALENCE EXCITATIONS

The distinct feature observed at 10.840 eV has been reported in a few earlier works [170, 177, 178], however assignments made by these authors are not in agreement with each other. Assuming the FRC calculations of Cossart-Magos *et al.* [176] to be the best theoretical estimate of quantum defects available, these features cannot be satisfactorily assigned to any Rydberg transition. It is therefore concluded that this peak is a valence transition $X^1\Sigma^+ \rightarrow {}^1\Pi$ arising from the orbital excitation 7σ→3π*. This transition is theoretically predicted at 11.477 eV with a Λ value of 0.522, confirming its valence nature. The triplet component arising from this orbital excitation is predicted at 9.473 eV, which overlaps with the strong, broad peak at ~9.63 eV. It may be noted that these assignments are consistent with the prediction of valence transitions at $9.782\,({}^3\Pi)$ and $11.320\,({}^1\Pi)$ eV by Cossart-Magos *et al.* [176] although they have not reported any experimental peaks corresponding to these transitions.

CHAPTER 7

CONCLUSIONS AND FUTURE DIRECTION

7.1 CONCLUSIONS

This thesis presents the synchrotron radiation (SR) based gas phase VUV photoabsorption spectroscopy of dihalomethanes (CH_2X_2, CD_2X_2, X=Cl, Br, I), dimethyl sulphoxide (DMSO and DMSO-d_6) and nitrous oxide (N_2O). The knowledge of the excited electronic states of these molecules is important in the understanding of complex photochemical processes involving these molecules in the atmosphere. The spectroscopic studies in 1050–3000 Å region are carried out using two VUV beamlines, *viz.*, the Photophysics and High Resolution Ultraviolet (HRVUV) beamlines, at the Indus-1 SR source, RRCAT, Indore, India [4, 6, 8]. The spectra have been analyzed in detail to identify the valance, Rydberg and mixed valence/Rydberg states together with the vibronic structures associated with them. The spectral analysis is supported by DFT, MP2, and TDDFT calculations performed using GAMESS (US) [19] computational chemistry code.

The electronic absorption spectroscopy of diiodomethane (CH_2I_2) in the region 30,000–95,000 cm^{-1} (3.7–11.8 eV) is discussed in Chapter 2. The experimentally observed spectrum is discussed in the light of TDDFT calculations to obtain better understanding of the Rydberg/valence nature of the excitations and their interactions. The VUV spectrum is assigned to Rydberg transitions converging to the first four ionization potentials (IPs) at 9.46, 9.76, 10.21 and 10.56 eV [70] based on a quantum defect analysis. Quantum defect values obtained are consistent with excitation from iodine lone pair orbitals [75]. Vertical excited states computed by TDDFT method are assigned to the experimentally observed bands on the basis of the initial and final molecular orbitals involved. Lambda diagnostic values help in identifying the excited states as Rydberg or valence. Observed vibronic features are assigned based on computations of equilibrium geometries and vibrational frequencies in the neutral and cationic ground states. Vibronic features accompanying the $2b_1 \rightarrow 6s$, $3b_2 \rightarrow 6p$, $2b_1 \rightarrow 6p$ and $2b_1 \rightarrow 5d$ transitions are mainly due to excitation of the C–I symmetric stretch (ν_3') and CH_2 wag (ν_8') modes, with some smaller contribution from the C–H symmetric stretch (ν_1'). Spectral assignments are confirmed by comparison with the electronic absorption spectrum of CD_2I_2. The photoabsorption spectrum in the UV region is reinvestigated with the help of TDDFT predicted vertical excited states and excited state potential energy curves of the first few singlet excited states with respect to C–I bond. Some of the discrepancies in earlier work [42] are clarified and the UV absorption bands are assigned to low lying valence states 1^1B_2, 1^1B_1, 2^1A_1, 3^1A_1, 2^1B_1 and 2^1B_2. The unusually high underlying intensity in parts of the VUV spectrum is attributed to valence states with high oscillator strength. To the best of knowledge this is the first report of the VUV spectrum of CH_2I_2 in the region 50,000–66,666 cm^{-1} region and the first spectral analysis of the VUV spectrum in the 50,000–85,000 cm^{-1} region. This is also the first report of the VUV photoabsorption spectrum of CD_2I_2. The consolidated VUV photoabsorption study and considerable amount of new spectral data presented here are expected to be very useful in future studies of this molecule and its role in atmospheric chemistry.

The photoabsorption spectroscopy of dibromomethane in the energy region 35,000–95,000 cm^{-1} (4.3–11.8 eV) is reported in Chapter 3. The spectrum in the VUV region is dominated by Rydberg series converging to first four IPs at 10.52, 10.74, 11.21 and 11.30 eV

[85]. Quantum defect analysis is used to assign *ns*, *np* and *nd* Rydberg series originating from the four outermost ($3b_2$, $2b_1$, $1a_2$, $4a_1$) orbitals of CH_2Br_2. The analysis is further supported using quantum chemical calculations at PBE0/aug-cc-pV5Z level, which provide an overall good agreement with the experimental values. Earlier assignments of *ns* series are revised, and *np* and *nd* Rydberg series are assigned for the first time [88]. The underlying intensity in the photoabsorption spectrum is attributed to valence or valence-Rydberg mixed type transitions as obtained from TDDFT calculations. Observed vibrational features associated with 5p and 4d Rydberg states are assigned to totally symmetric (a_1) –CBr symmetric stretch mode (ν_3) of $3b_2$, $2b_1$, $1a_2 \rightarrow 5p$ and $3b_2$, $2b_1 \rightarrow 4d$ Rydberg states in contrast to the earlier assignments of ν_3 and $–CH_2$ bend (ν_2) [88]. Proposed assignments are confirmed by the UV-VUV photoabsorption spectrum of the diboromomethane-d_2 (CD_2Br_2) whose spectrum is reported here for the first time. This chapter presents a consolidated analysis of the UV-VUV photoabsorption spectrum of dibromomethane, which would serve as a useful basis for further photochemical studies of this molecule.

In Chapter 4, the photoabsorption spectrum of dichloromethane in the energy region 50,000–95,000 cm^{-1} (6.2–11.8 eV) is investigated. Analysis of the experimental spectrum is supported by TDDFT calculations of excited states at the PBE0/aug-cc-pV5Z level and potential energy curves of the first few singlet excited states with respect to C–Cl bond. The lowest absorption band in the region from 50,000 to 60,000 cm^{-1} is attributed mainly to the 1^1B_2 state with smaller contributions from the 1^1B_1 and 2^1A_1 states. In the region above 60,000 cm^{-1}, most of the observed bands are assigned to *ns*, *np* and *nd* type Rydberg series originating from the four outermost ($3b_1$, $2b_2$, $1a_2$ and $4a_1$) orbitals of CH_2Cl_2 and converging to first four IPs at 11.320, 11.357, 12.152 and 12.271 eV [131]. Vertical excited states computed by the TDDFT method are correlated with the experimentally observed bands on the basis of initial and final molecular orbitals involved in the transition. TDDFT predicted lambda diagnostic values help in identifying the excited states as Rydberg, valence or mixed type. In several sub-regions, the Rydberg peaks appear to ride on an underlying intensity, which could be satisfactorily explained by valence or valence-Rydberg mixed type transitions with high oscillator strengths. Observed vibronic features are assigned with the help of computations of equilibrium geometries and vibrational frequencies in the neutral and cationic ground states. The dominant vibrational mode accompanying the Rydberg transitions is the CCl symmetric stretch mode (ν_3). In the present work, extensive progressions of ν_3' bands are observed which could be conclusively assigned to the $2b_1$, $3b_2 \rightarrow 4p$ Rydberg transitions, in contrast to earlier work [118, 119] wherein the Rydberg series origins associated with these progressions had not been assigned. Additionally, a single excitation of the ν_3' mode appears with $1a_2 \rightarrow 4p$ as well as $3b_2 \rightarrow 5p$. The ν_1' (CH symmetric stretch) and ν_2' (CH_2 bend) modes are excited only in the $2b_1 \rightarrow 5s$ transition, while the ν_8' (CH_2 wag) mode is seen along with $2b_1 \rightarrow 5s$, $2b_1 \rightarrow 5p$ and $3b_2 \rightarrow 5p$. Proposed assignments are confirmed by the VUV photoabsorption spectrum of the dichloromethane-d_2 (CD_2Cl_2) which is reported here for the first time. We believe that the consolidated VUV photoabsorption study of dichloromethane presented here will contribute significantly to the understanding of its excited state structure and photochemistry.

At this juncture, it is worthwhile to compare the observations in respect of the VUV photoabsorption spectra of dihalomethanes (CH_2X_2, X = I, Br, Cl). Quantum defect values for the *ns*, *np* and *nd* series obtained in each of these molecules are close to the corresponding values for the halogen atom, thus indicating that these Rydberg series originate from the halogen lone pair non-bonding orbitals in all three cases. As we move down this series, from lighter to heavier (Cl to I), the energy separation between the first four IPs progressively decreases, which leads to severe overlap of the Rydberg series and makes their assignments more complicated. In all three molecules, low lying electronic transitions as well as anomalously high intensities observed in the region of the Rydberg series are attributed to valence transitions with the help of theoretically predicted energies. Vibronic bands accompanying some of the electronic transitions are observed in all three dihalomethanes, with the richest structure being seen in CH_2Cl_2 (CD_2Cl_2). It is interesting to note that in CH_2Br_2 (CD_2Br_2); only the ν_3 mode is observed, while in CH_2I_2 (CD_2I_2) and CH_2Cl_2 (CD_2Cl_2), additionally there are contributions from ν_1, ν_2 and ν_8 modes. The major contribution to vibronic structure is from ν_3 which appears in all three molecules and tends to form long progressions. Assuming that the vibrational frequencies in these excited (Rydberg) states are close to the corresponding ionic frequencies, one would expect a C–X (X=I, Br, Cl) bond lengthening in the cationic ground state. However, from the optimized geometries of all the dihalomethanes, it can be seen that the bond lengths remain almost the same while the bond angles change appreciably in going from neutral to ionic ground states. One possible explanation for this could be that the excited states in question have valence-Rydberg mixed nature or are involved in vibronic interactions with other nearby levels. It is also to be noted that the effect of spin-orbit interactions in the spectra, which become more important as we move from Cl to I has not been explicitly considered in the present analysis.

VUV photoabsorption studies of DMSO-h_6 and DMSO-d_6 in the 35,000–80,000 cm^{-1} region and associated VU/VUV photodissociation processes are presented in Chapter 5. The overall spectral features observed for DMSO-h_6 are in good agreement with earlier work, while the VUV photoabsorption spectrum of DMSO-d_6 is reported here for the first time. The observed absorption spectral features are analyzed and interpreted in terms of valence transitions and Rydberg series converging to the first three IPs at 9.10, 10.10 and 12.13 eV

[146]. Rydberg series are extended to higher members as compared to earlier works [132, 136]. Analysis is aided by quantum chemical calculations. The three sub-regions in which vibronic structure is observed are re-examined by comparison of the spectra of the two isotopologues. Since the vibronic structure in DMSO-d_6 is partly smeared out, photoabsorption studies at higher resolution are taken up. In this case, instead of the photoabsorption features of DMSO, completely different spectral features are observed. Most of these features could be identified and assigned to electronic or vibronic transitions of the SO radical [152-154]. It is concluded that SO is prominently produced in the UV-VUV photodissociation of DMSO brought about by the intense broadband radiation incident on the sample in the experimental configuration used. Further detailed ab initio calculations and high resolution studies would be required to gain a better understanding of the excited state structure and dissociation dynamics of DMSO. The results presented here could provide the impetus for future such studies on this molecule.

Photoabsorption studies of nitrous oxide in the VUV region 8.9–11.8 eV are presented in Chapter 6. The analysis of the spectrum is carried out with the help of quantum chemical calculations of vertical excited state energies in order to gain a better understanding of the excited state structure. The observed spectrum consists of a few valence transitions and several Rydberg series (n=3, 4) converging to the two spin orbit components $({}^2\Pi_{3/2,1/2})$ of the ground state of N_2O^+. In this region, the comprehensive experimental data supported by extensive theoretical calculations have resulted in unambiguous assignments and clarification of discrepancies in earlier work. The broad and intense $3p\pi\,{}^1\Sigma^+$ transition at ~9.62 eV is proposed to have a mixed valence-Rydberg character, explaining its unusually high quantum defect value of 0.96. In the 10.4–11.8 eV region dominated by Rydberg series, several features are observed and assigned for the first time. The Rydberg state $3p\pi\,{}^3\Sigma^-$ at 10.636 eV, the valence transition $7\sigma\rightarrow3\pi\,(^1\Pi)$ at 10.840eV and the Rydberg series 3dλ in the 11.37–11.48eV region are assigned for the first time as well as several accompanying vibronic transitions. The intensity of singlets and triplets being comparable for most of the observed Rydberg states leads to the conclusion that the spin-orbit coupling is quite large in Rydberg states of N_2O, even for low *n* (3, 4). These results are a step towards understanding the excited state structure of this environmentally important molecule.

7.2 FUTURE DIRECTION

Knowledge of the excited electronic states of polyatomic molecules is crucial to the understanding of several phenomena encountered in physics, chemistry and biology. In particular, it is indispensable in the studies of complex photophysical and photochemical processes taking place in the environment; the issue that has taken centre stage owing to the current concerns regarding the atmospheric pollution, ozone depletion and global warming.

In this thesis we have investigated VUV spectroscopy of molecules that are of significant interest in environmental sciences. The dihalomethane family of molecules (CH_2I_2, CH_2Br_2, CH_2Cl_2) has been recognized as an important contributor to the formation of aerosols, ozone balance in the atmosphere, and global warming. Dimethyl sulphoxide, an organo-sulphur compound, plays an important role in suphur balance in the atmosphere. Nitrous oxide is considered to be the single largest anthropogenic threat to the ozone layer with a very high global warming potential. The consolidated UV-VUV photoabsorption study and considerable amount of new spectral data presented in this thesis are expected to be very useful in future studies of these molecules and their role in atmospheric chemistry.

At the fundamental level, the molecules investigated in this thesis belong to different symmetry groups, C_{2v}, C_s and $C_{\infty v}$ for dihalomethanes, DMSO and N_2O respectively. The study thus provides a perspective of the excited state spectroscopy of different polyatomic molecules, non-linear as well as linear. The work has resulted in clarifying several issues relating to the nature of the excited states, Rydberg and valence transitions, vibronic assignments, etc. for these molecules. Understanding of a few unresolved issues pertaining to the electronic and vibronic structure of the dihalomethanes would benefit greatly from a detailed comparison of the similarities, differences and trends observed in the VUV spectra of each of the dihalomethanes, obtained with higher resolution experiments and higher level quantum chemical calculations. The experimental and theoretical methodologies developed and used here are general enough, and they can be conveniently adopted for similar studies on other molecular systems.

Future scope of the current work also includes improvements in the resolution of the recorded spectrum. The spectra reported in this thesis are obtained for gaseous samples at room temperature. There is a merit in conducting these studies in jet cooled molecular samples, which can simplify the spectral congestion by eliminating the contributions from higher vibrational levels. Also important to note here that while SR provides an intense and continuously tunable source, the resolution available with the current beamlines on Indus-1 is 0.5 Å (HRVUV beamline) and 1.5 Å (Photophysics beamline). While improvement in the resolution of the beamlines is important, the experimental techniques that use narrowband lasers in conjunction with SR will be of significant advantage in extending the current work in the high resolution domain.

Finally, the spectroscopy of highly excited states of molecules is inherently connected to the processes such as dissociation, ionization and fragmentations. Combining the energetics of molecules with their VUV spectra is ultimately the way forward in molecular physics. In our photoabsorption studies on DMSO, we could infer the presence of SO as a photodissociation product. Detailed studies of such kind would need techniques such as photoelectron-photoion coincidence spectroscopy, mass analyzed threshold ionization spectroscopy, zero kinetic energy spectroscopy etc. Efforts are currently on to extend the present work in this direction.

REFERENCES

1. N. J. Mason, A. Dawes, R. Mukerji, E. A. Drage, E. Vasekova, S. M. Webb and P. Limão-Vieira, *Atmospheric chemistry with synchrotron radiation*, J. Phys. B At. Mol. Opt. Phys. **38**, S893 (2005).
2. Y. Hatano, *Spectroscopy and dynamics of molecular superexcited states. Aspects of primary processes of radiation chemistry*, Rad. Phys. Chem. **67**, 187 (2003).
3. S. P. McGlynn, G. L. Findley, and R. H. Huebner (ed.), *Photophysics of Highly-Excited States*, Springer Netherlands, (1985).
4. D. Angal-Kalinin, A. Banerji, P. R. Hannurkar, M. G. Karmarkar, S. Kotaiah, S. P. Mhaskar, P. K. Nema, S. S. Prabhu, M. P. Kumar and S. S. Ramamurthi, *Synchrotron radiation source Indus-1*, Curr. Sci. **82**, 283 (2002).
5. S. S. Ramamurthi and G. Singh, *Status of the Indus-1 SR source*, Nucl. Instr. Meth. Phys. Res. A **359**, 15 (1995).
6. P. M. R. Rao, N. C. Das, B. N. Raja Sekhar, S. Padmanabhan, A. Shastri, S. S. Bhattacharya and A. P. Roy, *Photophysics beamline at Indus-1*, Nucl. Instr. Meth. Phys. Res. A **467–468**, 613 (2001).
7. N. C. Das, B. N. Raja Sekhar, P. Saraswathy, A. Shastri, S. S. Bhattacharya, S. Bhatt, A. K. Sinha and V. C. Sahni, *Development of Photophysics beamline at Indus-1 synchrotron radiation source*, J. Opt. (Ind.) **32**, 169 (2003).
8. P. J. Singh, A. Shastri, R. Sampath Kumar, S. N. Jha, S. V. N. B. Rao, R. D'Souza and B. N. Jagatap, *First commissioning results from high resolution vacuum ultraviolet beamline at Indus-1 synchrotron source*, Nucl. Instr. Meth. Phys. Res. A **634**, 113 (2011).
9. J. M. Hollas, *Modern Spectroscopy*, Wiley, Chichester (2004).
10. F. A. Cotton, *Chemical Applications of Group Theory*, Wiley, Chichester (2008).
11. G. Herzberg, *Molecular Spectra and Molecular Structure, Vol III. Electronic Spectra and Electronic Structure of Polyatomic Molecules*, D. van Nostrand, New Jersey (1966).
12. C. Sándorfy, *The Role of Rydberg States in Spectroscopy and Photochemistry*, Kluwer Academic, New York (2002).
13. M. B. Robin, *Higher Excited States of Polyatomic Molecules, Vol. 3*, Academic Press, New York (1985).
14. M. B. Robin, *Higher Excited States of Polyatomic Molecules, Vol. 1*, Academic Press, New York (1974).
15. C. Sándorfy, *Rydberg states in chemistry*, Int. J. Quant. Chem. **19**, 1147 (1981).

16. A. Shastri, P. J. Singh, B. N. Raja Sekhar, R. D'Souza and B. N. Jagatap, *The role of torsional modes in the electronic absorption spectrum of acetone,* J. Quant. Spectrosc Rad. Transfer **113**, 1553 (2012).

17. P. J. Singh, A. Shastri, B. N. Raja Sekhar, R. D'Souza and B. N. Jagatap, *Effect of isotopic substitution in the electronic absorption spectrum of acetone: VUV photoabsorption studies of acetone-*d_6, J. Quant. Spectrosc. Rad. Transfer **114**, 20 (2013).

18. P. J. Singh, A. Shastri, R. D’Souza and B. N. Jagatap, *Rydberg states of chloroform studied by VUV photoabsorption spectroscopy,* J. Quant. Spectrosc. Rad. Transfer **129**, 204 (2013).

19. M. W. Schmidt, K. K. Baldridge, J. A. Boatz, S. T. Elbert, M. S. Gordon, J. H. Jensen, S. Koseki, N. Matsunaga, K. A. Nguyen, S. Su, T. L. Windus, M. Dupuis and J. A. Montgomery, *General atomic and molecular electronic structure system,* J. Comp. Chem. **14**, 1347 (1993).

20. B. M. Bode and M. S. Gordon, *Macmolplt: a graphical user interface for GAMESS,* J. Mol. Graph. Modelling **16**, 133 (1998).

21. P. Atkins and R. Friedman, *Molecular Quantum Mechanics*, Oxford, New York (2009).

22. N. N. Matsuzawa, A. Ishitani, D. A. Dixon and T. Uda, *Time-dependent density functional theory calculations of photoabsorption Spectra in the vacuum ultraviolet region,* J. Phys. Chem. A **105**, 4953 (2001).

23. M. A. L. Marques and E. K. U. Gross, *Time-dependent density functional theory,* Annu. Rev. Phys. Chem. **55**, 427 (2004).

24. K. Burke and L. O. Wagner, *DFT in a nutshell,* Int. J. Quantum Chem. **113**, 96 (2013).

25. C. Lee, W. Yang and R. G. Parr, *Development of the Colle-Salvetti correlation-energy formula into a functional of the electron density,* Phys. Rev. B **37**, 785 (1988).

26. A. Dreuw and M. Head-Gordon, *Single-reference ab initio methods for the calculation of excited states of large molecules,* Chem. Rev. **105**, 4009 (2005).

27. E. Runge and E. K. U. Gross, *Density-functional theory for time-dependent systems,* Phys. Rev. Lett. **52**, 997 (1984).

28. P. Hohenberg and W. Kohn, *Inhomogeneous electron gas,* Phys. Rev. **136**, B864 (1964).

29. C. A. Ullrich and Z.-h. Yang, *A brief compendium of time-dependent density functional theory,* Brazilian J. Phys. **44**, 154 (2014).

30. P. Elliott, F. Furche and K. Burke, *Excited states from time-dependent density functional theory,* Rev. Comp. Chem. **26**, 91 (2009).

31. I. Ciofini and C. Adamo, *Accurate evaluation of valence and low-lying Rydberg states with standard time-dependent density functional theory,* J. Phys. Chem. A **111**, 5549 (2007).

32. M. J. G. Peach, P. Benfield, T. Helgaker and D. J. Tozer, *Excitation energies in density functional theory: An evaluation and a diagnostic test,* J. Chem. Phys. **128**, 044118 (2008).

33. M. M. Francl, W. J. Pietro, W. J. Hehre, J. S. Binkley, M. S. Gordon, D. J. DeFrees and J. A. Pople, *Self-consistent molecular orbital methods. XXIII. A polarization-type basis set for second-row elements,* J. Chem. Phys. **77**, 3654 (1982).

34. F. Jensen, *Introduction to Computational Chemistry*, Wiley, Chinchester (2007).

35. I. N. Levine, *Quantum Chemistry*, Pearson, New Jersey (2009).

36. T. H. Dunning, *Gaussian basis sets for use in correlated molecular calculations. I. The atoms boron through neon and hydrogen,* J. Chem. Phys. **90**, 1007 (1989).

37. D. E. Woon and T. H. Dunning, *Gaussian basis sets for use in correlated molecular calculations. III. The atoms aluminum through argon,* J. Chem. Phys. **98**, 1358 (1993).

38. J. C. Mössinger, D. E. Shallcross and A. R. Cox, *UV-VIS absorption cross-sections and atmospheric lifetimes of* CH_2Br_2*,* CH_2I_2 *and* CH_2BrI*,* J. Chem. Soc., Faraday Trans. **94**, 1391 (1998).

39. T. J. Johnson, T. Masiello and S. W. Sharpe, *The quantitative infrared and NIR spectrum of* CH_2I_2 *vapor: vibrational assignments and potential for atmospheric monitoring,* Atmos. Chem. Phys. **6**, 2581 (2006).

40. H. Xu, Y. Guo, S. Liu, X. Ma, D. Dai and G. Sha, *Photodissociation dynamics of* CH_2I_2 *molecules in the ultraviolet range studied by ion imaging,* J. Chem. Phys. **117**, 5722 (2002).

41. W. M. Kwok and D. L. Phillips, *Solvation and solvent effects on the short-time photodissociation dynamics of* CH_2I_2 *from resonance Raman spectroscopy,* J. Chem. Phys. **104**, 2529 (1996).

42. H. Okabe, M. Kawasaki and Y. Tanaka, *The photodissociation of* CH_2I_2*: Production of electronically excited* I_2*,* J. Chem. Phys. **73**, 6162 (1980).

43. M. Ito, P.-k. C. Huang and E. M. Kosower, *Electronic absorption spectra of iodo- and bromomethanes,* Trans. Faraday Soc. **57**, 1662 (1961).

44. M. Kawasaki, S. J. Lee and R. Bersohn, *Photodissociation of molecular beams of methylene iodide and iodoform,* J. Chem. Phys. **63**, 809 (1975).

45. B. P. Tsai, T. Baer, A. S. Werner and S. F. Lin, *Photoelectron-photoion coincidence study of the ionization and fragment appearance potentials of bromo- and iodomethanes,* J. Phys. Chem. **79**, 570 (1975).

46. P. M. Kroger, P. C. Demou and S. J. Riley, *Polyhalide photofragment spectra. I. Two-photon two-step photodissociation of methylene iodide,* J. Chem. Phys. **65**, 1823 (1976).

47. S. L. Baughcum and S. R. Leone, *Photofragmentation infrared emission studies of vibrationally excited free radicals* CH_3 *and* CH_2I, J. Chem. Phys. **72**, 6531 (1980).

48. J. B. Koffend and S. R. Leone, *Tunable laser photodissociation: quantum yield of* $I(^2P_{1/2})$ *from* CH_2I_2, Chem. Phys. Lett. **81**, 136 (1981).

49. W. H. Pence, S. L. Baughcum and S. R. Leone, *Laser UV photofragmentation of halogenated molecules. Selective bond dissociation and wavelength-specific quantum yields for excited iodine* $(^2P_{1/2})$ *and bromine* $(^2P_{1/2})$ *atoms,* J. Phys. Chem. **85**, 3844 (1981).

50. C. Fotakis, M. Martin and R. J. Donovan, *Ultraviolet laser multiphoton excitation of* CH_2I_2, J. Chem. Soc., Faraday Trans. 2, Mol. Chem. Phys. **78**, 1363 (1982).

51. T. F. Hunter and K. S. Kristjansson, *Yield of* $I(^2P)$ *in the photodissociation of* CH_2I_2, Chem. Phys. Lett. **90**, 35 (1982).

52. J. Zhang and D. G. Imre, CH_2I_2 *photodissociation: Emission spectrum at 355 nm,* J. Chem. Phys. **89**, 309 (1988).

53. U. Marvet, Q. Zhang, E. J. Brown and M. Dantus, *Femtosecond dynamics of photoinduced molecular detachment from halogenated alkanes. I. Transition state dynamics and product channel coherence,* J. Chem. Phys. **109**, 4415 (1998).

54. X. Zheng and D. L. Phillips, *Solvation can open the photoisomerization pathway for the direct photodissociation reaction of diiodomethane: Transient resonance Raman observation of the isodiiodomethane photoproduct from ultraviolet excitation of diiodomethane in the solution phase,* J. Phys. Chem. A **104**, 6880 (2000).

55. C. M. Cheatum, M. M. Heckscher, D. Bingemann and F. F. Crim, CH_2I_2 *fundamental vibrational relaxation in solution studied by transient electronic absorption spectroscopy,* J. Chem. Phys. **115**, 7086 (2001).

56. A. F. Lago, J. P. Kercher, A. Bödi, B. Sztáray, B. Miller, D. Wurzelmann and T. Baer, *Dissociative photoionization and thermochemistry of dihalomethane compounds studied by threshold photoelectron photoion coincidence spectroscopy,* J. Phys. Chem. A **109**, 1802 (2005).

57. J. Davidsson, J. Poulsen, M. Cammarata, P. Georgiou, R. Wouts, G. Katona, F. Jacobson, A. Plech, M. Wulff, G. Nyman and R. Neutze, *Structural determination of a transient isomer of* CH_2I_2 *by picosecond x-ray diffraction,* Phys. Rev. Lett. **94**, 245503 (2005).

58. H. Okabe, *Photochemistry of Small Molecules,* Wiley, New York (1978).

59. S. Roszak, W. S. Koski, J. J. Kaufman and K. Balasubramanian, *Structures and electron attachment properties of halomethanes (CX_nY_m , X = H, F; Y = Cl, Br, I; n = 0,4; m = 4–n),* SAR QSAR Env. Res. **11**, 383 (2001).

60. J. Zhang, E. J. Heller, D. Huber, D. G. Imre and D. Tannor, *CH_2I_2 photodissociation: Dynamical modeling,* J. Chem. Phys. **89**, 3602 (1988).

61. X. Zheng and D. L. Phillips, *Density functional theory and resonance Raman investigation of the ultraviolet electronic excited states of CF_2I_2,* Chem. Phys. Lett. **316**, 524 (2000).

62. M. Odelius, M. Kadi, J. Davidsson and A. N. Tarnovsky, *Photodissociation of diiodomethane in acetonitrile solution and fragment recombination into iso-diiodomethane studied with ab initio molecular dynamics simulations,* J. Chem. Phys. **121**, 2208 (2004).

63. Y.-J. Liu, L. De Vico, R. Lindh and W.-H. Fang, *Spin-orbit ab initio investigation of the ultraviolet photolysis of diiodomethane,* ChemPhysChem **8**, 890 (2007).

64. J. P. Perdew, K. Burke and M. Ernzerhof, *Generalized gradient approximation made simple,* Phys. Rev. Lett. **77**, 3865 (1996).

65. A. D. Becke, *Density-functional thermochemistry. III. The role of exact exchange,* J. Chem. Phys. **98**, 5648 (1993).

66. K. A. Peterson, D. Figgen, E. Goll, H. Stoll and M. Dolg, *Systematically convergent basis sets with relativistic pseudopotentials. II. Small-core pseudopotentials and correlation consistent basis sets for the post-d group 16–18 elements,* J. Chem. Phys. **119**, 11113 (2003).

67. K. A. Peterson, B. C. Shepler, D. Figgen and H. Stoll, *On the spectroscopic and thermochemical properties of ClO, BrO, IO, and their anions,* J. Phys. Chem. A **110**, 13877 (2006).

68. D. Feller, *The role of databases in support of computational chemistry calculations,* J. Comp. Chem. **17**, 1571 (1996).

69. K. L. Schuchardt, B. T. Didier, T. Elsethagen, L. Sun, V. Gurumoorthi, J. Chase, J. Li and T. L. Windus, *Basis Set Exchange: A community database for computational sciences,* J. Chem. Info. Modelling **47**, 1045 (2007).

70. A. W. Potts, H. J. Lempka, D. G. Streets and W. C. Price, *Photoelectron spectra of the halides of elements in groups III, IV, V and VI,* Phil. Trans. Royal Soc. London A **268**, 59 (1970).

71. R. Manne, K. Wittel and B. S. Mohanty, *Spin-orbit interaction in molecular photoelectron spectra. An intermediate coupling approach,* Mol. Phys. **29**, 485 (1975).

72. R. N. Dixon, J. N. Murrell and B. Narayan, *The photoelectron spectra of the halomethanes,* Mol. Phys. **20**, 611 (1971).

73. S. A. Kudchadker and A. P. Kudchadker, *Ideal gas thermodynamic properties of the eight bromo- and iodomethanes,* J. Phys. Chem. Ref. Data **4**, 457 (1975).

74. T. A. Ford, *Infrared and Raman spectra and vibrational assignments of diiodomethane and its deuterated analogs,* J. Mol. Spectrosc. **58**, 185 (1975).

75. M. Eypper, F. Innocenti, A. Morris, S. Stranges, J. B. West, G. C. King and J. M. Dyke, *Photoionization of iodine atoms: Rydberg series which converge to the* $I^+(^1S_0)\leftarrow I(^2P_{3/2})$ *threshold,* J. Chem. Phys. **132**, 244304 (2010).

76. A. Gedanken and M. D. Rowe, *Magnetic circular dichroism of iodoform and methylene iodide,* Chem. Phys. **36**, 181 (1979).

77. K. D. Goodwin, M. E. Lidstrom and R. S. Oremland, *Marine bacterial degradation of brominated methanes,* Env. Sci. Tech. **31**, 3188 (1997).

78. Q. Liang, R. S. Stolarski, S. R. Kawa, J. E. Nielsen, A. R. Douglass, J. M. Rodriguez, D. R. Blake, E. L. Atlas and L. E. Ott, *Finding the missing stratospheric* Br_y*: A global modeling study of* $CHBr_3$ *and* CH_2Br_2*,* Atmos. Chem. Phys. **10**, 2269 (2010).

79. L. T. Molina, M. J. Molina and F. S. Rowland, *Ultraviolet absorption cross sections of several brominated methanes and ethanes of atmospheric interest,* J. Phys. Chem. **86**, 2672 (1982).

80. J. Huang, D. Xu, W. H. Fink and W. M. Jackson, *Photodissociation of the dibromomethane cation at 355 nm by means of ion velocity imaging,* J. Chem. Phys. **115**, 6012 (2001).

81. L. Ji, Y. Tang, R. Zhu, Z. Wei and B. Zhang, *Photodissociation dynamics of* CH_2Br_2 *near 234 and 267 nm,* Spectrochimica Acta A, Mol. Biomol. Spectrosc. **67**, 273 (2007).

82. L. Ji, Y. Tang, R. Zhu, B. Tang and B. Zhang, *Studies on photodissociation of dibromoalkane in UV region,* Chem. Phys. **314**, 173 (2005).

83. P. Sharma, R. K. Vatsa, D. K. Maity and S. K. Kulshreshtha, *Laser induced photodissociation of* CH_2Cl_2 *and* CH_2Br_2 *at 355 nm: An experimental and theoretical study,* Chem. Phys. Lett. **382**, 637 (2003).

84. P.-Y. Wei, Y.-P. Chang, W.-B. Lee, Z. Hu, H.-Y. Huang, K.-C. Lin, K. T. Chen and A. H. H. Chang, *248 nm photolysis of* CH_2Br_2 *by using cavity ring-down absorption spectroscopy:* Br_2 *molecular elimination at room temperature,* J. Chem. Phys. **125**, 133319 (2006).

85. N. Kishimoto, E. Matsumura, K. Ohno and M. S. Deleuze, *Collision-energy-resolved Penning ionization electron spectroscopy of bromomethanes (*CH_3Br*,*CH_2Br_2*, and* $CHBr_3$*) by collision with He* (*2^3S*) metastable atoms,* J. Chem. Phys. **121**, 3074 (2004).

86. D. Gillotay and P. C. Simon, *Ultraviolet absorption cross-sections of photoactive species of stratospheric interest. Part 1: The Halocarbons,* Aeronomica Acta A **356**, 1 (1990).

87. Y. Liu, H. Xiao, M. Sun and W. Fang, *Spin-orbit ab initio investigation of the photodissociation of dibromomethane in the gas and solution phases,* J. Comp. Chem. **29**, 2513 (2008).
88. G. C. Causley and B. R. Russell, *Vacuum ultraviolet absorption spectra of the bromomethanes,* J. Chem. Phys. **62**, 848 (1975).
89. M. J. Frisch, J. A. Pople and J. S. Binkley, *Self-consistent molecular orbital methods. XXV. Supplementary functions for Gaussian basis sets,* J. Chem. Phys. **80**, 3265 (1984).
90. K. Kuchitsu and G. G., *Structure of free polyatomic molecules: Basic data*, Springer, Berlin (1998).
91. R. S. Dennen, E. A. Piotrowski and F. F. Cleveland, *Raman and infrared spectral data for* CH_2Br_2*,* $CHDBr_2$*, and* CD_2Br_2*,* J. Chem. Phys. **49**, 4385 (1968).
92. R. Venkatraman, J. S. Kwiatkowski, G. Bakalarski and J. Leszczynski, *Molecular structure and IR spectra of bromomethanes by DFT and post-Hartree-Fock MP2 and CCSD(T) calculations,* Mol. Phys. **98**, 371 (2000).
93. Z. Kisiel, A. Kraśnicki, L. Pszczółkowski, S. T. Shipman, L. Alvarez-Valtierra and B. H. Pate, *Assignment and analysis of the rotational spectrum of bromoform enabled by broadband FTMW spectroscopy,* J. Mol. Spectrosc. **257**, 177 (2009).
94. C. E. Theodosiou, M. Inokuti and S. T. Manson, *Quantum defect values for positive atomic ions,* Atom. Data Nucl. Data Tables **35**, 473 (1986).
95. R. Koppmann (ed.), *Halogenated Volatile Organic Compounds*, Blackwell Publishing Ltd. (2007).
96. K. F. Alcantara, W. Wolff, A. H. A. Gomes, L. Sigaud, S. Soriano, V. Oliveira, A. B. Rocha and A. C. F. Santos, *Fragmentation of the* CH_2Cl_2 *molecule by proton impact and VUV photons,* J. Phys. B, At. Mol. Opt. Phys. **44**, 165205 (2011).
97. P. Fabian and O. N. Singh (ed.), *Reactive Chlorine Compounds in the Atmosphere,* Springer, Berlin (1999).
98. J. M. Lobert, W. C. Keene, J. A. Logan and R. Yevich, *Global chlorine emissions from biomass burning: Reactive chlorine emissions inventory,* J. Geophys. Res. Atmos. **104**, 8373 (1999).
99. T. E. Graedel and W. Keene, *The budget and cycle of Earth's natural chlorine,* Pure Appl. Chem. **68**, 1689 (1996).
100. A. S. Werner, B. P. Tsai and T. Baer, *Photoionization study of the ionization potentials and fragmentation paths of the chlorinated methanes and carbon tetrabromide,* J. Chem. Phys. **60**, 3650 (1974).
101. E. Tiemann, H. Kanamori and E. Hirota, *Diode laser spectroscopy for monitoring the yield of metastable Cl from photodissociation of simple molecules,* J. Chem. Phys. **88**, 2457 (1988).

102. Y. Matsumi, K. Tonokura, M. Kawasaki, G. Inoue, S. Satyapal and R. Bersohn, *Erratum: Fine structure branching ratios and Doppler spectroscopy of chlorine atoms from the photodissociation of alkyl chlorides and chlorofluoromethanes at 157 and 193 nm [J. Chem. Phys.* ***94****, 2669 (1991)],* J. Chem. Phys. **97**, 5261 (1992).

103. R. A. Brownsword, M. Hillenkamp, T. Laurent, R. K. Vatsa, H.-R. Volpp and J. Wolfrum, *Dynamics of H atom formation in the photodissociation of chloromethanes at 193.3 nm,* J. Phys. Chem. A **101**, 5222 (1997).

104. S.-Y. Chiang, M. Bahou, K. Sankaran, Y.-P. Lee, H.-F. Lu and M.-D. Su, *Dissociative photoionization of CH_2Cl_2 and enthalpy of formation of $CHCl^+$: Experiments and calculations,* J. Chem. Phys. **118**, 62 (2003).

105. R. Marom, A. Golan, S. Rosenwaks and I. Bar, *Photodissociation dynamics of vibrationally excited CH_2Cl_2 molecules,* Chem. Phys. Lett. **378**, 305 (2003).

106. R. Marom, A. Golan, S. Rosenwaks and I. Bar, *Intramolecular dynamics in the photofragmentation of initially vibrationally excited CH_2Cl_2,* J. Phys. Chem. A **108**, 8089 (2004).

107. F. Taketani, K. Takahashi and Y. Matsumi, *Quantum yields for $Cl(^2P_j)$ atom formation from the photolysis of chlorofluorocarbons and chlorinated hydrocarbons at 193.3 nm,* J. Phys. Chem. A **109**, 2855 (2005).

108. T. Alapi and A. Dombi, *Direct VUV photolysis of chlorinated methanes and their mixtures in an oxygen stream using an ozone producing low-pressure mercury vapour lamp,* Chemosphere **67**, 693 (2007).

109. H.-Y. Xiao, Y.-J. Liu, J.-G. Yu and W.-H. Fang, *Spin–orbit ab initio investigation of the photodissociation of CH_2Cl_2,* Chem. Phys. Lett. **436**, 75 (2007).

110. S. Hayakawa, T. Sasaki and H. Matsubara, *Dissociation mechanism of electronically excited CH_2X_2 (X= Cl, Br) formed by near-resonant neutralization using charge-inversion mass spectrometry,* Chem. Phys. Lett. **463**, 60 (2008).

111. J. Harvey, R. P. Tuckett and A. Bödi, *A halomethane thermochemical network from iPEPICO experiments and quantum chemical calculations,* J. Phys. Chem. A **116**, 9696 (2012).

112. J. Yu, W. Cai, J. Chen, L. Feng, Y. Jiang and Z. Cheng, *Conversion characteristics and mechanism analysis of gaseous dichloromethane degraded by a VUV light in different reaction media,* J. Env. Sci. **24**, 1777 (2012).

113. A. A. Gordus and R. B. Bernstein, *Isotope effect in continuous ultraviolet absorption spectra: Methyl bromide-d_3 and chloroform-d,* J. Chem. Phys. **22**, 790 (1954).

114. C. Hubrich and F. Stuhl, *The ultraviolet absorption of some halogenated methanes and ethanes of atmospheric interest,* J. Photochem. **12**, 93 (1980).

115. P. C. Simon, D. Gillotay, N. Vanlaethem-Meuree and J. Wisemberg, *Ultraviolet absorption cross-sections of chloro and chlorofluoro-methanes at stratospheric temperatures,* J. Atmos. Chem. **7**, 107 (1988).

116. C. R. Zobel and A. B. F. Duncan, *Vacuum ultraviolet absorption spectra of some halogen derivatives of methane. Correlation of the spectra,* J. Am. Chem. Soc. **77**, 2611 (1955).

117. H. Tsubomura, K. Kimura, K. Kaya, J. Tanaka and S. Nagakura, *Vacuum ultraviolet absorption spectra of saturated organic compounds with non-bonding electrons,* Bull. Chem. Soc. Jap. **37**, 417 (1964).

118. B. R. Russell, L. O. Edwards and J. W. Raymonda, *Vacuum ultraviolet absorption spectra of the chloromethanes,* J. Am. Chem. Soc. **95**, 2129 (1973).

119. L. C. Lee and M. Suto, *Fluorescence yields from photodissociative excitation of chloromethanes by vacuum ultraviolet radiation,* Chem. Phys. **114**, 423 (1987).

120. R. J. Berry and M. D. Harmony, *The use of scaled moments of inertia in experimental structure determinations of polyatomic molecules,* Struct. Chem. **1**, 49 (1990).

121. H.-W. Xi and M.-B. Huang, *The* 1^2B_2, 1^2B_1, 1^2A_1, 1^2A_2, *and* $3^2A'$ (2^2B_2) *states of the 1,1-dichloromethene ion studied using multiconfiguration second-order perturbation theory,* Chem. Phys. Lett. **425**, 28 (2006).

122. R. Escribano, J. M. Orza, S. Montero and C. Domingo, *Absolute Raman intensities, force constants, and electro-optical parameters of* CH_2Cl_2, CD_2Cl_2 *and* $CHDCl_2$, Mol. Phys. **37**, 361 (1979).

123. J. L. Duncan, G. D. Nivellini and F. Tullini, *Methylene chloride: The mid-infrared spectrum of an almost vibrationally unperturbed molecule,* J. Mol. Spectrosc. **118**, 145 (1986).

124. K. Takeshita, *A theoretical study on the ionic states and the photoelectron spectrum of dichloromethane* (CH_2Cl_2), Chem. Phys. **143**, 239 (1990).

125. F. Hopfgarten and R. Manne, *Molecular orbital interpretation of X-ray emission and photoelectron spectra: IV. Chloromethanes,* J. Elec. Spectrosc. Rel. Phen. **2**, 13 (1973).

126. S. Katsumata and K. Kimura, *Interpretation of photoelectron spectra of halomethanes,* Bull. Chem. Soc. Jap. **46**, 1342 (1973).

127. D. Li, J.-K. Zhu, J. Li and Y.-K. Pan, *Calculation of photoelectron spectra of chloromethanes,* Chem. Phys. Lett. **87**, 463 (1982).

128. W. von Niessen, L. Åsbrink and G. Bieri, *30.4 nm He (II) photoelectron spectra of organic molecules. Part VI. Halogeno-compounds (C, H, X; X = Cl, Br, I),* J. Elec. Spectrosc. Rel. Phen. **26**, 173 (1982).

129. D. Li, J.-K. Zhu, J.-Q. Li and Y.-K. Pan, *An SCF–Xα–MS study of the photoelectron spectra and electronic structures of methylene dihalides,* J. Elec. Spectrosc. Rel. Phen. **34**, 1 (1984).

130. R. Bohinc, M. Žitnik, K. Bučar, M. Kavčič, L. Journel, R. Guillemin, T. Marchenko, M. Simon and W. Cao, *Dissociation of chloromethanes upon resonant σ* excitation studied by x-ray scattering,* J. Chem. Phys. **139**, 134302 (2013).

131. T. Pradeep and D. A. Shirley, *High resolution photoelectron spectroscopy of CH_2F_2, CH_2Cl_2 and CF_2Cl_2 using supersonic molecular beams,* J. Elec. Spectrosc. Rel. Phen. **66**, 125 (1993).

132. E. A. Drage, P. Cahillane, S. V. Hoffmann, N. J. Mason and P. Limão-Vieira, *High resolution VUV photoabsorption cross section of dimethyl sulphoxide $(CH_3)_2SO$,* Chem. Phys. **331**, 447 (2007).

133. G. M. Thorson, C. M. Cheatum, M. J. Coffey and F. Fleming Crim, *Photofragment energy distributions and dissociation pathways in dimethyl sulfoxide,* J. Chem. Phys. **110**, 10843 (1999).

134. E. Bodo and G. Lanaro, *Theoretical treatment of the electronic excited states of the DMSO molecule: A challenge for current theoretical methods,* Chem. Phys. **377**, 136 (2010).

135. K. Gollnick and H.-U. Stracke, *Direct and sensitized photolysis of dimethyl sulphoxide in solution,* Pure Appl. Chem. **33**, 217 (1973).

136. K. H. Sze, C. E. Brion, M. Tronc, S. Bodeur and A. P. Hitchcock, *Inner and valence shell electronic excitation of dimethyl sulfoxide by electron energy loss and photoabsorption spectroscopies,* Chem. Phys. **121**, 279 (1988).

137. J. W. Cubbage and W. S. Jenks, *Computational studies of the ground and excited state potentials of DMSO and H_2SO: Relevance to photostereomutation,* J. Phys. Chem. A **105**, 10588 (2001).

138. V. P. Mondéjar, M. J. Yusá, I. G. Cuesta, A. M. J. S. de Merás and J. Sánchez-Marín, *Vertical excitation energies to valence states of DMS and DMSO,* Theor. Chem. Accounts **118**, 527 (2007).

139. T. H. Dunning, *Gaussian basis sets for use in correlated molecular calculations. I. The atoms boron through neon and hydrogen,* The Journal of Chemical Physics **90**, 1007 (1989).

140. D. E. Woon and T. H. Dunning, *Gaussian basis sets for use in correlated molecular calculations. III. The atoms aluminum through argon,* The Journal of Chemical Physics **98**, 1358 (1993).

141. C. Lee, W. Yang and R. G. Parr, *Development of the Colle-Salvetti correlation-energy formula into a functional of the electron density,* Physical Review B **37**, 785 (1988).

142. A. D. Becke, *Density-functional thermochemistry. III. The role of exact exchange,* The Journal of Chemical Physics **98**, 5648 (1993).

143. J. P. Perdew, K. Burke and M. Ernzerhof, *Generalized gradient approximation made simple,* Physical Review Letters **77**, 3865 (1996).

144. S. Patai, Z. Rappoport and C. J. Stirling, *The Chemistry of Sulfones and Sulphoxides,* John Wiley & Sons, (1988).

145. V. Typke and M. Dakkouri, *The force field and molecular structure of dimethylsulfoxide from spectroscopic and gas electron diffraction data,* J. Mol. Struct. **599**, 177 (2001).

146. K. Kimura, *Handbook of HeI Photoelectron Spectra of Fundamental Organic Molecules,* Japan Scientific Societies Press, Tokyo (1981).

147. X. Chen, F. Asmar, H. Wang and B. R. Weiner, *Nascent sulfur monoxide ($X^3\ \Sigma^-$) vibrational distributions from the photodissociation of sulfur dioxide, sulfonyl chloride, and dimethylsulfoxide at 193 nm,* The Journal of Physical Chemistry **95**, 6415 (1991).

148. X. Chen, H. Wang, B. R. Weiner, M. Hawley and H. Nelson, *Photodissociation of dimethyl sulfoxide at 193 nm in the gas phase,* J. Phys. Chem. **97**, 12269 (1993).

149. D. A. Blank, S. W. North, D. Stranges, A. G. Suits and Y. T. Lee, *Unraveling the dissociation of dimethyl sulfoxide following absorption at 193 nm,* J. Chem. Phys. **106**, 539 (1997).

150. H.-Q. Zhao, Y.-S. Cheung, D. P. Heck, C. Y. Ng, T. Tetzlaff and W. S. Jenks, *A 193-nm-laser photofragmentation time-of-flight mass spectrometric study of dimethylsulfoxide,* J. Chem. Phys. **106**, 86 (1997).

151. R. N. Rudolph, S. W. North, G. E. Hall and T. J. Sears, *Diode laser measurements of CD_3 quantum yields and internal energy for the dissociation of dimethyl sulfoxide-d_6,* J. Chem. Phys. **106**, 1346 (1997).

152. R. J. Donovan, D. Husain and P. T. Jackson, *Spectroscopic and kinetic studies of the SO radical and the photolysis of thionyl chloride,* Trans. Faraday Soc. **65**, 2930 (1969).

153. R. J. Donovan and D. J. Little, *Vacuum ultraviolet spectrum of the SO radical,* Spectrosc. Lett. **4**, 213 (1971).

154. C. P. Archer, J. M. F. Elks and C. M. Western, *The $C^3\Pi$, $d^1\Pi$, and $e^1\Pi$ states of SO,* J. Chem. Phys. **112**, 6293 (2000).

155. M. Barnes, J. Baker, J. M. Dyke, M. Feher and A. Morris, *An investigation of the SO ($X^3\Sigma^-$) molecule by multiphoton ionization spectroscopy,* Mol. Phys. **74**, 689 (1991).

156. W. C. Swope, Y. P. Lee and H. F. Schaefer, *Sulfur oxide: Low-lying bound molecular electronic states of SO,* J. Chem. Phys. **71**, 3761 (1979).

157. S. L. Manatt and A. L. Lane, *A compilation of the absorption cross-sections of* SO_2 *from 106 to 403 nm,* J. Quan. Spectrosc. Rad. Transfer **50**, 267 (1993).

158. J. M. Dyke, L. Golob, N. Jonathan, A. Morris, M. Okuda and D. J. Smith, *Vacuum ultraviolet photoelectron spectroscopy of transient species. Part 3. The* $SO(^3\Sigma^-)$ *radical,* J. Chem. Soc., Faraday Trans. 2 **70**, 1818 (1974).

159. J. M. Dyke, D. Haggerston, A. Morris, S. Stranges, J. B. West, T. G. Wright and A. E. Wright, *A study of the SO molecule with photoelectron spectroscopy using synchrotron radiation,* J. Chem. Phys. **106**, 821 (1997).

160. A. R. Ravishankara, J. S. Daniel and R. W. Portmann, *Nitrous oxide (*N_2O*): The dominant ozone-depleting substance emitted in the 21st century,* Science **326**, 123 (2009).

161. D. J. Wuebbles, *Nitrous oxide: No laughing matter,* Science **326**, 56 (2009).

162. H. Kawamata, H. Kohguchi, T. Nishide and T. Suzuki, *Photodissociation of nitrous oxide starting from excited bending levels,* J. Chem. Phys. **125**, 133312 (2006).

163. E. Bustos, A. M. Velasco, I. Martín and C. Lavín, *Photoabsorption of nitrous oxide through Rydberg states in the bound and continuum spectral regions: Main ionization channels,* J. Phys. Chem. A **106**, 35 (2001).

164. N. R. Carlon, D. K. Papanastasiou, E. L. Fleming, C. H. Jackman, P. A. Newman and J. B. Burkholder, *UV absorption cross sections of nitrous oxide (*N_2O*) and carbon tetrachloride (*CCl_4*) between 210 and 350 K and the atmospheric implications,* Atmos. Chem. Phys. **10**, 6137 (2010).

165. A. B. F. Duncan, *The far ultraviolet absorption spectrum of* N_2O*,* J. Chem. Phys. **4**, 638 (1936).

166. H. Sponer and E. Teller, *Electronic spectra of polyatomic molecules,* Rev. Mod. Phys. **13**, 75 (1941).

167. M. Zelikoff, K. Watanabe and E. C. Y. Inn, *Absorption coefficients of gases in the vacuum vltraviolet. Part II. Nitrous oxide,* J. Chem. Phys. **21**, 1643 (1953).

168. Y. Tanaka, A. S. Jursa and F. J. LeBlanc, *Higher ionization potentials of linear triatomic molecules. II.* CS_2*, COS, and* N_2O*,* J. Chem. Phys. **32**, 1205 (1960).

169. S. P. McGlynn, J. W. Rabalais, J. R. McDonald and V. M. Scherr, *Electronic spectoscopy of isoelectronic molecules. II. Linear triatomic groupings containing sixteen valence electrons,* Chem. Rev. **71**, 73 (1971).

170. J. Nee, J. Yang, P. Lee, X. Wang and C. Kuo, *Photoabsorption Cross Sections of* N_2O *in 100–220 nm,* Chin. J. Chem. Phys. **37**, 172 (1999).

171. P. von Hessberg, J. Kaiser, M. B. Enghoff, C. A. McLinden, S. L. Sorensen, T. Röckmann and M. S. Johnson, *Ultra-violet absorption cross sections of isotopically*

substituted nitrous oxide species: $^{14}N^{14}NO$, $^{15}N^{14}NO$, $^{14}N^{15}NO$ and $^{15}N^{15}NO$, Atmos. Chem. Phys. **4**, 1237 (2004).

172. K. Yoshino, D. E. Freeman and W. H. Parkinson, *High resolution absorption cross-section measurements of N_2O at 295–299 K in the wavelength region 170–222 nm,* Planetary Space Sci. **32**, 1219 (1984).

173. G. S. Selwyn and H. S. Johnston, *Ultraviolet absorption spectrum of nitrous oxide as a function of temperature and isotopic substitution,* J. Chem. Phys. **74**, 3791 (1981).

174. A. Shastri, K. Sunanda, P. J. Singh, B. R. Sekhar, S. B. Rao, R. D'Souza and B. Jagatap, *Excited state vibrational modes of a few triatomic molecules of environmental interest,* Asian J. Spectrosc. **0**, 121 (2012).

175. Z. Cheng, H. Ya-hua, Z. Xiao-guo and L. Shi-lin, *Dissociation dynamics of nitrous oxide from jet-cooling absorption spectrum in 142.5–147.5 nm,* Chin. J. Chem. Phys. **24**, 267 (2011).

176. C. Cossart-Magos, M. Jungen and F. Launay, *High resolution absorption spectrum of N_2O between 75,000 and 104,000 cm^{-1},* J. Chem. Phys. **114**, 7368 (2001).

177. L. C. Lee and M. Suto, *Production and quenching of excited photofragments of N_2O,* J. Chem. Phys. **80**, 4718 (1984).

178. E. Patsilinakou, R. T. Wiedmann, C. Fotakis and E. R. Grant, *Jet-resolved vibronic structure in the higher excited states of N_2O: Ultraviolet three-photon absorption spectroscopy from 80,000 to 90,000 cm^{-1},* J. Chem. Phys. **91**, 3916 (1989).

179. M. G. Szarka and S. C. Wallace, *Spectroscopy and photodissociation of Rydberg states of N_2O,* J. Chem. Phys. **95**, 2336 (1991).

180. C. R. Scheper, J. Kuijt, W. J. Buma and C. A. de Lange, *Resonance-enhanced multiphoton ionization photoelectron spectroscopy of Rydberg states of N_2O below the $X^2\Pi$ ionization limit,* J. Chem. Phys. **109**, 7844 (1998).

181. C. Maul, M. Poretskiy, A. Rakhymzhan and J. Grunenberg, *On the ultraviolet absorption of nitrous oxide and its van der Waals complexes,* J. Mol. Spectrosc. **256**, 80 (2009).

182. Y.-Y. Wang, J.-M. Sun and L.-F. Zhu, *Cross sections for the valence shell excitations of nitrous oxide studied by fast electron impact,* J. Chem. Phys. **132**, 124301 (2010).

183. K. England, T. Reddish and J. Comer, *Electron energy-loss studies of nitrous oxide in the energy range 10–20 eV,* Chem. Phys. **119**, 435 (1988).

184. Y.-W. Liu, Y.-Y. Wang and L.-F. Zhu, *Valence-shell excitations of nitrous oxide studied by fast electron impact,* Chin. Phys. Lett. **29**, 043302 (2012).

185. F. Wang and R. D. Harcourt, *Electronic structure study of the* N_2O *isomers using post-Hartree−Fock and density functional theory calculations,* J. Phys. Chem. A **104**, 1304 (2000).

186. R. Schinke, *Photodissociation of* N_2O*: Potential energy surfaces and absorption spectrum,* J. Chem. Phys. **134**, 064313 (2011).

187. G. C. McBane and R. Schinke, *Product angular distributions in the ultraviolet photodissociation of* N_2O*,* J. Chem. Phys. **136**, 044314 (2012).

188. R. Schinke and J. A. Schmidt, *Photodissociation of* N_2O*: Excitation of* $^1A''$ *states,* J. Phys. Chem. A **116**, 11083 (2012).

189. A. Brown, P. Jimeno and G. G. Balint-Kurti, *Photodissociation of* N_2O*. I. Ab initio potential energy surfaces for the low-lying electronic states* $\tilde{X}^1A'$, $2^1A'$, *and* $1^1A''$, J. Phys. Chem. A **103**, 11089 (1999).

190. S. Nanbu and M. S. Johnson, *Analysis of the ultraviolet absorption cross sections of six isotopically substituted nitrous oxide species using 3D wave packet propagation,* J. Phys. Chem. A **108**, 8905 (2004).

191. M. N. Daud, G. G. Balint-Kurti and A. Brown, *Ab initio potential energy surfaces, total absorption cross sections, and product quantum state distributions for the low-lying electronic states of* N_2O*,* J. Chem. Phys. **122**, 054305 (2005).

192. N. W. Winter, *Theoretical assignments of the electronic states of nitrous oxide,* Chem. Phys. Lett. **33**, 300 (1975).

193. D. G. Hopper, *Abinitio multiple root optimization MCSCF study of the* $C_{\infty v}/C_s$ *excitation spectra and potential energy surfaces of* N_2O*,* J. Chem. Phys. **80**, 4290 (1984).

194. I. Martín, A. M. Velasco, C. Lavín, E. Olalla and E. Bustos, *Photoabsorption processes in nitrous oxide and formaldehyde,* Int. J. Quantum Chem. **85**, 345 (2001).

195. F. Jensen, *Polarization consistent basis sets. II. Estimating the Kohn–Sham basis set limit,* J. Chem. Phys. **116**, 7372 (2002).

196. F. Jensen and T. Helgaker, *Polarization consistent basis sets. V. The elements Si–Cl,* J. Chem. Phys. **121**, 3463 (2004).

197. G. Herzberg, *Molecular Spectra and Molecular Structure, Vol II. Infrared and Raman Spectra of Polyatomic Molecules*, D. van Nostrand, New York (1966).

198. J. H. Callomon and F. Creutzberg, *The electronic emission spectrum of ionized nitrous oxide,* N_2O^+*:* $\tilde{A}^2\Sigma^+$–$\tilde{X}^2\Pi$*,* Phil. Trans. Royal Soc. London A **277**, 157 (1974).

199. H. Lefebvre-Brion and R. W. Field, *The Spectra and Dynamics of Diatomic Molecules,* Elsevier, Amsterdam (2004).

200. R. T. Wiedmann, E. R. Grant, R. G. Tonkyn and M. G. White, *High-resolution threshold photoionization of* N_2O*,* J. Chem. Phys. **95**, 746 (1991).